COMPENSATING SEQUENCES FOR ROBUST QUANTUM CONTROL OF TRAPPED-ION QUBITS

A Thesis
Presented to
The Academic Faculty

by

J. True Merrill

In Partial Fulfillment
of the Requirements for the Degree
Doctor of Philosophy in the
School of Chemistry and Biochemistry

Georgia Institute of Technology
August 2013

COMPENSATING SEQUENCES FOR ROBUST QUANTUM CONTROL OF TRAPPED-ION QUBITS

Approved by:

C. David Sherrill, Committee Chair
Schools of Chemistry and Biochemistry, and Computational Science and Engineering
Georgia Institute of Technology

Kenneth R. Brown, Advisor
Schools of Chemistry and Biochemistry, Computational Science and Engineering, and Physics
Georgia Institute of Technology

Joseph W. Perry
School of Chemistry and Biochemistry
Georgia Institute of Technology

Thomas M. Orlando
Schools of Chemistry and Biochemistry, and Physics
Georgia Institute of Technology

Jungsang Kim
Departments of Electrical and Computer Engineering, Physics, and Computer Science
Duke University

Michael S. Chapman
School of Physics
Georgia Institute of Technology

Date Approved: 14 May 2013

For my grandparents ...

Howard, Jean, Maggie, and Jim

ACKNOWLEDGEMENTS

I would like to recognize those who have made this work possible. In particular, I thank my advisor, Ken Brown, who has been an excellent mentor during my graduate career. Ken has shown me the importance of loving all kinds of science, and also the importance of picking a good problem to work on. I owe my proficiency in quantum mechanics to the many hours we spent together excitedly deriving new results or trying new ideas.

I am deeply grateful for the many people who have helped me through my scientific training, especially my many teachers without whom I would have likely never began graduate studies. Thank you Lesli Bordas for making me a chemist.

Thank you to all of those who have provided mentorship in other areas. Thank you to C.S. Pai and Harley Hayden for teaching me microfabrication.I owe a tremendous debt to Charlie Doret, who still continues to teach me everything I know about experimental matters. Thank you Jason Amini, for showing me how to be wholeheartedly passionate about ion trapping. I am grateful to Alexa Harter and Curtis Volin for giving me the opportunity to work in the most exciting science I have ever been a part of.

I have been fortunate to work with many talented labmates over the years; I would like to acknowledge the help of Craig Clark, James Goeders, Grahame Vittorini, Yu Tomita, Chingiz Kabytayev, Mauricio Gutiérrez, and especially J.P. Addison.

Graduate school is a road paved with many distractions. Thank you to those who distracted me, and made these years so enjoyable. I thank my parents and my wife Natalie for their support during this process.

TABLE OF CONTENTS

LIST OF FIGURES

LIST OF SYMBOLS OR ABBREVIATIONS

$\langle A, B\rangle$	Hilbert-Schmidt inner product, $\langle A, B\rangle = \mathrm{tr}(A^\dagger B)$.
$\mathbf{a}$	Vector on a Lie algebra, $\mathbf{a} = a^\mu \mathbf{e}_\mu$.
$\|\|A\|\|_{HS}$	Hilbert-Schmidt norm, $\|\|A\|\|_{HS} = \sqrt{\langle A, A\rangle}$.
$\delta u^\mu(t)$	First-order deformation of the controls, $\delta u^\mu(t) = \frac{d}{d\epsilon} F^\mu[\vec{u}(t); \epsilon]\big\|_{\epsilon=0}$.
ϵ	Error parameter representing the strength of a systematic error.
$\mathbf{e}_\mu$	Basis vector for a Lie algebra, $\mathbf{e}_\mu = -\mathrm{i}H_\mu$.
$\mathcal{F}$	Quantum gate fidelity.
F^μ	Systematic error model which maps error-free controls to imperfect controls.
$\mathfrak{g}$	Lie algebra.
G	Lie group.
η_{ij}	Lamb-Dicke parameter.
H_μ	Dimensionless Hermitian control Hamiltonian.
Ω	Rabi frequency.
$R(\theta, \phi)$	Single-qubit rotation operator, $R(\theta, \phi) = \exp\left(-\frac{\mathrm{i}\theta}{2}(X\cos\phi + Y\sin\phi)\right)$.
$\mathfrak{su}(N)$	Lie algebra of the special-unitary group $SU(N)$.
$SU(N)$	Special-unitary group of degree N.
$\mathscr{U}$	Admissible set of control solutions.
$\vec{u}(t)$	Vector of control functions, $\vec{u}(t) = (u^1(t), u^2(t), \ldots, u^n(t))$.
$U(\vec{u}; t_f)$	Propagator solution to a Schrödinger equation for the controls $\vec{u}(t)$ over the interval $t \in [0, t_f)$.
$u^\mu(t)H_\mu$	Einstein summation notation for the Hamiltonian, $H(t) = \sum_\mu u^\mu(t)H_\mu$.
$u^\mu(t)$	Real-valued control function with units of angular frequency.
X	Pauli X-operator, $X = \|0\rangle\langle 1\| + \|1\rangle\langle 0\|$.
Y	Pauli Y-operator, $Y = -\mathrm{i}\|0\rangle\langle 1\| + \mathrm{i}\|1\rangle\langle 0\|$.
Z	Pauli Z-operator, $Z = \|0\rangle\langle 0\| - \|1\rangle\langle 1\|$.

SUMMARY

Universal quantum computation requires precision control of the dynamics of qubits. Frequently accurate quantum control is impeded by systematic drifts and other errors. Compensating composite pulse sequences are a resource efficient technique for quantum error reduction. This work describes compensating sequences for ion-trap quantum computers. We introduce a Lie-algebraic framework which unifies all known fully-compensating sequences and admits a novel geometric interpretation where sequences are treated as vector paths on a dynamical Lie algebra. Using these techniques, we construct new narrowband sequences with improved error correction and reduced time costs. We use these sequences to achieve laser addressing of single trapped $^{40}Ca^{+}$ ions, even if neighboring ions experience significant field intensity. We also use broadband sequences to achieve robust control of $^{171}Yb^{+}$ ions even with inhomogeneous microwave fields. Further, we generalize compensating sequences to correct certain multi-qubit interactions. We show that multi-qubit gates may be corrected to arbitrary accuracy if there exists either two non-commuting controls with correlated errors or one error-free control.

A practical ion-trap quantum computer must be extendible to many trapped ions. One solution is to employ microfabricated surface-electrode traps, which are well-suited for scalable designs and integrated systems. We describe two novel surface-electrode traps, one with on-chip microwave waveguides for hyperfine $^{171}Yb^{+}$ qubit manipulations, and a second trap with an integrated high numerical aperture spherical micromirror for enhanced fluorescence collection.

CHAPTER I

INTRODUCTION

Recent years have witnessed tremendous progress in the power, scale, and pervasiveness of computers. Many modern devices now incorporate computing elements, and already computing plays a critical role in many aspects of modern society. Yet despite their widespread availability and usefulness, computers are currently unable to efficiently solve certain kinds of problems, such as breaking an RSA encryption by factoring keys [1], or solving a full configuration-interaction (full CI) problem in quantum chemistry [2]. These problems are difficult from an algorithmic perspective; although a solution can be quickly verified, no efficient methods exist to compute a solution in the first place.

Quantum computing is a rapidly emerging technology that may allow these problems to be solved efficiently. Quantum computers differ from more common (classical) computers in that they exploit quantum phenomena (such as superposition, interference, and entanglement) to process data. These properties enable more efficient algorithms. Quantum computers were first conceived in the 1980's by Richard Feynmann [3], Paul Benioff [4, 5] and others, who mostly focused on using these devices to simulate other quantum systems. The 1990's saw important advances in quantum algorithms [6–8] and theoretical quantum computing [9, 10]. Notably, Peter Shor discovered a factoring algorithm [7] which operates in polynomial time, which greatly improved on the best known classical algorithms. These advances stimulated the development of quantum computing devices [11–16], a line of research which continues to the present day.

Currently multiple quantum computing technologies are under development. Computers constructed from trapped atomic ions are among the most promising. Early work by Wolfgang Paul developed the Paul trap [17, 18]. Hans Dehmelt and others advanced laser cooling and ion imaging techniques [19]. These elements were combined in a proposal by Ignacio Cirac and Peter Zoller [20], who first described how interactions between trapped

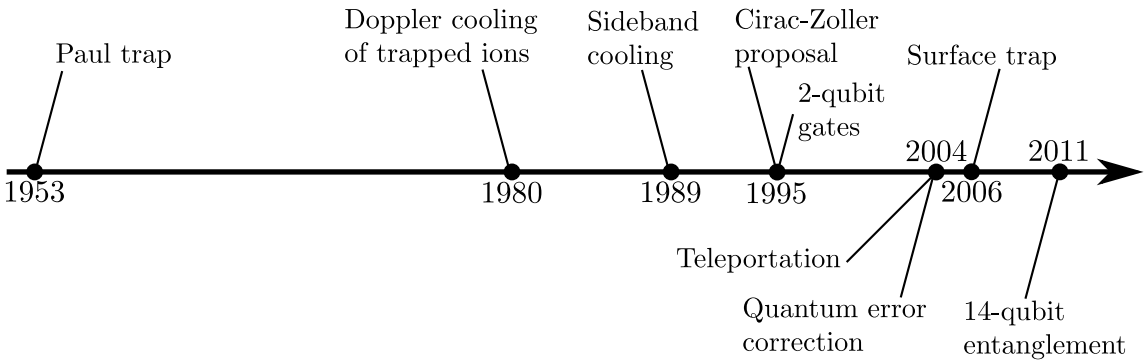

Figure 1.1: Developments towards an ion-trap quantum computer. Wolfgang Paul developed the Paul trap in 1953 [17, 18]. Doppler cooling [19] and sideband cooling [23] techniques were applied to trapped ions in the 1980's. Cirac and Zoller proposed combining these elements in a quantum computer [20]. Soon afterwords the first two-qubit gates were achieved [24, 25]. Recently, quantum teleportation [26], quantum error correction [27], and microfabricated surface-electrode traps [28] have been demonstrated. The current record for the largest entangled state is 14 ions [29].

ions could be used for computation. More recent progress by a number of researchers (notably by Dave Wineland, Rainer Blatt, and others) have demonstrated all of the essential technologies required for universal quantum computation. Current research focuses on improving the quality of quantum logic operations and integrating existing technologies into a computer architecture amenable to scaling to large numbers of trapped ions [21, 22].

One technology well-suited for scaling is the surface-electrode trap [28, 30]. These devices place trapping electrodes in a common plane and are easily miniaturized using microfabrication techniques. Furthermore, complex electrode geometries may be produced, for instance geometries compatible with ion transport [31, 32] and ion reordering [33, 34]. Here at Georgia Tech and the Georgia Tech Research Institute (GTRI) we have built a research program that develops complex surface-electrode traps. A major focus of this thesis is the description and testing of these devices.

1.1 Why errors ruin the party

During logic operations quantum computers utilize a continuum of superposition states. If the system is subjected to a noise process or some kind of systematic error, the computer tends to produce an incorrect superposition. Overcoming errors is a major challenge in

quantum computing, and a serious obstacle towards building practical devices [35]. A common strategy in classical systems is to use measurement and feedback control to stabilize a noisy system. This strategy is difficult in quantum systems since measurement itself irreversibly alters the quantum state.

Quantum error correction (QEC) is a method of protecting quantum information from noise and decoherence by identifying errors and employing active correction measures [38, 39]. These methods are expected to be an essential tool in future quantum processors, since they can correct arbitrary errors provided that they occur with a sufficiently low probability [40] (called the error threshold). QEC employs a kind of quantum redundancy, in the sense that a single logical bit of information is encoded in the entangled state of multiple physical bits [35]. These methods are costly in the sense that they lower the density of stored information, slow the effective speed of the computation, and require highly-entangled systems which are difficult to achieve in practice.

However, many types of systematic errors can be corrected using a simple technique that avoids the costly overhead associated with QEC. Compensating composite pulse sequences reduce systematic errors by choosing operations such that the net error nearly cancels. These methods require no measurements or additional ancilla bits, and improve accuracy even when the strength of the error is unknown. Compensating sequences were originally developed in the context of NMR spectroscopy. Pioneering work in the subject was done by Malcolm Levitt [41, 42], Ray Freeman [43], Robert Tycko [44, 45], and others. These techniques were first introduced to the quantum information community when they were used in NMR quantum computers [46]. Currently several researchers are studying compensating sequences in the context of specific quantum computing models.

1.2 Organization of the thesis

This thesis develops compensating sequences for ion-trap quantum computers. We introduce a control-theoretic formalism that successfully generalizes all known fully-compensating composite sequences. Using this framework, novel sequences which correct systematic errors in ion-trap quantum computers are designed. We demonstrate these methods in several

experiments on trapped atomic ions, and describe how they may be extended to improve pairwise entangling operations.

The thesis is organized as follows. Chapter 2 introduces quantum computing and quantum control theory. Chapter 3 describes ion-trap quantum computers, surface-electrode traps, and related experimental hardware. Chapter 4 introduces compensating pulse sequences, and derives a fundamental set of conditions which all fully-compensating sequences satisfy. Systematic error models for ion-trap quantum computers are also described here. Chapter 5 discusses novel narrowband sequences which correct systematic errors associated with single-ion addressing. We test these sequences in an experiment on single $^{40}Ca^{+}$ ions confined in a surface-electrode trap. Chapter 6 describes a surface-electrode trap with on-chip waveguides which produce near-field microwaves to manipulate single $^{171}Yb^{+}$ ions. We demonstrate compensating sequences which correct errors associated with the microwave field. Chapter 7 extends the composite pulse technique to include multi-ion interactions. Finally, chapter 8 describes a surface electrode trap with an integrated micromirror for efficient fluorescence measurement of trapped ions.

CHAPTER II

QUANTUM COMPUTATION AND CONTROL

The following chapter will summarize fundamental concepts in quantum computation, introduce the notion of quantum information and qubits, and describe quantum control and related techniques.

2.1 Fundamentals of quantum information

2.1.1 Qubits and gates

Modern digital computers store information in *bits* which exists in one of two states, either 0 or 1, usually corresponding to the voltage or magnetization of an electronic switch or storage device. The state of a bit is well described as a classical variable related to bulk properties of many atoms in a device. Unlike classical computers, quantum computers store binary information in a *qubit*, a quantum two-level system with states $|0\rangle$ and $|1\rangle$ corresponding to two distinguishable eigenstates of an observable, for example distinguishable electronic states of a single atom [35].

Unlike a classical bit, a qubit can exist in a superposition of states. The span of the qubit states forms a two-dimensional logical Hilbert space, here denoted as $\mathscr{H}(2)$. A qubit may exit an any normalized state in $\mathscr{H}(2)$, specifically any state of the form

$$|\psi\rangle = \cos\frac{\theta}{2}|0\rangle + \sin\frac{\theta}{2}\mathrm{e}^{\mathrm{i}\phi}|1\rangle, \tag{2.1}$$

where θ and ϕ are real angles. By convention we always neglect an arbitrary unobservable global phase, that is, we consider $\mathrm{e}^{\mathrm{i}\gamma}|\psi\rangle$ and $|\psi\rangle$ to be equivalent since for any observable both states give identical expectation values and probability distributions.

A classical computer retrieves data from memory by measuring the states of bits. Similarly, data is retrieved from a qubit by a measurement on the logical basis. However unlike a classical measurement, a quantum measurement irreversibly alters the qubit state [47].

We consider here ideal hard or projective measurements of the qubit, which in the Copenhagen interpretation collapse the wavefunction (2.1) into the eigenstate $|0\rangle$ with probability $P(0) = \cos^2(\theta/2)$ and into $|1\rangle$ with probability $P(1) = 1 - \cos^2(\theta/2)$. This of course is a special case of more general measurement models [48, 49] which induce a partial collapse caused by the joint interaction of a qubit and a measurement apparatus.

Quantum computers require several qubits grouped into a register to perform useful computational tasks. A register of n qubits exists in a joint quantum state on the Hilbert space $\mathscr{H}(2^n) = \bigotimes_{j=1}^{n} \mathscr{H}_j(2)$ where j is an index over the individual qubits of the register. Data storage on a quantum register is fundamentally different than in the classical counterpart. Consider the task of representing the state of a quantum register on a classical register of bits. To describe an n-qubit wavefunction requires $2^n - 1$ complex numbers, an extremely costly task on a classical system. A common error is to conclude that quantum computers somehow store data more efficiently than their classical counterparts; of course this is false since measurement involves projection of the wavefunction against the computational basis, yielding a binary string of length N. It is more accurate to say that quantum computers exploit quantum phenomena (i.e., superposition, interference and entanglement) to achieve an *algorithmic* speedup over classical computers. A discussion of quantum algorithms is beyond the scope of this work, we refer the reader to [35, 50] for a specific treatment of this topic.

Computation involves the application of logical gates according to some algorithm to yield data. Let U represent a quantum logic gate. The application of U to an arbitrary initial qubit state $|\psi\rangle$ yields the resultant state $|\psi'\rangle = U|\psi\rangle$. However, probability conservation requires $\langle\psi'|\psi'\rangle = \langle\psi|U^\dagger U|\psi\rangle = 1$, which implies that all quantum logic gates are unitary operators. As an example consider the quantum-mechanical analogue of the NOT gate which inverts the state of a bit. In the language of quantum mechanics, this mapping is applied by the Pauli-X operator $X = |0\rangle\langle 1| + |1\rangle\langle 0|$, which is both unitary and Hermitian.

In practice, running a quantum computation reduces to the task of applying a sequence of unitary transformations to a qubit register. Since quantum gates are unitary operators, they are always reversible in principle. Equivalently, during a quantum gate every unique

qubit register state is mapped to a unique final state. This contrasts with several classical gates, such as NAND, which map multiple inputs to the same output [35].

2.1.2 The Bloch sphere

Frequently it is useful to relate an abstract system to a geometric picture leads to an intuitive approach for problem solving. Here we introduce the Bloch sphere [51], which interprets a qubit wavefunction as a pseudo spin-1/2 system and single-qubit gates as rotations. The spin polarization is described by a vector operator $\vec{S} = \hbar\vec{\sigma}/2$ where the components of $\vec{\sigma} = (X, Y, Z)$ are the Pauli operators,

$$X = |0\rangle\langle 1| + |1\rangle\langle 0|, \qquad Y = -\mathrm{i}|0\rangle\langle 1| + \mathrm{i}|1\rangle\langle 0|, \qquad Z = |0\rangle\langle 0| - |1\rangle\langle 1|. \tag{2.2}$$

The Pauli operators are each self-inverse (i.e., an involution), traceless, and transform under commutation as $[X, Y] = 2\mathrm{i}Z$. The Pauli operators and the identity operator span the space of observables, in the sense that the expectation value of any observable may be written as a function of the expectation values of Pauli operators. However the Pauli operators themselves are incompatible observables: we may not precisely determine the components of $\vec{\sigma}$ using a single preparation of the qubit.

We may rewrite (2.1) as a density matrix $\rho = |\psi\rangle\langle\psi| = (1 + \vec{a} \cdot \vec{\sigma})/2$ where 1 is the identity operator, $\vec{a} = (\sin\theta\cos\phi, \sin\theta\sin\phi, \cos\theta)$ is the Bloch vector. The components of $\vec{a}$ correspond to the expectation values of the Pauli operators, for example $\langle X\rangle = \vec{a}_x$. Since by probability conservation $||\vec{a}|| \leq 1$ with equality if an only if ρ is pure, the vectors $\vec{a}$ are confined to a closed ball called the Bloch sphere, shown in figure 2.1. The computational basis states $|0\rangle$ and $|1\rangle$ are antipodal since they correspond to the positive and negative eigenstates of Z.

It is simple to show that single qubit gates are equivalent to spin-rotations on the Bloch sphere. Consider the application of a gate U on the state ρ to form the resultant state $\rho' = (1 + \vec{a} \cdot U\vec{\sigma}U^\dagger)/2$. The transformed vector components $U\vec{\sigma}_j U^\dagger$ themselves act as Pauli operators since they satisfy the same properties: each component is self-inverse, traceless, and all three satisfy an angular momentum commutation relation. The transformation U

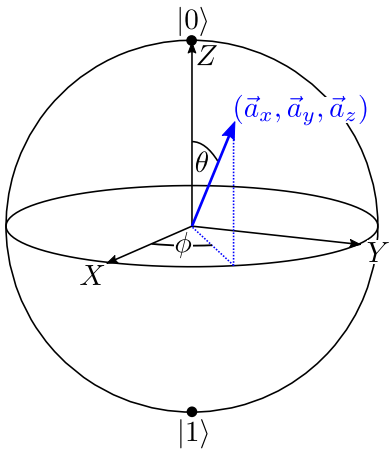

Figure 2.1: A qubit visualized as a vector on a Bloch sphere. The components $(\vec{a}_x, \vec{a}_y, \vec{a}_z)$ uniquely determine the qubit state but are incompatible observables.

only has shifted to a new basis of Pauli operators. Since the vector length $||\vec{a}||$ is preserved, U acts as a rotation.

2.1.3 The DiVincenzo criteria

What are the experimental requirements for building a quantum computer? So far, we have discussed qubits and quantum gates in abstract terms, without regard to a physical system. In this section, we discuss the DiVincenzo criteria [52, 53], which codify a set of hardware requirements for universal quantum computation. In chapter 3 we describe the trapped-ion quantum computing architecture, and explicitly show how this system meets these requirements. Simply stated, the criteria are:

1. *State initialization:* It must be possible to initialize the quantum system into a well defined quantum state. This requirement is easily satisfied if it is possible to *cool* a set of relevant quantum degrees of freedom to the ground state.

2. *Isolation:* The quantum computer must be well isolated from environmental perturbations. Interactions between a (controlled) quantum computer and an (uncontrolled) environment result in a joint entanglement between the systems. To remain isolated, computation must occur sufficiently quickly to avoid significant entanglement, or alternatively, active correction measures must be implemented.

3. *Unitary control:* It must be possible to efficiently approximate any unitary transform $U \in SU(N)$, where $SU(N)$ is the special-unitary group of transformations on the logical Hilbert space $\mathscr{H}(N)$.

4. *Measurement:* It must be possible to subject the system to a projective measurement with distinguishable outcomes. The span of measurement eigenstates should span the logical Hilbert space $\mathscr{H}(N)$.

5. *Scalable architecture:* The quantum computer must be scalable in the sense that an exponential increase in the logical Hilbert space dimension is achieved with a polynomial increase in cost (e.g., hardware, execution time). Typically this is achieved by adding additional particles to a composite quantum system.

In practice, it is challenging to meet each of these requirements simultaneously. In particular, unitary control typically requires a strong-coupling interaction between qubits. However, this frequently complicates qubit isolation, since qubits which interact strongly with each other usually interact strongly with an uncontrolled environment [49]. Ion-trap quantum computers circumvent this difficulty by using long-lived internal states for long-term information storage, shifting to strongly-interacting motional states during qubit-qubit interactions [54, 55].

2.2 Fundamentals of quantum control

Quantum computation requires accurate control of the internal states of a register of qubits. In practice, the task reduces to applying a desired unitary evolution using a finite set of controls, which may be constrained by the physical limitations of the experimental apparatus [56]. Here we review several fundamental concepts in quantum control and introduce mathematical techniques that will be used throughout the thesis. Section 2.2.1 introduces quantum control systems and the notion of *controllability*. Sec. 2.2.2 reviews Lie groups and algebras. Sec. 2.2.3 introduces the Baker-Campbell-Hausdorff formula and the related Magnus expansion. Sec. 2.2.4 introduces several Lie-theoretic decompositions and approximations.

2.2.1 Quantum control systems

We briefly review several fundamental properties of control systems, and discuss the modeling of dynamic quantum systems using control-theoretic techniques. Whenever possible, we adopt notational conventions consistent with both quantum and control theory; however in the case of disagreement we revert to quantum conventions.

Definition 1. *A* control system *modulates or changes the dynamic response of a state* $\vec{x}(t)$ *according to a control law, which is modeled as a system of ordinary differential equations of the form* $\frac{d}{dt}\vec{x} = f(\vec{x}, t, \vec{u})$ *with the components of the control vector* $\vec{u}(t) = (u^1(t), u^2(t), \cdots, u^n(t))$ *chosen to belong to a set of permissible control functions* $\mathscr{U}$.

In classical control, the state $\vec{x}(t)$ is a vector function which completely specifies the system [57]. In quantum control systems, the state is usually synonymous with the wavefunction [56, 58, 59]. However in quantum computing, the object is not to prepare a specific state but efficiently simulate a unitary gate. The quantum state of the qubit register is inaccessible until the end of computation, and therefore any control scheme should be agnostic to the qubit state. This subtle distinction leads to an alternate formulation of the control law [56, 60] where the control state is a unitary propagator $U(t)$, which must satisfy an operational Schrödinger equation,

$$\dot{U}(t) = -\frac{\mathrm{i}}{\hbar} H(t) U(t), \qquad U(0) = 1. \tag{2.3}$$

Of special interest are Hamiltonians that admit a decomposition of the form $H(t) = \hbar \sum_\mu u^\mu(t) H_\mu$, where the control Hamiltonians $H_\mu \in \{H_1, H_2, \ldots, H_n\}$ are dimensionless Hermitian operators modulated by real-valued control functions $u^\mu(t)$ representing the n available degrees of control for a particular experimental apparatus. We interpret the vector $\vec{u}(t) = (u^1(t), u^2(t), \ldots, u^n(t))$ as a vector function over the manifold of control parameters, with components $u^\mu(t)$ representing the magnitudes of the control Hamiltonians with units of angular frequency. For compactness we employ an Einstein summation convention over repeated Greek indices where the sum over controls is simply written as $u^\mu(t) H_\mu$. This notation is motivated by the transformation properties of the Hamiltonian when interpreted as a member of a dynamic Lie algebra.

We omit a term which represents the portion of the total Hamiltonian which is outside of direct control (i.e. a drift Hamiltonian); in principle it is always possible to work in an interaction picture where this term is removed. Alternatively, one may assign a Hamiltonian H_0 to represent this interaction, with the condition that $u^0(t) = 1$ for all t.

In practice, a desired evolution is prepared by carefully manipulating the coupling of the system to a control apparatus, such as a spectrometer. The controls may be subject to a set of constraints imposed by the physics of the system; we say the control must belong to an admissible set $u^\mu(t) \in \mathscr{U}$ [56, 58]. Constraints may include limitations on the total operation length, control amplitudes or derivatives, or possibly Fourier components. The constraints indirectly limit the admitted propagator solutions of the Schrödinger equation. Denote by $U(\vec{u}; t_f)$[1] the particular solution of (2.3) for the controls $\vec{u}(t)$ over the interval $t \in [0, t_f)$. The set of reachable solutions may be described as follows.

Definition 2. *The* reachable set *at time $t_f > 0$, denoted as $\mathscr{R}(t_f)$, is the set of all propagators $U(\vec{u}; t_f) \in \mathscr{R}(t_f)$ produced by admissible controls $u^\mu(t) \in \mathscr{U}$ over the interval $t \in [0, t_f)$. The reachable set $\mathscr{R}(\leq t_f)$ is the union of all reachable sets for times less than or equal to t_f, e.g., $\mathscr{R}(\leq t_f) = \cup_{0 \leq \tau \leq t_f} \mathscr{R}(\tau)$. The reachable set $\mathscr{R} = \cup_{\tau \geq 0} \mathscr{R}(\tau)$ is the union of all sets over all positive time intervals.*

The reachable set determines the controllability of the system. For instance if $\mathscr{R} = SU(N)$ then by an appropriate choice of controls every unitary gate in $SU(N)$ may be produced. Such a system is called *controllable* [56, 61]. An equivalent concept exists in quantum information literature; if every unitary gate may be produced by a quantum computer, then the computer is *universal* [35, 62]. Therefore it is important to confirm whether a quantum computer is actually controllable, and also to determine control schemes that perform gates in some optimal way.

Constraints on the controls frequently introduce boundaries on the reachable set $\mathscr{R}(\leq t_f)$. For instance, consider the control system (2.3) where the control Hamiltonians are related to the Pauli operators by $H_\mu \in \{X/2, Y/2, Z/2\}$ and the magnitude of the control

[1] Another common notation uses the Dyson time-ordering operator T to write $U(\vec{u}; t_f)$ as a time-ordered exponential of the form $U(\vec{u}; t_f) = T \exp\left(-\frac{i}{\hbar} \int_0^{t_f} dt' \, H(t')\right)$.

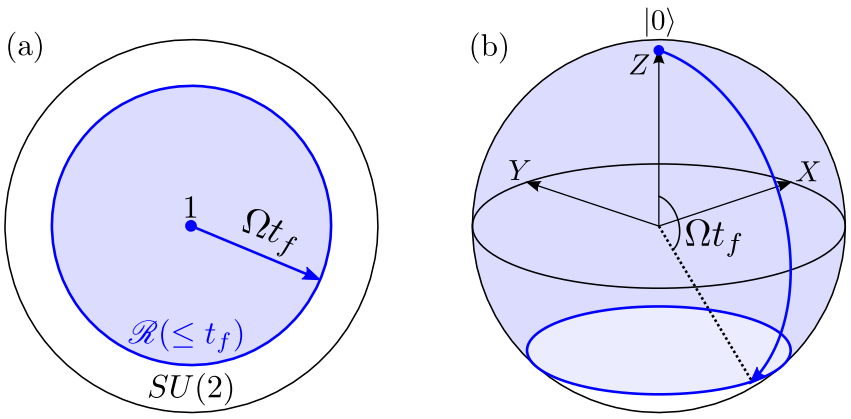

Figure 2.2: The reachable set $\mathscr{R}(\leq t_f)$ for a bounded control problem on the group of single-qubit gates $SU(2)$. (a) $\mathscr{R}(\leq t_f)$ viewed as a subset of $SU(2)$, where the distance from the identity element 1 corresponds to the angle of rotation provided by a propagator $U \in \mathscr{R}(\leq t_f)$. (b) The reachable set viewed as accessible states on a Bloch sphere, starting from the initial qubit state $|0\rangle$.

vector is bounded to not exceed some maximum frequency $||\vec{u}(t)|| \leq \Omega$. This control problem is equivalent to the problem of producing single qubit rotations with a time-dependent field (laser, microwave, etc.) of bounded amplitude. At time $t_f < \pi/\Omega$ the largest accessible qubit rotations are by an angle Ωt_f, therefore rotations exceeding this maximal angle are inaccessible. The minimum time which produces any single-qubit rotation up to a global phase is $t_\pi = \pi/\Omega$, frequently called the π-time in quantum computing experiments. Figure 2.2 illustrates the reachable set in this control problem.

2.2.2 Lie groups and algebras

So far our discussion on quantum control has repeatedly referred to a Lie group, which may be thought of as a continuous group of transformations. Here we briefly discuss several aspects of the theory of Lie groups, with emphasis on conceptual clarity over mathematical rigor. The interested reader is referred to Refs. [56] and [63] for additional details and a rigorous treatment of the subject.

Definition 3. *A* Lie group G *is a continuous group which is also a differentiable manifold with analytic group multiplication and group inverse operations.*

Consider the reachable set $\mathscr{R}$ for unbounded controls $u^\mu(t)$. Observe that this set forms

a representation of a Lie group since the following properties are satisfied: for all solutions U_1 and U_2, the product U_1U_2 is also a solution (see section 2.2.3); the associative property is preserved (i.e. $U_1(U_2U_3) = (U_1U_2)U_3$); the identity 1 is a valid solution; and for all solutions U_1, the inverse $U_1^\dagger$ is also a valid solution. Moreover, by nature of (2.3) differentiation of propagators is well defined and the set forms a continuous differentiable manifold, parameterized by the control functions. The set of N-dimensional quantum propagators forms a representation of the unitary group $U(N)$, which is a Lie group [63]. Without loss of generality, we may restrict our attention to the special unitary subgroup $SU(N)$, since every element in $U(N)$ is equivalent to an element in $SU(N)$ with an additional global phase [63, 64].

Lie groups are also manifolds and therefore have topological properties. For instance, $SU(N)$ is connected and compact, meaning any two points (unitary operators) on the manifold may be connected by a curve on the manifold, and any curve may be subdivided into subcurves that converge to a point as the divisions become infinitesimally small [63]. In particular $SU(2)$ is homomorphic to rotations of the 2-sphere. Any pair of operators $U_1, U_2 \in SU(2)$ are connected by a curve that converges to a single point as U_2 approaches U_1. The curves themselves are related to the controls by (2.3); in the case of controls that are constant in time, the produced curve is a geodesic on the manifold. Thus we can build a picture where group elements are transformed into other elements along a continuous path determined by the application of a set of controls.

Definition 4. *A* Lie algebra $\mathfrak{g}$ *is a vector space over an associated field* $\mathscr{F}$ *which is closed under the Lie bracket, e.g.,* $[\mathbf{a}, \mathbf{b}] \in \mathfrak{g}$ *for all* $\mathbf{a}, \mathbf{b} \in \mathfrak{g}$*. Each Lie group* G *has an associated algebra* $\mathfrak{g}$*, whose vector space is the tangent space of* G *at the identity element.*

The Lie algebra for a group G is directly related to the control Hamiltonians $\{H_\mu\}$ [56, 65]. This is easily seen by differentiating the elements $U(\vec{u}; t_f)$ in the neighborhood of the identity element to find a family of tangent curves at $U(\vec{u}; 0) = 1$,

$$\left.\frac{dU(\vec{u};t)}{dt}\right|_{t=0} = -\mathrm{i}u^\mu(0)H_\mu = u^\mu(0)\mathbf{e}_\mu. \tag{2.4}$$

The set of skew-symmetrized Hamiltonians $\{\mathbf{e}_\mu = -\mathrm{i}H_\mu\}$ and the field of real numbers $\mathbb{R}$ (corresponding to the allowed values for the components $u^\mu(0)$) form a linear vector space under matrix addition and the scalar product. We therefore interpret terms $\mathbf{u} = u^\mu \mathbf{e}_\mu$ as vectors on the tangent space of G at the identity, denoted by $T_1 G$. On this space is defined the binary Lie bracket operation between two vectors $[\mathbf{a}, \mathbf{b}]$, which for our purposes is synonymous with the operator commutator. If the space $T_1 G$ remains closed under the Lie bracket, then it forms a Lie algebra $\mathfrak{g}$ corresponding to the group G.

We note however that the available control Hamiltonians do not necessarily need to be closed under commutation in order to generate an algebra. Suppose $\mathfrak{e} = \mathrm{span}\{\mathbf{e}_\mu\}$[2] and $\mathfrak{m} = \mathfrak{e}^\perp$ are subspaces of an algebra $\mathfrak{g} = \mathfrak{e} \oplus \mathfrak{m}$. If $\mathfrak{e}$ is not an algebra, commutators of the form $[\mathfrak{e}, \mathfrak{e}]$ return elements in both $\mathfrak{e}$ and $\mathfrak{m}$. Once these commutators are calculated, elements outside of $\mathfrak{e}$ may be appended to a new larger subspace $\mathfrak{e}'$ with a smaller orthogonal compliment $\mathfrak{m}'$. This procedure can be iterated until $\mathfrak{e}'$ is closed under the commutator, or if $\mathfrak{e}'$ never converges, we may construct $\mathfrak{e}'$ as an infinite vector space of the nested commutators produced by this procedure. Then $\mathfrak{e}' \subseteq \mathfrak{g}$ and $\mathfrak{e}'$ is a Lie algebra. Physically this means that we need not have direct control over all Hamiltonians that span a Lie algebra in order to produce any gate within its associated group. In section 2.2.4.1 we provide explicit constructions that produce any propagator in a Lie group using a finite set of control Hamiltonians that generate the algebra by repeated Lie brackets.

The power of most Lie algebraic techniques relies on the mapping between group elements which act on a manifold (such as the manifold of rotations on a Bloch sphere) to elements in a Lie algebra which are members of a vector space. In the groups we study here, the mapping is provided by the exponential function $G = \mathrm{e}^{\mathfrak{g}}$ (i.e., every element $U \in G$ may be written as $U = \mathrm{e}^{t\mathbf{u}}$ where $t\mathbf{u} \in \mathfrak{g}$, see figure 2.3). The object of this method is to study the properties of propagators, which are members of a Lie group, in terms of vector operations on the associated Lie algebra.

[2]The operation span denotes all linear combinations with coefficients in the field $\mathscr{F}$, here the field of real numbers.

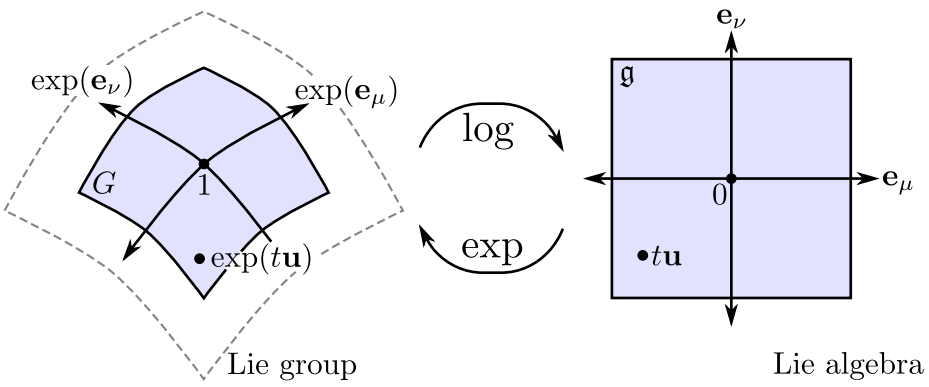

Figure 2.3: Elements on a Lie algebra are transformed to members of a Lie group by the exponential mapping. Frequently, calculations are easier to perform on a Lie algebra (a linear vector space) than the associated group (a manifold).

2.2.2.1 Inner products, norms, and basis transformations

Frequently it is useful to associate an inner product with an algebra in order to form an inner product space [63]. We shall use the Hilbert-Schmidt inner product (also known as the Frobenius product), which is a natural extension of the vector inner product over the field of complex numbers to matrices with complex coefficients. Let A and B be $n \times n$ matrices with entries A_{ij} and B_{ij} respectively. The Hilbert-Schmidt inner product $\langle A, B \rangle$ is defined as,

$$\langle A, B \rangle = \sum_{i=1}^{n} \sum_{j=1}^{n} A_{ji}^* B_{ij} = \mathrm{tr}(A^\dagger B). \tag{2.5}$$

This inner product has several properties that closely mirror the inner product for complex vectors, namely $\langle A, B \rangle = \langle B, A \rangle^*$, and $|\langle A, V \rangle| \leq ||A||_{HS} ||B||_{HS}$, where the Hilbert-Schmidt norm $||A||_{HS} = \sqrt{\langle A, A \rangle}$ also satisfies a corresponding triangle inequality $||A + B||_{HS} \leq ||A||_{HS} + ||B||_{HS}$. Also, using the inner product we easily construct a metric tensor $g_{\mu\nu} = \langle \mathbf{e}_\mu, \mathbf{e}_\nu \rangle$ to measure intervals on the Lie algebra.

We also consider basis transformations on a Lie algebra. For instance a set of control Hamiltonians may form an overcomplete basis; we can switch to a more useful basis, for instance an orthogonal basis under the Hilbert-Schmidt inner product, by applying a linear basis transformation. Let $\{\mathbf{e}_\mu\}$ be a basis that spans an algebra $\mathfrak{g}$ and let $\{\mathbf{e}'_\mu\}$ be a new basis related by an pseudoinvertable transformation $\mathbf{e}'_\nu = A^\mu_\nu \mathbf{e}_\mu$. Any vector $\mathbf{u} = u^\mu \mathbf{e}_\mu =$

$(u^\mu)'\mathbf{e}'_\mu$ must be invariant under the change of basis, requiring that the coordinates transform contravariantly as $(u^\mu)' = u^\nu (A^{-1})^\mu_\nu$, where A^{-1} is the pseudoinverse basis transformation. For this reason, we use a notation that writes the controls $u^\mu(t)$ as contravariant vector components.

2.2.2.2 The spinor rotation group $SU(2)$

As a relevant example, we return to the group of single-qubit operations $SU(2)$ which is generated by the spin operators $H_\mu \in \{X/2, Y/2, Z/2\}$. The skew-symmetrized control Hamiltonians are closed under the Lie bracket and thus form a representation of the Lie algebra $\mathfrak{su}(2) = \text{span}\{-\text{i}X/2, -\text{i}Y/2, -\text{i}Z/2\}$. Therefore, any element in $U \in SU(2)$ may be written as $U = \exp(-\text{i}tu^\mu H_\mu)$, where $-\text{i}tu^\mu H_\mu \in \mathfrak{su}(2)$ may now be interpreted as a vector on the the Lie algebra. Furthermore, since $\langle -\text{i}H_\mu, -\text{i}H_\nu \rangle = \delta_{\mu\nu}/2$, the spin operators form an orthogonal basis for the algebra.

2.2.3 Exponential formulas

2.2.3.1 The Baker-Campbell-Hausdorff formula

Elements of a Lie algebra are related to members of a Lie group by an exponential mapping. In the following, it will be useful to relate the product of two members of a Lie group to a vector on the Lie algebra. The relationship allows us to map products of propagators to an effective Hamiltonian that generates the net operation. This correspondence is provided by the Baker-Campbell-Hausdorff (BCH) formula [63, 66], which relates group products to a series expansion in the Lie algebra. For rapid convergence, it is most convenient to consider products of infinitesimal unitary operations, that is, operations of the form $\text{e}^{\epsilon t\mathbf{u}}$, where $t\mathbf{u} \in \mathfrak{g}$ and $\epsilon < 1$ is a real expansion parameter. We assume ϵ is sufficiently small to guarantee that the group product of propagators always lies within the radius of convergence for the expansion [67]. Let $U_1 = \text{e}^{\epsilon t_1 \mathbf{u}_1}$ and $U_2 = \text{e}^{\epsilon t_2 \mathbf{u}_2}$ be members of a Lie group G, where the Hamiltonians $\mathbf{u}_\mu = -\text{i}H_\mu \in \mathfrak{g}$ are members of the associated algebra. The BCH representation for the product $U_1 U_2 = U_3$ involves the calculation of an effective

Hamiltonian $\mathbf{F} \in \mathfrak{g}$ by the expansion

$$U_3 = \exp(\mathbf{F}) = \exp\left(\sum_n^\infty \epsilon^n \mathbf{F}_n\right), \tag{2.6}$$

where the terms

$$\begin{aligned}
\epsilon\mathbf{F}_1 &= \epsilon(t_1\mathbf{u}_1 + t_2\mathbf{u}_2) \\
\epsilon^2\mathbf{F}_2 &= \frac{\epsilon^2}{2}[t_1\mathbf{u}_1, t_2\mathbf{u}_2] \\
\epsilon^3\mathbf{F}_3 &= \frac{\epsilon^3}{12}\Big([t_1\mathbf{u}_1, [t_1\mathbf{u}_1, t_2\mathbf{u}_2]] + [t_2\mathbf{u}_2, [t_2\mathbf{u}_2, t_1\mathbf{u}_1]]\Big),
\end{aligned}$$

are calculated from $t_1\mathbf{u}_1$, $t_2\mathbf{u}_2$, and nested commutators of elements of the Lie algebra. A combinatoric formula found by Dykin [68] exists to calculate $\mathbf{F}_n$ for arbitrary n. The expansion may be truncated once a desired level of accuracy is reached. In principle, group products of arbitrarily length may be approximated to arbitrary accuracy using BCH formulas; however, these formulas rapidly become unwieldy and difficult to use without the aid of a computer. The BCH expansion is most useful for systems where the controls are piecewise constant, meaning that over each constant interval the Hamiltonian is time independent.

2.2.3.2 The Magnus expansion

A related expansion developed by Magnus [69] may be used to compute the propagator generated by a general time-dependent Hamiltonian. The solution to a control equation (e.g. $\dot{U}(t) = \epsilon\mathbf{u}(t)U(t)$, where $\epsilon\mathbf{u}(t) = -\mathrm{i}\epsilon u^\mu(t)H_\mu$) over the interval $t \in [0, t_f)$ may be written as the power series

$$U(\vec{u}; t_f) = \exp(\mathbf{\Omega}(\vec{u}; t_f)) = \exp\left(\sum_n^\infty \epsilon^n \mathbf{\Omega}_n(\vec{u}; t_f)\right), \tag{2.7}$$

where the first few expansion terms are,

$$\begin{aligned}
\epsilon\mathbf{\Omega}_1(\vec{u}; t_f) &= \epsilon \int_0^{t_f} dt\, \mathbf{u}(t) \\
\epsilon^2\mathbf{\Omega}_2(\vec{u}; t_f) &= \frac{\epsilon^2}{2}\int_0^{t_f} dt \int_0^t dt'\, [\mathbf{u}(t), \mathbf{u}(t')] \\
\epsilon^3\mathbf{\Omega}_3(\vec{u}; t_f) &= \frac{\epsilon^3}{6}\int_0^{t_f} dt \int_0^t dt' \int_0^{t'} dt''\, ([\mathbf{u}(t), [\mathbf{u}(t'), \mathbf{u}(t'')]] + [\mathbf{u}(t''), [\mathbf{u}(t'), \mathbf{u}(t)]]).
\end{aligned}$$

Again as a matter of notational convenience, we drop the labels $(\vec{u}; t_f)$ on the expansion terms when there is no risk of confusion. Formulas for higher order terms may be found in [70]. The BCH and Magnus expansions are in fact intimately related; when considering piecewise-constant controls the techniques are equivalent. We refer the interested reader to [67] for further details regarding both the Magnus expansion and BCH formulas.

The BCH and Magnus expansions are very well known in composite pulse literature, and techniques that utilize these expansions are collectively referred to as average Hamiltonian theory. A variant of this technique, pioneered by Waugh [71, 72], has been a mainstay of composite pulse design in the NMR community for decades. In some formalisms, the BCH expansion of the product of two propagators is interpreted as a power series in the rotation axis and angle. For the study of composite single-qubit rotations, this picture is extremely useful as it allows rotations on the sphere to guide the mathematics. However, this picture of composite rotations can not be generalized to more complex groups, such as the group of n-qubit operations $SU(2^n)$.

In this work, we emphasize a Lie algebraic interpretation of these methods, which also leads to a second geometric picture for the terms of the expansions. Observe that the first-order terms $\mathbf{F}_1$ and $\mathbf{\Omega}_1$ may be regarded as simple vector sums on the Lie algebra, i.e., the sum of $t_1\mathbf{u}_1$ and $t_2\mathbf{u}_2$ in the BCH expansion, and the sum of each of the infinitesimal vectors $dt\,\mathbf{u}(t)$ in the Magnus expansion (see figure 2.4). In an analogous way, one may interpret the higher order terms as the addition of successively smaller vectors on $\mathfrak{g}$. From this insight, one may construct controls which produce a target unitary from geometric considerations on the Lie algebra.

2.2.4 Decompositions and approximation methods

Several useful techniques involve decompositions that may be understood in terms of the structure of a Lie group and its corresponding algebra. In this section we discuss several important methods and identities.

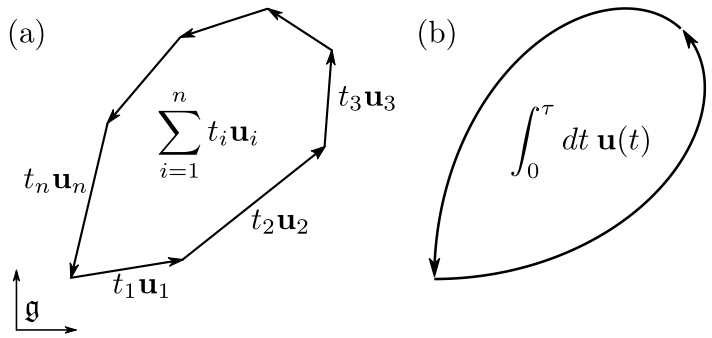

Figure 2.4: Vector paths on a Lie algebra $\mathfrak{g}$ may be used to represent a sequence of propagations. (a) The BCH expansion relates group multiplication of several propagators to vector addition on $\mathfrak{g}$. (b) The Magnus expansion relates continuous controls to an integral series on $\mathfrak{g}$.

2.2.4.1 Basic building operations

Given a limited set of controls $\{\mathbf{u}_1, \mathbf{u}_2\}$ that generate the algebra $\mathfrak{g}$, one may produce any unitary operation in the corresponding Lie group $G = \mathrm{e}^{\mathfrak{g}}$ using only two identities. The first identity, the Lie-Trotter formula [73], describes how to produce a unitary generated by the sum of two non-commuting control operators. Using the BCH formula one may compute that $\mathrm{e}^{t_1\mathbf{u}_1/n}\mathrm{e}^{t_2\mathbf{u}_2/n} = \mathrm{e}^{(t_1\mathbf{u}_1+t_2\mathbf{u}_2)/n} + O([t_1\mathbf{u}_1, t_2\mathbf{u}_2]/n^2)$. In terms of physical pulses, this corresponds to dividing the propagators $\mathrm{e}^{t_1\mathbf{u}_1}$ and $\mathrm{e}^{t_2\mathbf{u}_2}$ into n equal intervals to produce the propagators $\mathrm{e}^{t_1\mathbf{u}_1/n}$ and $\mathrm{e}^{t_2\mathbf{u}_2/n}$. Suppose we perform n such successive products, so that the resulting propagator is

$$\left(\mathrm{e}^{t_1\mathbf{u}_1/n}\mathrm{e}^{t_2\mathbf{u}_2/n}\right)^n = \mathrm{e}^{t_1\mathbf{u}_1+t_2\mathbf{u}_2} + O([t_1\mathbf{u}_1, t_2\mathbf{u}_2]/n). \tag{2.8}$$

Although the Hamiltonians $\mathbf{u}_1 = -\mathrm{i}u_1^\mu H_\mu$ and $\mathbf{u}_2 = -\mathrm{i}u_2^\mu H_\mu$ do not commute in general, we may approximate $U = e^{t_1\mathbf{u}_1+t_2\mathbf{u}_2}$ to arbitrary accuracy by dividing the evolution into n-many time intervals and using the construction (2.8). By extension, it follows that any unitary generated by a Hamiltonian in the Lie algebra subspace $\mathrm{span}\{\mathbf{u}_1, \mathbf{u}_2\}$ may be approximated to arbitrary accuracy using a Trotter sequence. A number of improved sequences were developed by Suzuki [74] that remove errors to higher commutators and scale more strongly with n.

The second identity, which we refer to as the balanced group commutator, enables

the synthesis of a unitary generated by the Lie bracket $[t_1\mathbf{u}_1, t_2\mathbf{u}_2]$. Again the BCH formula may be used to show $\mathrm{e}^{t_1\mathbf{u}_1/n}\mathrm{e}^{t_2\mathbf{u}_2/n}\mathrm{e}^{-t_2\mathbf{u}_1/n}\mathrm{e}^{-t_2\mathbf{u}_2/n} = \mathrm{e}^{[t_1\mathbf{u}_1,t_2\mathbf{u}_2]/n^2} + O([t_1\mathbf{u}_1 + t_2\mathbf{u}_2, [t_1\mathbf{u}_1, t_2\mathbf{u}_2]]/n^3)$. If we now consider n^2-many successive balanced group commutator constructions, the resulting propagator is

$$\left(\mathrm{e}^{t_1\mathbf{u}_1/n}\mathrm{e}^{t_2\mathbf{u}_2/n}\mathrm{e}^{-t_1\mathbf{u}_1/n}\mathrm{e}^{-t_2\mathbf{u}_2/n}\right)^{n^2} = \mathrm{e}^{[t_1\mathbf{u}_1,t_2\mathbf{u}_2]} + O([t_1\mathbf{u}_1 + t_2\mathbf{u}_2, [t_1\mathbf{u}_1, t_2\mathbf{u}_2]]/n). \quad (2.9)$$

Then, as in the case of the Trotter formula, we may approximate $U = \mathrm{e}^{[t_1\mathbf{u}_1,t_2\mathbf{u}_2]}$ to arbitrary accuracy by increasing the number of intervals n. Since by assumption the entire Lie algebra may be generated by nested Lie brackets between the Hamiltonians $\mathbf{u}_1$ and $\mathbf{u}_2$, this implies that any $U \in G$ may be produced by a combination of balanced group commutator and Trotter formulas. However, we emphasize that in almost all cases much more efficient constructions exist. The balanced group commutator construction also forms the basis of the Solovay-Kitaev theorem [75], an important result regarding the universality of a finite gate set in quantum computation.

2.2.4.2 Euler decomposition

In section 2.2.2.2 it was shown that any one-qubit operation $U \in SU(2)$ may be written in the form $U = \exp(-\mathrm{i}tu^\mu H_\mu)$ where $H_\mu \in \{X/2, Y/2, Z/2\}$. It is well known that an alternative representation exists, namely the Euler decomposition

$$U = \exp(-\mathrm{i}\alpha_3 H_x)\exp(-\mathrm{i}\alpha_2 H_y)\exp(-\mathrm{i}\alpha_1 H_x), \quad (2.10)$$

which is given by sequential rotations by the angles $\{\alpha_1, \alpha_2, \alpha_3\}$ about the X, Y, and X axes of the Bloch sphere. The Euler decomposition gives a method of producing rotations generated by a Hamiltonian outside of direct control. For example, suppose the Hamiltonian H_z is outside of direct control so that $U = \exp(-\mathrm{i}\theta H_z)$ cannot be directly produced; however if $\{H_x, H_y\}$ are available, the Euler decomposition $U = \exp(-\mathrm{i}\frac{\pi}{2}H_x)\exp(-\mathrm{i}\theta H_y)\exp(\mathrm{i}\frac{\pi}{2}H_x)$ may be implemented.

2.2.4.3 Cartan decomposition

Let $\mathfrak{g}$ be a semi-simple Lie algebra that may be decomposed into two subspaces $\mathfrak{g} = \mathfrak{k} \oplus \mathfrak{m}$, $\mathfrak{m} = \mathfrak{k}^{\perp}$ satisfying the commutation relations,

$$[\mathfrak{k}, \mathfrak{k}] \subseteq \mathfrak{k}, \qquad [\mathfrak{m}, \mathfrak{k}] \subseteq \mathfrak{m}, \qquad [\mathfrak{m}, \mathfrak{m}] \subseteq \mathfrak{k}. \tag{2.11}$$

Such a decomposition is called a Cartan decomposition of $\mathfrak{g}$ [56]. Suppose for the moment there exists a subalgebra $\mathfrak{a}$ of $\mathfrak{g}$ which is in a subspace of $\mathfrak{m}$. Since $\mathfrak{a}$ is an algebra of its own right, it is closed under the Lie bracket $[\mathfrak{a}, \mathfrak{a}] \subseteq \mathfrak{a}$. However, note $\mathfrak{a} \subseteq \mathfrak{m}$ implies that $[\mathfrak{a}, \mathfrak{a}] \subseteq [\mathfrak{m}, \mathfrak{m}] \subseteq \mathfrak{k}$. Since the subspaces $\mathfrak{k}$ and $\mathfrak{m}$ are mutually orthogonal, then $[\mathfrak{a}, \mathfrak{a}] = \{0\}$ and the subalgebra $\mathfrak{a}$ must be abelian. A maximal abelian subalgebra $\mathfrak{a} \subseteq \mathfrak{m}$ for a Cartan decomposition pair $(\mathfrak{k}, \mathfrak{m})$ is called a Cartan subalgebra [56].

For brevity, we state without proof an important theorem regarding the decomposition of an operator in a group G with a Lie algebra admitting a Cartan decomposition. Consider a Lie algebra $\mathfrak{g}$ with a Cartan subalgebra $\mathfrak{a}$ corresponding to the decomposition pair $(\mathfrak{k}, \mathfrak{m})$. Every U in the group $G = \mathrm{e}^{\mathfrak{g}}$ may be written in the form,

$$U = K_2 A K_1, \tag{2.12}$$

where $K_1, K_2 \in \mathrm{e}^{\mathfrak{k}}$ and $A \in \mathrm{e}^{\mathfrak{a}}$. This is called the KAK Cartan decomposition for the group G. The interested reader is referred to [63] for additional details regarding the KAK decomposition.

As a relevant example, here we show how the Euler decomposition for a propagator $U \in SU(2)$ is a special case of a KAK decomposition. The algebra is spanned by the orthogonal basis matrices $\mathfrak{su}(2) = \mathrm{span}\{-\mathrm{i}H_x, -\mathrm{i}H_y, -\mathrm{i}H_z\}$. Observe that $\mathfrak{k} = \mathrm{span}\{-\mathrm{i}H_x\}$ and $\mathfrak{m} = \mathrm{span}\{-\mathrm{i}H_y, -\mathrm{i}H_z\}$ form a Cartan decomposition for $\mathfrak{su}(2)$. The maximal abelian subalgebra of $\mathfrak{m}$ is one-dimensional; we choose $\mathfrak{a} = \mathrm{span}\{-\mathrm{i}H_y\}$ although the choice $\mathfrak{a}' = \mathrm{span}\{-\mathrm{i}H_z\}$ would serve just as well (i.e. the different axis conventions of the Euler decomposition differ in the choice of a maximal abelian subalgebra). Then by (2.12), every element $U \in SU(2)$ may be expressed in the form $U = \exp(-\mathrm{i}\alpha_3 H_x)\exp(-\mathrm{i}\alpha_2 H_y)\exp(-\mathrm{i}\alpha_1 H_x)$, where the parameters α_j are real. This is a restatement of (2.10), thus completing the proof. The

KAK decomposition is an existence theorem, and does not provide a direct method for the calculation of the required rotation angles α_j.

The Cartan decomposition has important implications for universality. For instance, if one may generate any unitary operation over the subgroups $e^{\mathfrak{k}}$ and $e^{\mathfrak{a}}$, then any gate in the larger group $e^{\mathfrak{g}}$ may be produced. Another important application is the decomposition of large Lie groups into products of more simple ones. Of special interest to quantum computing is the inductive decomposition of n-qubit $SU(2^n)$ gates into products of one-qubit $SU(2)$ and two-qubit $SU(4)$ rotations [76].

2.3 Summary

In this chapter, we have introduced quantum computing and quantum control theory. Quantum computers encode information in binary strings of two-level systems, called qubits. Logic operations on qubits are reversible unitary operators. A universal quantum computer must be able to apply an arbirtary unitary transformation. We treat this problem using control theory. To apply gates, we modulate a set of interactions (control Hamiltonians) according to an instruction set (control functions). We have shown that the reachable set of unitary gates is related to the Lie algebra generated by the control Hamiltonians. Further, we introduced the Baker-Campbell-Hausdorff and Magnus expansions, and also discussed Lie-theoretic decompositions and approximation methods. The following chapter discusses ion-trap quantum computers and describes interactions on trapped ions using a set of control Hamiltonians. Later, we use these techniques to describe compensating pulse sequences.

CHAPTER III

FUNDAMENTALS OF TRAPPED-ION QUANTUM COMPUTING

This chapter provides a brief introduction to trapped-ion quantum computing experiments and interprets the manipulation of atomic ions as a quantum control problem. Trapped-ion computers can be understood in terms of three fundamental components: an *ion trap* which stores a string of ion qubits, a *control field* such as a laser or microwave field which couples the qubit levels during logic operations, and *photodetectors* which discriminate between "bright" and "dark" qubit states during a fluorescence measurement. We shall describe how these components may be used to produce universal quantum computation. Section 3.1 describes the motion of ions in a Paul trap, and required experimental hardware. Section 3.2 describes the internal structure of trapped-ion qubits, the processes of qubit initialization and readout, and the laser systems used to control atomic ions. Section 3.3 describes how laser or microwave pulses may be used to implement a universal set of quantum gates.

3.1 Motional degrees of freedom

Quantum computers based on trapped ions use an *ion trap* to store qubits and to isolate them from environmental perturbations. Most implementations also require quantum control of the motional states of trapped ions for conditional two-qubit gates. In this section our focus will be the motion of charged ions in a Paul trap [17, 18]. Included in this description are electrode geometries other than a traditional quadrupole configuration; all we require is an approximately quadrupolar electric potential at the center of the trapping region. The classical equations of motion for this problem are well studied and are described in detail by Ghosh [77] and numerous other sources. We review the classical solution in section 3.1.1 before turning our attention to a full quantum description of the problem in section 3.1.2. Section 3.1.3 describes surface-electrode traps and the experimental apparatus we use to trap atomic ions.

3.1.1 Classical treatment

Consider the motion of an ion in an electric field described by the quadrupolar scalar potential

$$\Phi = \frac{V_{DC}}{2} \sum_j \alpha_j x_j^2 + \frac{V_{RF}(t)}{2} \sum_j \alpha'_j x_j^2 \tag{3.1}$$

where the index $j \in \{x, y, z\}$ runs over spatial coordinates and the constants α_j, α'_j set the curvature of the potential. The potential is factored into two parts: a static component V_{DC}, and a time-dependent component $V_{RF}(t) = V_{RF} \cos(\Omega_{RF} t)$ that varies sinusoidally at an RF drive frequency Ω_{RF}. Further, we assume the near-absence of time-varying magnetic fields so that the electric field is well approximated by the negative gradient of (3.1). The potential must satisfy Laplace's equation at every instant in time, requiring that $\sum_j \alpha_j = 0$ and $\sum_j \alpha'_j = 0$ are simultaneously satisfied. Since the sign of each α_j determines whether the potential is attractive or repulsive, this implies that an ion experiences a restoring force in at most two directions at once. No potential minimum exists in three-dimensional space, so ions may only be trapped in an "average" dynamical way.

A linear Paul trap produces a scalar potential of the form (3.1) by superimposing fields generated by a set of parallel DC and RF electrodes [77–79]. The Paul trap geometry yields stable trapping potentials characterized by

$$-(\alpha_x + \alpha_y) = \alpha_z > 0, \qquad \alpha'_x = -\alpha'_y, \qquad \alpha'_z = 0. \tag{3.2}$$

In this configuration, ions are confined in the z (axial) direction by a simple harmonic well, while in the x-y (radial) directions the confinement is dynamic. A classical treatment of the radial dynamics problem yields an equation of motion $m\ddot{x}_j = -e\left[V_{DC}\alpha_j + V_{RF}(t)\alpha'_j\right] x_j$ that may be rewritten in the form of the Mathieu equation,

$$\left[\frac{d^2}{d\xi^2} + \mathrm{a}_j - 2\mathrm{q}_j \cos(2\xi)\right] x_j = 0 \tag{3.3}$$

where we have introduced the dimensionless time $\xi = \Omega_{RF} t/2$ and voltages

$$\mathrm{a}_j = \frac{4eV_{DC}\,\alpha_j}{m\Omega_{RF}^2}, \qquad \mathrm{q}_j = \frac{2eV_{RF}\,\alpha'_j}{m\Omega_{RF}^2}. \tag{3.4}$$

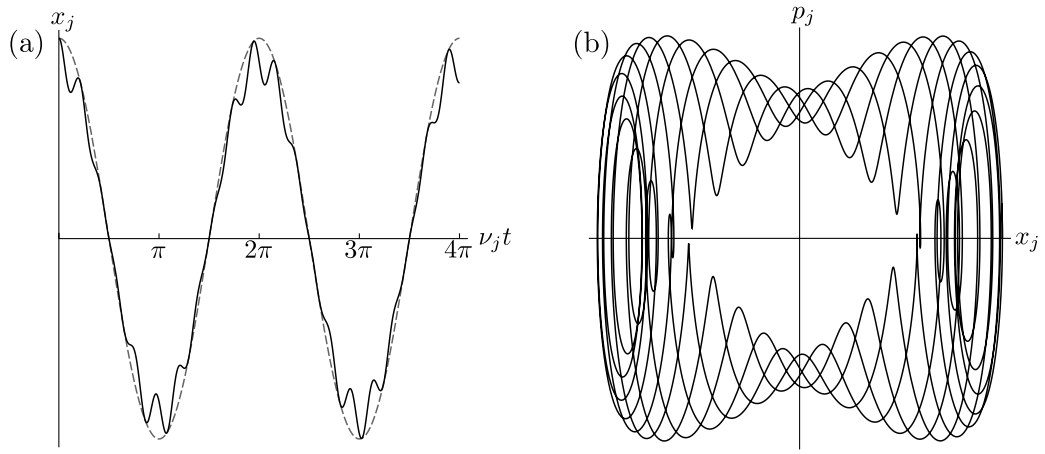

Figure 3.1: (a) Radial trajectory of a trapped ion with trapping parameters $\mathrm{q}_j = 0.25$, $\mathrm{a}_j = 0.016$. The motion is characterized by rapid micromotion oscillations at the RF drive frequency $\Omega_{RF} = 2\pi \times 50$ MHz and slow secular oscillations at the frequency $\nu_j = 2\pi \times 5.4$ MHz. The dashed curve is the harmonic trajectory at the secular frequency. (b) Phase space trajectory of the same solution.

The trapping parameters a_j, q_j determine the properties of the solutions. Not all solutions are stable, and three-dimensional confinement is only possible within a set of *stability regions* (see [77] for details). The stable solutions are quasiperiodic and can be studied using Floquet's theorem. In general, a quasiperiodic solution may be written as $x_j(\xi) = Au_j(\xi) + Bu_j^*(\xi)$ where A, B are constants determined by boundary conditions and

$$u_j(\xi) = \sum_{n=-\infty}^{\infty} C_{2n} \mathrm{e}^{\mathrm{i}\xi(2n+\mu_j)}, \tag{3.5}$$

and the complex conjugate $u_j^*(\xi)$ are linearly independent Floquet solutions of (3.3). The Floquet solutions are special functions related to the Mathieu sine $S(\mathrm{q}_j, \mathrm{a}_j, \xi)$ and cosine $C(\mathrm{q}_j, \mathrm{a}_j, \xi)$ functions by $u_j(\xi) = C(\mathrm{q}_j, \mathrm{a}_j, \xi) + \mathrm{i}\nu_j S(\mathrm{q}_j, \mathrm{a}_j, \xi)$, where $\nu_j = -\mathrm{i}\dot{u}_j(0)$ is called the *secular frequency* [80]. The characteristic exponent μ_j and the Fourier coefficients C_{2n} are determined by q_j, a_j and converge to $\sum_{n=-\infty}^{\infty} C_{2n} = 1$ so that $u_j(0) = 1$. The Fourier coefficients may be calculated by a recursion relation that yields solutions in the form of a continued fraction [81].

Most ion-trap quantum computing experiments work in the first stability region, where the parameters $\mathrm{a}_j \simeq 0$ and $\mathrm{q}_j < 0.908$ [77]. Provided that the trapping parameters are sufficiently small, the higher Fourier coefficients C_{2n} for $|n| > 1$ become negligible and (3.5)

simplifies to

$$u_j(t) \simeq \mathrm{e}^{\mathrm{i}\nu_j t}\frac{1+(\mathrm{q}_j/2)\cos(\Omega_{RF}t)}{1+\mathrm{q}_j/2} \tag{3.6}$$

where the secular frequency is very nearly $\nu_j \simeq \mu_j\Omega_{RF}/2$ and the characteristic exponent is nearly $\mu_j \simeq \sqrt{\mathrm{a}_j+\mathrm{q}_j^2/2}$ [80]. Then choosing $x_j = (x_0/2)\{u_j(t)+u_j^*(t)\}$ yields a quasiperiodic ion trajectory that satisfies the boundary conditions $x_j(0)=x_0$ and $\dot{x}_j(0)=0$. In this limit the radial motion may be decomposed into two components: a slow large-amplitude secular motion that oscillates at ν_j, and a superimposed small-amplitude micromotion that oscillates at the RF drive frequency. Figure 3.1 plots a typical radial trajectory of a trapped ion, illustrating both the secular motion and superimposed micromotion oscillations.

3.1.2 Quantum-mechanical treatment

A proper description of an ion-trap quantum computer requires a quantum mechanical treatment of ion motion. The axial component of the motion is harmonic and is described by a simple oscillator. An exact quantum solution of the radial components shows that in certain limiting cases the motion can be separated into slow, large-amplitude oscillations at the secular frequency ν_j and fast micromotion oscillations at Ω_{RF}. In a certain interaction frame the radial modes may be thought of as simple harmonic oscillators with a time-dependent phase related to the micromotion [82]. We will follow an elegant approach described by Roy Glauber [83] which cleverly constructs a radial phonon annihilation operator from Floquet solutions $u_j(t)$ and $u_j^*(t)$.

The motion along a radial axis is described by the Hamiltonian,

$$H_j(t) = \frac{p_j^2}{2m}+\frac{1}{2}m\omega_j^2(t)x_j^2 \tag{3.7}$$

where $\omega_j(t) = \frac{\Omega_{RF}}{2}\left\{\mathrm{a}_j-2\mathrm{q}_j\cos(\Omega_{RF}t)\right\}^{1/2}$ can be thought as a time-varying harmonic oscillator frequency. Using the Ehrenfest theorem we derive an equation of motion for the position operator, $\ddot{x}_j+\omega_j^2(t)x_j=0$, which is a quantum-mechanical analogue of the Mathieu equation (3.3). Therefore we assume a solution of the form $x_j(t)=Au_j(t)+Bu_j^*(t)$.

Since $u_j(t)$ and $u_j^*(t)$ are linearly independent, in general the solution $x_j(t)$ is independent of $u_j(t)$ or $u_j^*(t)$ but not both. We may apply Abel's identity or show by direct

computation that the Wronskian $W(u_j(t), u_j(t)^*) = u_j(t)\dot{u}_j(t)^* - u_j(t)^*\dot{u}_j(t) = 2\mathrm{i}\nu_j$ is a constant. Similarly if we assume $x_j(t)$ and $u_j(t)$ are both linearly independent solutions of the Mathieu equation (3.3) the operator

$$b_j(t) = b_j(0) = \mathrm{i}\sqrt{\frac{m}{2\hbar\nu_j}}\{u_j(0)\dot{x}_j(0) - x_j(0)\dot{u}_j(0)\} \tag{3.8}$$

is proportional to the Wronskian $W(u_j(t), x_j(t))$ and is also constant in time. Inserting $u_j(0) = 1$ and $\dot{u}_j(0) = \mathrm{i}\nu_j$ along with $\dot{x}_j = p_j/m$ into (3.8) yields

$$b_j = \sqrt{\frac{1}{2\hbar\nu_j m}}\{m\nu_j x_j(0) + \mathrm{i}p_j(0)\}, \qquad [b_j, b_j^\dagger] = 1, \tag{3.9}$$

which we immediately recognize as a boson annihilation operator. Then by solving for $x_j(0) = \sqrt{\hbar/2m\nu_j}\{b_j^\dagger + b_j\}$ and comparing to our trial solution for $x_j(t)$, it is simple to infer the general solutions for the position and momentum operators

$$x_j(t) = \sqrt{\frac{\hbar}{2m\nu_j}}\{b_j u_j^*(t) + b_j^\dagger u_j(t)\}, \qquad p_j(t) = \sqrt{\frac{\hbar m}{2\nu_j}}\{b_j \dot{u}_j^*(t) - b_j^\dagger \dot{u}_j(t)\}. \tag{3.10}$$

The radial modes behave similarly to a quantum harmonic oscillator, now with the simple periodic motion replaced with a quasiperiodic orbit. For most calculations, we may substitute the radial mode with a simple harmonic oscillator at the secular frequency [80].

3.1.3 Experimental implementation

A quantum computer should be scalable to many qubits and implement two-qubit entangling gates between arbitrary qubit parings. In one possible architecture [21], ion qubits are held in separate trapping wells and are transported to interaction regions, where two trapping wells are merged and laser pulses entangle ion qubit pairs using common motional modes (see section 3.3.3). This scheme requires fine control of the positions of many ions, and trap geometries compatible with ion reordering [84].

Microfabricated surface-electrode traps meet these requirements [22, 28, 30, 85]. In these traps, electrodes lie in a common plane and produce a local quadrupolar field above the surface of the trap. We use a five-wire electrode geometry which is related to the traditional three-dimensional quadrupole geometry by a certain conformal map [86]. The DC electrode "wires" are segmented into individually controllable electrodes which are biased to create

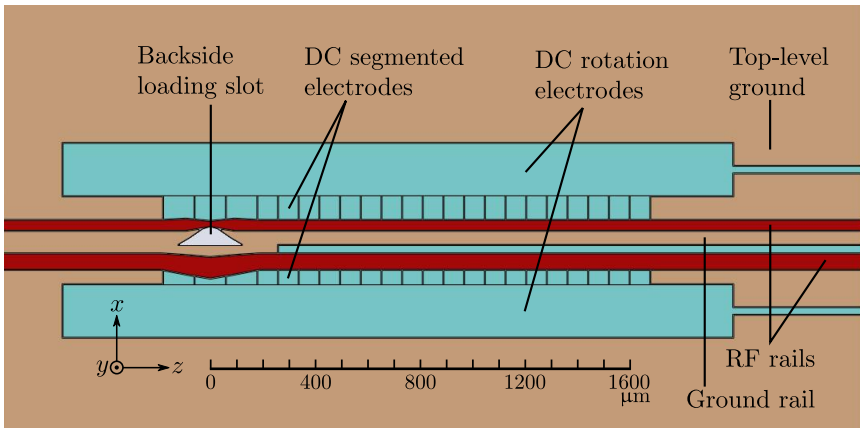

Figure 3.2: Trapping region of the GTRI Gen II surface-electrode trap.

several trapping wells in a single device. Ion transport along the trap axis is achieved by smoothly adjusting the DC potentials [31, 34, 85]. A similar procedure can merge or separate trapping wells. Microfabrication techniques allow the construction of many identical traps, and also permit complicated geometries with junction elements for ion reordering.

Figure 3.2 shows the trapping region of a microfabricated surface-electrode ion trap developed locally at GTRI [32]. Our traps are fabricated from three sputtered 99% Al / 1% Cu layers separated by insulating SiO_2 films. The lowermost aluminum layer forms a ground plane that prevents RF electric fields from penetrating into the lossy Si substrate. We lithographically pattern a second metal layer to form trapping electrodes, electrode leads, and bottom plates of integrated capacitive RF filters that shield the DC wires from unwanted RF pickup. The topmost aluminum layer forms a second ground plane and serves as the top plates for the on-chip $\simeq 60$ pF capacitors. Some trap designs feature large DC "rotation electrodes" fabricated from this layer. These electrodes are typically used to adjust the orientation of the radial motional axes relative to the trap plane for efficient Doppler cooling. The topmost layer is removed from a portion of the trapping region, exposing the underlying trapping electrodes. Each trap design uses a similar fabrication process, described in detail in section 8.2.

3.1.3.1 Electrical connections for trap electronics

Our RF source is an amplified signal generator which we filter using a $Q \simeq 60$ helical resonator. Modest RF potentials ($V_{RF} \sim 100$ V peak-to-peak, $\Omega_{RF} \simeq 2\pi \times 50$ MHz for $^{40}Ca^{+}$) provide strong radial confinement, achieving secular frequencies of about $\nu_{x,y} \simeq 2\pi \times 5$ MHz. DC voltages of about $V_{DC} \leq 10$ V achieve axial secular frequencies around $\nu_z \simeq 2\pi \times 1$ MHz.

We apply DC potentials using a system of independent digital-to-analog converters (DACs) which update in parallel during ion transport[1]. Typically, we update DAC voltages at 500 kHz and trigger the start of a transport event with a transistor-transistor logic (TTL) pulse controlled by a field-programmable gate array[2] (FPGA) which serves as the experiment scheduler (see section 3.2.4.3). The DC voltages are filtered using low-pass Butterworth filters with a corner frequency of $2\pi \times 40$ kHz. The filters both smooth transport potentials and suppress noise pickup on the DC lines. Transport potentials are created from DC potential sets that produce an axial well at a regular interval (typically every 10 μm) throughout the trap. Intermediate locations are handled by linearly interpolating DC values between neighboring potential sets.

A network of traces route electrical connections from the trap electrodes to bondpads at the edge of the die. After dicing, each trap fits on a 11×11 mm^2 chip. We mount chips to a 100-pin ceramic pin grid array[3] (CPGA) carrier with a 1.2 mm thick slotted alumina spacer with 80% Au / 20% Sn solder. The spacer raises the height of the chip surface above the CPGA edge to ensure laser access. We use a wirebonder to wedge-bond two redundant 25 μm diameter Al wires connecting the chip bondpads to the CPGA.

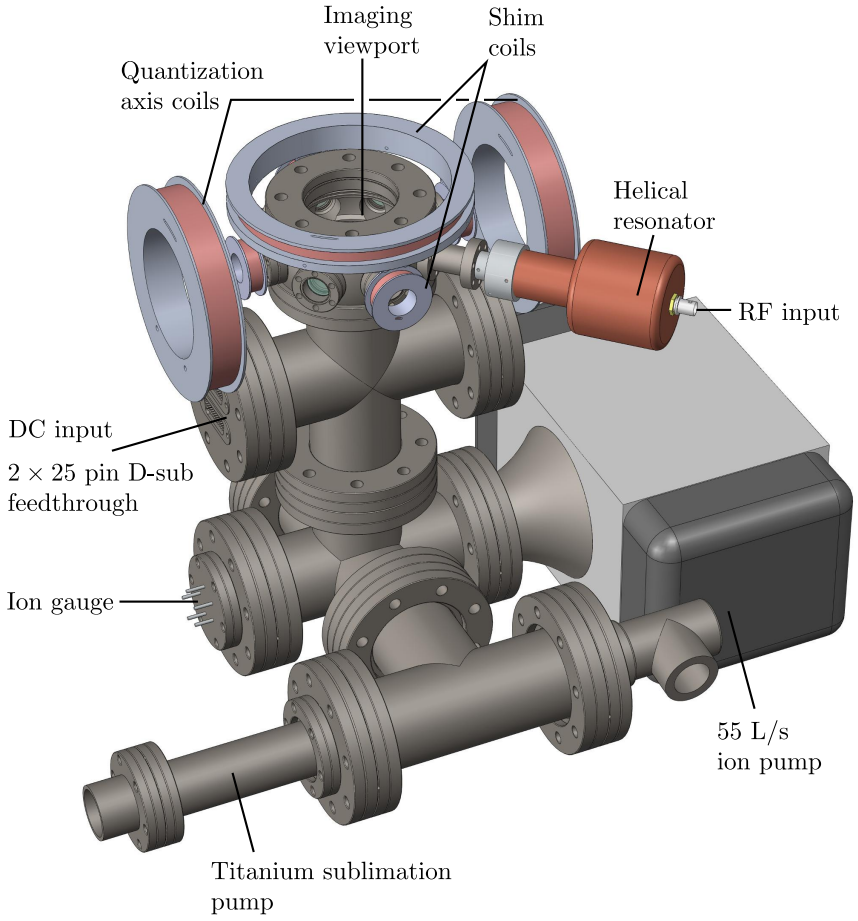

Figure 3.3: A vacuum apparatus for surface-electrode traps. The ion trap is mounted onto a 100-pin CPGA which plugs into a socket underneath the imaging viewport. The socket routes 96 independent DC connections to four 25-pin D-subminiature feedthroughs, and the RF connections to a feedthrough attached to the helical resonator. A feedthrough provides electrical connections for the Ca or Yb ovens. Six AR-coated windows provide laser access. A five-way cross attaches an ion gauge for pressure readout, a titanium sublimation pump, and a 55 L/s ion pump. The vacuum system achieves pressures below 10^{-11} torr.

3.1.3.2 Vacuum chamber for surface-electrode traps

Figure 3.3 shows an ultra-high vacuum (UHV) chamber used in ion trapping experiments. The ion-trap CPGA plugs into a socket interface housed in a 4.5" diameter spherical octagon[4] near the top of the chamber. Six octagon ports attach anti-reflection (AR) coated windows[5], providing three laser axes parallel with the trap surface. We use the large viewport[6] directly above the CPGA for camera access. The socket routes electrical connections to various feedthroughs in the vacuum chamber. The socket connects 96 independent DC pins to two separate 2×25 pin CF-flange feedthroughs via Kapton© coated wires. A pair of wires connect the RF pins to a feedthrough attached to an octagon port. A second feedthrough provides a DC ground which connects via a wire to a mesh ground shield assembly that clips onto the CPGA. The ground shield surface is 4 mm above the trap surface, and protects trapped ions from stray electric fields.

The ground shield feedthrough also provides electrical connections for neutral atomic beam ovens used during ion loading. The ovens are mounted to the socket assembly behind the ion-trap. During loading, neutral flux passes from the backside through a loading slot that pierces the trap substrate [85, 87]. The backside loading arrangement avoids coating trap surfaces with neutral atoms. Above the trap surface, atoms pass through two intersecting laser beams which eject an electron via a resonant two-photon process. The photoionization process is isotopically selective, and we deterministically load a particular isotope by adjusting the laser frequency.

Low pressure is required to avoid ion loss from collisions with residual background gas. We use a 55 L/s ion pump[7] and an auxiliary titanium sublimation pump[8] to achieve pressures below 10^{-11} torr. In practice, the titanium sublimation pump is only used during the last stages of chamber bakeout or to clean the chamber after several months of use.

[1]National Instruments, NI PXI-6733
[2]Xilinx, Spartan 3E
[3]Spectrum semiconductor materials, CPG 10039
[4]Kimball physics, MCF450-SphOct-E2A8
[5]Kurt J. Lesker, VPZL-133
[6]Kurt J. Lesker, VPZL-450
[7]Varian, StarCell 55
[8]Varian, 916-0009

The pumping section of the chamber attaches via a five-way cross, which also houses a hot-filament ion gauge for monitoring the pressure during bakeout.

3.2 Internal degrees of freedom

Ion-trap quantum computers store information in the internal states of trapped atomic ions. In this section we describe the internal structure of trapped-ion qubits, the process of qubit initialization and readout, and the laser systems used to control atomic ions.

3.2.1 Choosing an ion

An appropriate ion should have a strong closed optical transition for laser cooling, qubit state initialization, and for fluorescence readout. In practice this requires an ion with a single valence electron, typically alkaline-earth metals (Be^+, Mg^+, Ca^+, Sr^+, and Ba^+) or certain transition metals (Zn^+, Cd^+, Hg^+, and Yb^+) [88]. Although multiply ionized species may work in principle, most require transitions in the deep UV outside the current range of laser and detector technologies. In addition to a cooling transition, an ion should have a pair of long lived states to serve as a qubit. Practically speaking, this requires two metastable states not coupled by an electric dipole transition. However, to perform gates we must control qubits through some coherent process, such as an optical quadrupole, microwave, or perhaps Raman process. In this thesis, we use both $^{40}Ca^+$ ions and $^{171}Yb^+$ ions as physical qubits.

3.2.2 The $^{40}Ca^+$ qubit

Figure 3.4 shows the electronic structure of the $^{40}Ca^+$ ion. We select two metastable states, $|1\rangle = (^2S_{1/2},\ m_J = -1/2)$ and $|0\rangle = (^2D_{5/2}, m_J = -5/2)$ to represent a qubit. A weak magnetic field (typically $|\mathbf{B}| \simeq 0.4$ mT) lifts the degeneracy of Zeeman sublevels and serves as a quantization axis. Decay from the metastable $^2D_{5/2}$ manifold is slow since the transition back to the ground state is forbidden by dipole selection rules. Therefore, this choice of qubit states forms an acceptable quantum memory [89].

We use an external-cavity diode laser[9] (ECDL) at $\lambda = 397$ nm to address the strong

[9]Toptica, DL 100. We use this model for all lasers except for the 423, and 729 nm lasers.

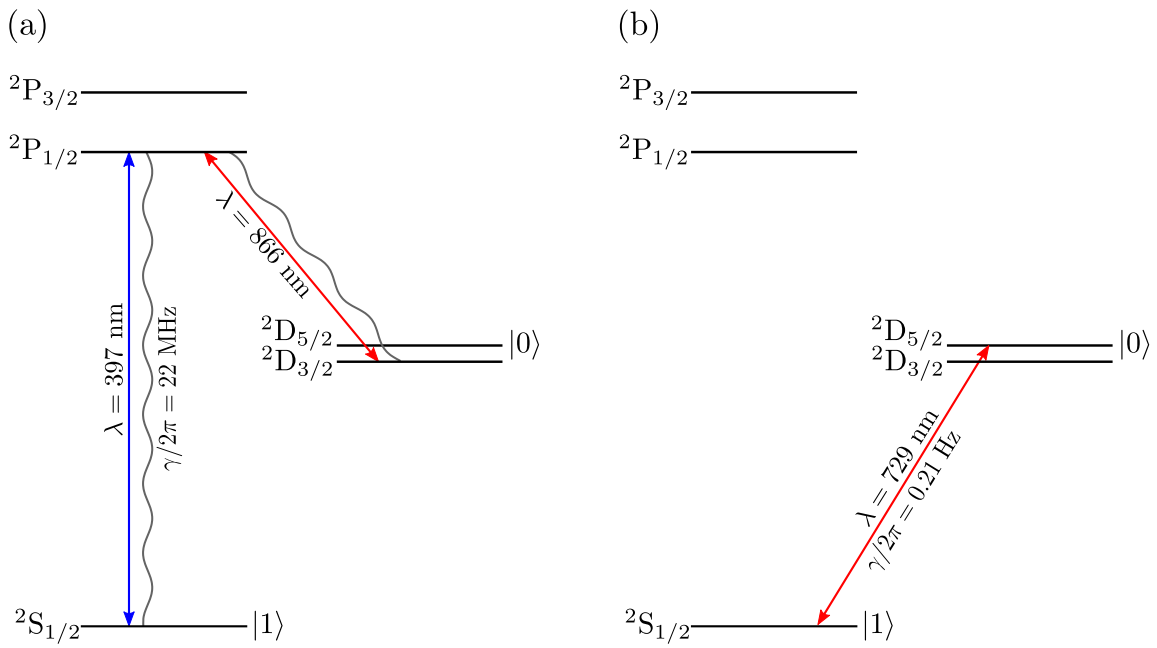

Figure 3.4: Electronic structure of the $^{40}Ca^+$ ion. (a) Laser configuration for Doppler cooling, fluorescence measurement, and optical pumping into the $|1\rangle = (^2S_{1/2}, m_J = -1/2)$ qubit state. Ions are cooled and imaged using the 397 nm $^2S_{1/2} \rightarrow {}^2P_{1/2}$ transition. A repump laser at 866 nm prevents trapping in the metastable $^2D_{3/2}$ level. (b) Laser configuration for qubit operations. A narrow linewidth 729 nm laser drives an electric quadrupole transition between $|1\rangle \rightarrow |0\rangle = (^2D_{5/2}, m_J = -5/2)$.

$^2S_{1/2} \rightarrow {}^2P_{1/2}$ transition during Doppler cooling [90], state preparation, and qubit state detection [91]. The Doppler cooling 397 nm beam is unpolarized to avoid pumping the ion into a dark Zeeman sublevel of the $^2S_{1/2}$ manifold. Once excited to $^2P_{1/2}$, the ion quickly decays into the $^2S_{1/2}$ or the metastable $^2D_{3/2}$ state with a branching ratio 18:1. To prevent population trapping in the metastable state, a second ECDL at $\lambda = 866$ nm repumps along $^2D_{3/2} \rightarrow {}^2P_{1/2}$, effectively closing the cooling cycle. Sideband cooling uses a third ECDL at $\lambda = 854$ nm that drives the $^2D_{5/2} \rightarrow {}^2P_{3/2}$ transition [92, 93].

Qubit state preparation uses a similar arrangement of lasers. We use a second $\hat{\sigma}_-$ polarized 397 nm state-preparation beam along with the 866 nm repump beam to initialize the qubit state by optical pumping [94]. As the ion scatters photons it eventually decays into $|1\rangle$, which is dark to this choice of polarizations. We calibrate the state preparation by monitoring the scattered fluorescence signal with a photomultiplier tube[10] (PMT) as a function of optical pumping time.

We use a narrow linewidth ($\gamma \simeq 150$ Hz) laser[11] to drive the $^2S_{1/2} \rightarrow {}^2D_{5/2}$ electric quadrupole transition at $\lambda = 729$ nm. We resolve spectral lines corresponding to transitions between individual magnetic sublevels, including the $\Delta m_J = -2$ transition that couples the qubit states $|1\rangle \rightarrow |0\rangle$. By driving the qubit transition we may selectively transfer population between the qubit states, implementing quantum gates. This subject is treated in detail in section 3.3.

Qubit readout uses a state-selective fluorescence measurement to discriminate between "bright" and "dark" qubit states. We apply the unpolarized 397 nm beam with the 866 nm repump and record the number of 397 nm photons that arrive at a PMT during a detection interval (typically between 400 μs and 1 ms). The qubit decoheres (that is, collapses in the Copenhagen interpretation) and we observe two outcomes: either the ion scatters very few photons and the qubit is in $|0\rangle$ or the ion scatters many photons and the qubit is in $|1\rangle$. By repeating a measurement many times (typically $n = 400$) for the same qubit preparation, we extract a population from the fraction of measurements which observe a particular state.

[10] Hamamatsu, H7360-02

[11] New Focus 7004 slave laser injection locked to a stabilized Toptica DL 100

3.2.3 The $^{171}Yb^{+}$ qubit

Figure 3.5 shows the electronic structure of the $^{171}Yb^{+}$ ion. This isotope has a nuclear spin $I = 1/2$ which introduces hyperfine structure when coupled with the electronic angular momentum. The qubit uses two hyperfine "clock" states on the $^2S_{1/2}$ ground state manifold, $|0\rangle = (^2S_{1/2}, F = 0, m_F = 0)$ and $|1\rangle = (^2S_{1/2}, F = 1, m_F = 0)$, where $F = I + J$ is the total angular momentum. Again we use a weak magnetic field to split magnetic levels and to act as a quantization axis. At zero magnetic field, the splitting between the qubit levels is first-order insensitive to magnetic field noise [95], providing the qubit with excellent information storage properties. Recent experiments have demonstrated qubit coherence times exceeding several seconds in this system.

The hyperfine interaction introduces a splitting on the order of a few GHz between states with differing total angular momentum quantum numbers. This hyperfine splitting further complicates laser cooling, since sufficiently narrow lasers frequently address only one angular momentum sub-manifold at a time. To simultaneously address multiple angular momentum states, we use a system of electro-acoustic modulators (EOMs) to produce frequency sidebands on the main laser frequency. Then, by selectively switching EOMs we may prepare our lasers for Doppler cooling, qubit initialization, or qubit readout. Our system closely follows the design of Olmschenk *et al.* [95].

The laser configuration for Doppler cooling is shown in figure 3.5a. We cool the ion using an unpolarized beam from an ECDL[9] at $\lambda = 369$ nm to address the $^2S_{1/2}\,(F = 1) \rightarrow {}^2P_{1/2}\,(F = 0)$ transition. A second-order frequency sideband produced by the 7.37 GHz "Doppler cooling" EOM[12] drives the $^2S_{1/2}\,(F = 0) \rightarrow {}^2P_{1/2}\,(F = 1)$ transition. Once excited to $^2P_{1/2}$, the ion decays to $^2S_{1/2}$ or to $^2D_{3/2}$ with a branching ratio of 200:1. To prevent population trapping in the metastable $^2D_{3/2}$ level, we use an unpolarized repump laser at $\lambda = 935$ nm to drive the $^2D_{3/2}(F = 1) \rightarrow {}^3[3/2]_{1/2}(F = 0)$ transition and return the ion to $^2S_{1/2}\,(F = 1)$ by radiative decay. A second "repump" EOM[13] at 3.07 GHz produces a frequency sideband on the 935 nm laser that drives the $^2D_{3/2}\,(F = 2) \rightarrow {}^3[3/2]_{1/2}\,(F = 1)$

[12] New Focus, 4851
[13] New Focus, 4431

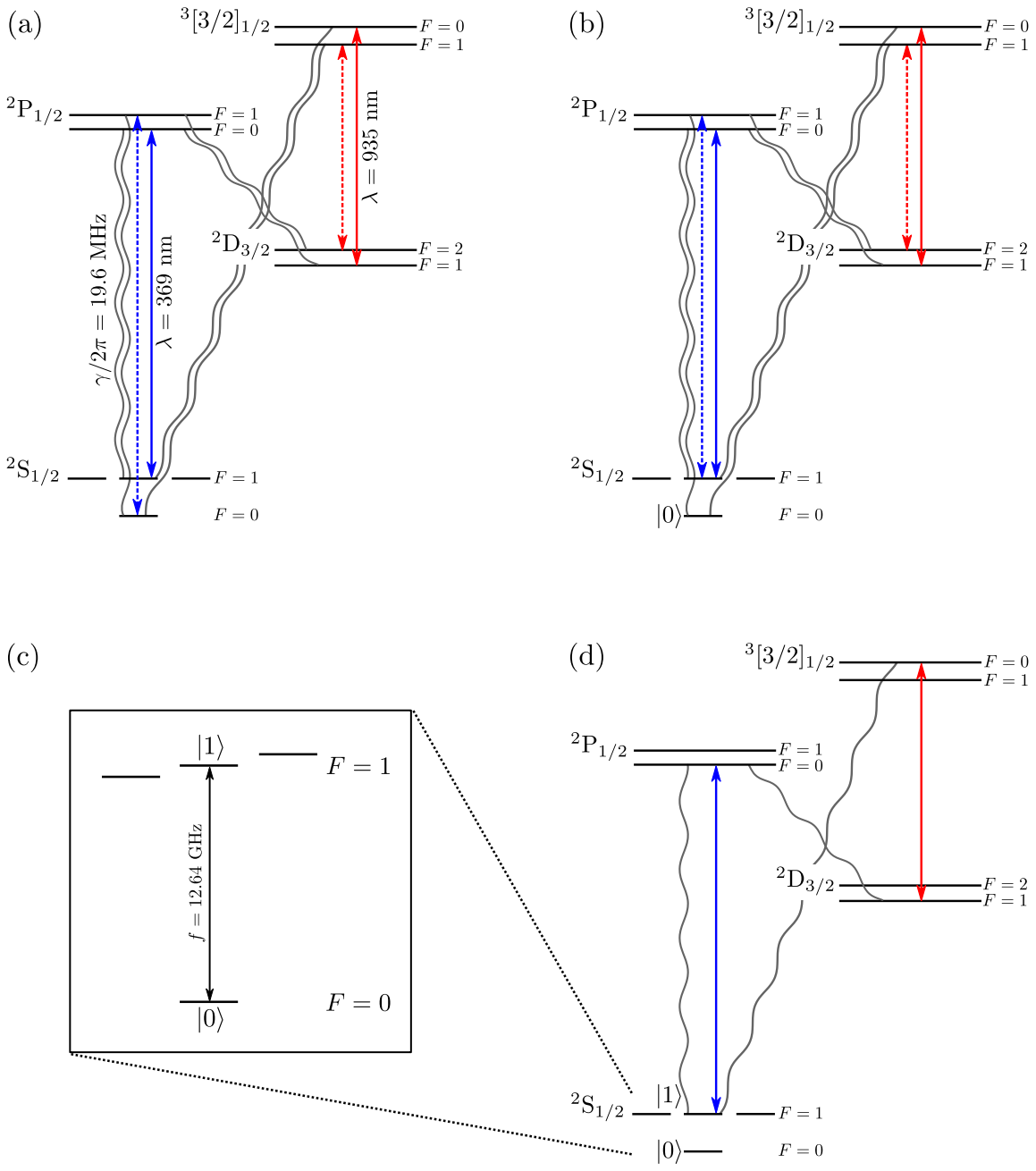

Figure 3.5: Electronic structure of the $^{171}Yb^+$ ion. Laser configurations for (a) Doppler cooling, (b) state preparation, and (d) qubit detection by a fluorescence measurement. Solid lines designate transitions driven by a central laser frequency, while dashed lines are transitions driven by sidebands introduced by an EOM. Curved lines mark states linked by a decay process. Ions are imaged and cooled using the 369 nm $^2S_{1/2} \rightarrow {}^2P_{1/2}$ transition. A repump laser at 935 nm prevents population trapping in $^2D_{3/2}$. (c) During gates a 12.64 GHz microwave field drives the magnetic dipole transition between $|0\rangle \rightarrow |1\rangle$.

transition and returns the ion to the $^2S_{1/2}\,(F=0)$ or $F=1$ states after emitting a photon. This choice of laser frequencies avoids the production of dark states that trap population and shut off the Doppler cooling process.

Qubit state preparation uses a similar arrangement of lasers (figure 3.5b), only now we switch off the "Doppler cooling" EOM and instead modulate the 369 nm beam with an independent 2.10 GHz "state preparation" EOM[13], producing a frequency sideband that drives the $^2S_{1/2}\,(F=1) \rightarrow {}^2P_{1/2}\,(F=1)$ transition. The 935 nm repump beam and EOM are still applied. As the ion scatters photons it eventually decays into $|0\rangle$ and becomes dark. Similar to state preparation in $^{40}Ca^+$, we calibrate the optical pumping time (usually $\tau_{\text{pump}} = 4$ μs) by monitoring the scattered fluorescence signal with a PMT.

Quantum gates require an interaction that couples the qubit states. For hyperfine qubits, this coupling is usually provided by a controlled microwave field, or by a pair of Raman lasers tuned so that the difference frequency is near the hyperfine splitting. We currently use the former method; a 12.64 GHz microwave field resonantly drives the $^2S_{1/2}\,(F=0) \rightarrow {}^2S_{1/2}\,(F=1)$ magnetic dipole transition (figure 3.5c). By tuning the microwave frequency and polarization, we resolve spectral lines corresponding to transitions between individual magnetic sublevels, and can selectively drive the $\Delta m_F = 0$ qubit transition.

Qubit readout uses a laser arrangement (figure 3.5d) where the 369 nm and 935 nm EOMs are all shut off [95, 96]. The resulting configuration selectively scatters 369 nm photons when the ion is prepared in the $^2S_{1/2}\,(F=1)$ manifold, which includes the $|1\rangle$ qubit state. Resonant photon scattering events only occur by driving the ion through $F=0$ excited states. Since transitions between two $F=0$ states are forbidden by angular momentum selection rules, the ion cannot decay into the dark qubit state $|0\rangle = {}^2S_{1/2}\,(F=0, m_F=0)$. We record the number of 369 nm photons counted by a PMT during a detection interval (again, typically between 400 μs and 1 ms). For a general qubit preparation we observe two outcomes: either the ion scatters many photons and the qubit is in $|1\rangle$, or the ion is dark and the qubit is in $|0\rangle$. By repeating a measurement several times for a given qubit preparation, we extract a population fraction and a standard error for the measurement.

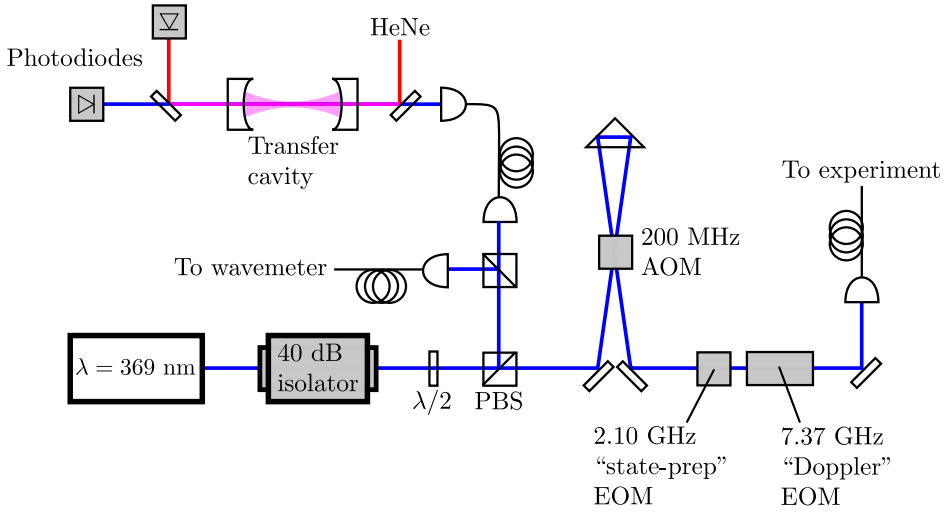

Figure 3.6: Schematic of the 369 nm laser system for $^{171}Yb^{+}$. A polarizing beam splitter picks off a portion of the beam ($P \sim 100$ μW) for the transfer cavity and wavemeter. The transmitted beam is modulated by a 200 MHz AOM in the double pass configuration, and two EOMs which produce frequency sidebands to address hyperfine structure. The beam is sent to the experiment via a polarization-maintaining optical fiber.

3.2.4 Experimental laser control

3.2.4.1 Frequency stabilization

Ion-trap quantum computers require stable laser sources for ion loading, cooling, qubit initialization and control. We use three methods for frequency stabilization. For coarse frequency control, we use a wavemeter[14] to monitor the laser frequency to a quoted $3\sigma \leq$ 60 MHz accuracy. A simple software lock generates a feedback signal that stabilizes the laser frequency by modulating the ECDL piezo voltage. Our resonant $\lambda = 399$ nm laser for $^{171}Yb^{+}$ photoionization is stabilized using this method.

Lasers for Doppler cooling and repumping require more accurate frequency control. We align an unstable laser to a low finesse $\mathcal{F} \leq 100$ transfer cavity referenced to a stabilized HeNe laser[15] with a maximum frequency drift 1 MHz/hr [97, 98]. We monitor the transmission of light through the cavity while scanning the cavity length over a HeNe free-spectral range. Then, by locking the relative positions of the transmission maxima by feedback to

[14]High Finesse, WS-7
[15]Research Electro Optics, 32732

the ECDL piezo voltages, we map the stability of the reference laser to the locked lasers. The 397, 423, 866, and 854 nm lasers for $^{40}Ca^{+}$ are locked to a common cavity; an identical cavity locks the 369, and 935 nm $^{171}Yb^{+}$ lasers. Figure 3.6 illustrates the 369 nm laser system, including the transfer lock cavity. We routinely stabilize our lasers to better than ≤ 5 MHz using this method.

The stability requirements are most severe for the 729 nm qubit logic laser used in $^{40}Ca^{+}$. We lock the 729 nm laser using the Pound-Drever-Hall method [99] to an external ultra-low expansion (ULE) high finesse cavity $\mathcal{F} \leq 10^5$ purchased from Advanced Thin Films. We achieve a 729 nm laser linewidth of about 150 Hz.

3.2.4.2 Rapid laser switching and control

Fast laser switching, power, phase, and frequency control is achieved using a system of acousto-optic modulators[16] (AOMs). The AOMs impart a frequency and phase shift on the laser which depends on an RF drive signal. For these applications we use reprogrammable direct-digital synthesizers[17] (DDSs) as an RF frequency source ($\omega_{RF} \simeq 2\pi \times 200$ MHz). Then by adjusting the digital RF signal, we achieve control of laser pulses. The 397, 854, and 729 nm lasers for $^{40}Ca^{+}$ are controlled using AOMs. For $^{171}Yb^{+}$ only the 369 nm laser uses an AOM. Typically the AOMs are set up in the double-pass cat-eye configuration to avoid beam steering issues.

3.2.4.3 Experiment timing and pulse control

We require a timing system to control laser pulses, ion transport DACs, PMTs and other measurement devices. The pulse control system consists of two parts: a scheduler responsible for triggering events and recording results, and a controller for the DDS boards used to modulate laser pulses. The heart of the system is a Spartan 3E FPGA, which we access using a breakout board[18]. The FPGA stores an instruction set (pulse program) which schedules experimental events. During an experiment, the FGPA sequentially triggers devices using carefully timed TTL pulses. One input pin receives signal from the PMT, allowing for the

[16] Brimrose, TEM 200-50
[17] Analog Devices, AD-9910
[18] Sparkfun, DEV-08458

FPGA to record the number of detected photons during a qubit measurement event. The FPGA is clocked at 50 MHz.

The FPGA also controls the DDS sources using a high-speed serial port to reprogram the DDS amplitude, frequency, and phase. A TTL pulse triggers the DDS board to switch the generated RF signal. The DDS programming occurs in about 1 μs. To avoid this delay, we sometimes store the parameters for multiple pulses in the DDS on-board memory. In this mode of operation, the DDS switches between up to four pre-programmed settings. The DDS internal clock runs at 1 GHz; this clock signal is divided by 16 and sent to the FPGA to synchronize events. Some applications require multiple synchronized DDS sources; in these cases the output of a single "master" DDS clock is sent to a clock distribution board, where it is routed to synchronize multiple "slave" DDS boards.

3.2.5 Experimental microwave control

We currently use 12.64 GHz microwaves to drive qubit gates in $^{171}Yb^{+}$. Our system uses two independent microwave fields, which we interfere near the ion to achieve polarization control (see section 6.1.3). A signal generator[19] provides a stable microwave source approximately 300 MHz blue-detuned from the qubit transition frequency. The signal is split to supply the local oscillator inputs to two frequency mixers. The intermediate frequency signals are provided by two synchronized DDS signals at 300 MHz. The mixers reject the carrier frequency and produce sidebands spaced by the DDS signal frequency. One sideband is tuned to match the qubit frequency, while the other is far off resonance. Each microwave signal is amplified using a high-power microwave amplifier[20] and delivered to the experiment via low-loss coaxial cables.

3.3 Quantum logic gates

Here we discuss the application of quantum gates using a near-resonant laser or microwave field. Ions experience momentum kicks during the absorption and emission of photons. In certain cases, this effect may be used to achieve quantum control of both the motional and

[19] Agilent, 83623B
[20] Mini-Circuits, ZVE-3W-183+

internal states of atomic ions. Section 3.3.1 describes the ion–laser interaction. Sec. 3.3.2 describes single-qubit gates. Sec. 3.3.3 describes multi-qubit gates which rely on shared motional modes to entangle ions.

3.3.1 The ion–laser interaction

The system we consider is a chain of ions trapped in a common harmonic potential well. For simplicity, we consider only the qubit transition and treat each ion as a two level system. Due to mutual Coulomb repulsion, the motions of individual ions in the chain are coupled; however, the total motion can be decomposed into a set of orthogonal modes which act as independent oscillators. An appropriate Hamiltonian for the ion chain is $H' = \sum_i H_i + \sum_j H_j$ where $H_i = \hbar\omega_i Z_i/2$ is the internal Hamiltonian of the ith ion and $H_j = \hbar\nu_j(b_j^\dagger b_j + 1/2)$ describes the jth collective motional mode. Under evolution by H' the internal states of the qubits do not become entangled with the motion.

We apply a laser to address the qubit transition during quantum gates. The laser is described by a single-mode traveling plane wave which couples to internal states of each ion. In the laboratory frame the net Hamiltonian is

$$H = H' + \hbar\sum_i \Omega_i \left(\sigma_i + \sigma_i^\dagger\right)\cos\left(\mathbf{k}\cdot\mathbf{x}_i - \omega t - \phi\right) \tag{3.11}$$

where $\sigma_i = |1_i\rangle\langle 0_i|$ is the qubit lowering operator, $\mathbf{x}_i = (x_i, y_i, z_i)$ is the Cartesian coordinate, and Ω_i is the Rabi frequency of the ith ion [80, 100]. By choosing an interaction frame generated by H' and applying the rotation-wave approximation we may rewrite (3.11) as

$$H_I = \frac{\hbar}{2}\sum_i \Omega_i \sigma_i^\dagger\, \mathrm{e}^{-\mathrm{i}(\omega-\omega_i)t}\, \mathrm{e}^{-\mathrm{i}\phi}\, \mathrm{e}^{\mathrm{i}\chi_i} + \text{h.c.}, \tag{3.12}$$

where now the spatial dependence is carried by the operator $\chi_i = (U')^\dagger \mathbf{k}\cdot\mathbf{x}_i(U')$ and the normal oscillator terms in the transformation propagator $U' = \exp(-\mathrm{i}H't/\hbar)$ modify the ion coordinate terms. If it were not for the interaction provided by χ_i the qubits in (3.12) would remain uncoupled.

Observe that the ion coordinate x_ℓ may be written in terms of the oscillator normal modes by a linear transformation $x_\ell = \sum_j Q_{\ell j} q_j$. Also, we may replace $q_j = \lambda_j(b_j + b_j^\dagger)$, where the lengthscale $\lambda_j = \sqrt{\hbar/2m\nu_j}$ corresponds to the width of the ground-state oscillator

wavefunction. These substitutions allow the transformation $\chi_i = (U')^\dagger \mathbf{k}\cdot\mathbf{x}_i(U')$ to be carried out analytically. The result is

$$\chi_i = \sum_j \eta_{ij} \left(b_j e^{-i\nu_j t} + b_j^\dagger e^{i\nu_j t} \right), \tag{3.13}$$

where $\eta_{ij} = \sum_\ell k_\ell Q_{\ell j} \lambda_j$, called the *Lamb-Dicke parameter*, is proportional to the overlap of the photon wavevector $\mathbf{k}$ with the jth oscillator mode. The Lamb-Dicke parameter sets the rate of momentum exchange between the laser field and the motional modes of the ion chain. In typical experiments on $^{40}Ca^+$ qubits, where qubit operations use the 729 nm electric quadrupole transition, the Lamb-Dicke parameters are on the order of $\eta_{ij} \sim 10^{-2}$ to 10^{-1}. However, for gates in $^{171}Yb^+$ the momentum carried by free-space microwave photons is much lower, yielding Lamb-Dicke parameters on the order of $\eta_{ij} \sim 10^{-6}$.

3.3.1.1 The Lamb-Dicke regime

The Hamiltonian (3.12) describes the complete set of interactions we may apply to an ion chain using a single laser beam; however, it can be cumbersome to use. Fortunately, an exact treatment is often unnecessary. The Hamiltonian is considerably simplified if the $\exp(i\chi_i)$ term is replaced with a perturbative expansion in powers of the Lamb-Dicke parameters,

$$\begin{aligned} e^{i\chi_i} = 1 + i \sum_j \eta_{ij} \left(b_j e^{-i\nu_j t} + b_j^\dagger e^{i\nu_j t} \right) + \\ - \sum_{jk} \frac{\eta_{ij}\eta_{ik}}{2} \left(b_j e^{-i\nu_j t} + b_j^\dagger e^{i\nu_j t} \right) \left(b_k e^{-i\nu_k t} + b_k^\dagger e^{i\nu_k t} \right) + O(\eta_{ij}^3). \end{aligned} \tag{3.14}$$

The phonon coupling introduces frequency sidebands spaced by integer multiples of the mode frequency from the qubit transition frequency. If the spectral line is sufficiently narrow to resolve the motional sidebands (see figure 3.7), we may tune the laser to resonantly drive a particular interaction, while off-resonant terms oscillate rapidly and contribute negligibly to the dynamics. When considered with the Hamiltonian (3.12) we identify three classes of spectral components.

Carrier transitions: When $\omega = \omega_i$ the laser is resonant with the qubit transition. The carrier transition closely resembles the qubit transition for a free (untrapped) ion, with only minor second-order corrections to account for motional effects. Fast oscillating terms

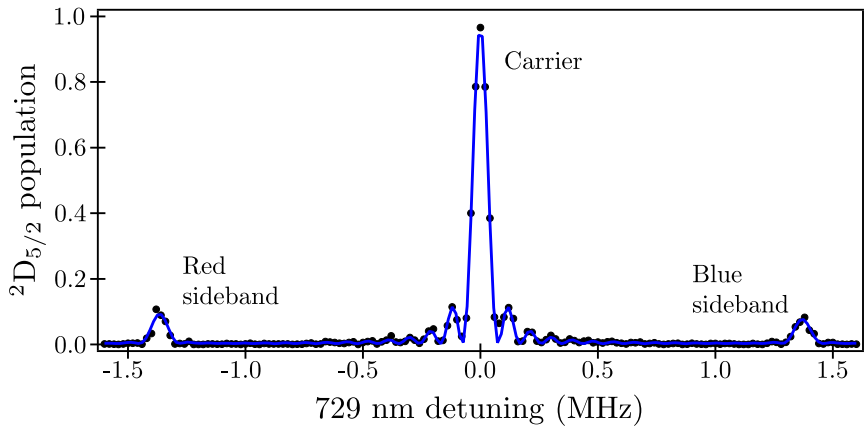

Figure 3.7: Spectrum of the qubit transition for a single $^{40}Ca^+$ ion with resolved axial sidebands. In this experiment, $\Omega_i = 2\pi \times 96$ kHz, $\nu_z = 2\pi \times 1.37$ MHz, and $\eta_{iz} = 0.18$. The radial sidebands are at $\nu_x = 4.70$ MHz and $\nu_y = 5.46$ MHz and are outside the range of the scan.

in (3.14) average out, leaving only terms which preserve the total phonon number. This averaging simplifies the Hamiltonian to

$$H_{\text{Carrier}} = \frac{\hbar}{2} \sum_i \left(\tilde{\Omega}_i \sigma_i e^{i\phi} + \tilde{\Omega}_i^\dagger \sigma_i^\dagger e^{-i\phi} \right), \tag{3.15}$$

where the effective Rabi frequency

$$\tilde{\Omega}_i = \Omega_i - \Omega_i \sum_{jk} \frac{\eta_{ij}\eta_{ik}}{2} \left(b_j b_k^\dagger e^{i(\nu_k - \nu_j)t} + b_j^\dagger b_k e^{i(\nu_j - \nu_k)t} \right) + O(\eta_{ij}^4) \tag{3.16}$$

now depends on the motional state of the ion chain. The second-order terms in (3.16) either swap phonons between modes ($j \neq k$) or preserve the current occupations ($j = k$).

It is also apparent that "hot ions" with a high motional quantum number evolve with a slower effective Rabi frequency. For example, for a single mode in the motional ground state the effective Rabi frequency is $\langle \tilde{\Omega}_i \rangle = \Omega_i(1 - \eta_{ij}^2/2)$; however, with n phonons the Rabi frequency is $\langle \tilde{\Omega}_i \rangle = \Omega_i(1 - \eta_{ij}^2(n + 1/2))$. Of course in general, the ion chain does not exist in a state with well-defined phonon numbers in each mode, rather it exists in a superposition. In these states each component of the motional wavefunction rotates at a slightly different Rabi frequency, leading to a destructive interference known as *motional dephasing*. This destructive interference becomes an important source of error in quantum computing experiments.

To avoid motional dephasing and other negative effects, most quantum gates are performed in the *Lamb-Dicke regime* where $\eta_{ij}^2(2\langle n\rangle + 1) \ll 1$. This represents the domain where the motional wavepacket is much smaller than the wavelength of the laser light, and where second-order and higher motional contributions are negligible. Typically the Lamb-Dicke regime is reached by sideband cooling the ion chain to the motional ground state or by using a laser arrangement where the Lamb-Dicke parameters are small.

Red sidebands: The motion of the ion chain induces sidebands on the main carrier transition, separated in frequency by integer multiples of the mode secular frequency ν_j. When $\omega = \omega_i - \nu_j$ the laser is resonant with the first-order red motional sideband and the Hamiltonian (3.12) simplifies to

$$H_{\mathrm{RSB}} = -\mathrm{i}\frac{\hbar}{2}\sum_{ij}\Omega_i\eta_{ij}\left(\sigma_i b_j^\dagger \mathrm{e}^{\mathrm{i}\phi} - \sigma_i^\dagger b_j \mathrm{e}^{-\mathrm{i}\phi}\right) + O(\eta_{ij}^3). \tag{3.17}$$

This is identical to the well-known Jaynes-Cummings Hamiltonian from quantum optics [101, 102]. The red-sideband interaction coherently exchanges quanta between the qubit states and the phonon modes. For example, $\sigma_i b_j^\dagger$ lowers the internal state of the ith qubit through stimulated emission while simultaneously creating a phonon in the jth motional mode, while $\sigma_i^\dagger b_j$ performs the inverse process.

Blue sidebands: When $\omega = \omega_i + \nu_j$ the laser is resonant with the first-order blue motional sideband and (3.12) simplifies to

$$H_{\mathrm{BSB}} = -\mathrm{i}\frac{\hbar}{2}\sum_{ij}\Omega_i\eta_{ij}\left(\sigma_i b_j \mathrm{e}^{\mathrm{i}\phi} - \sigma_i^\dagger b_j^\dagger \mathrm{e}^{-\mathrm{i}\phi}\right) + O(\eta_{ij}^3). \tag{3.18}$$

The blue-sideband interaction also entangles the qubit with its motional state. The term $\sigma_i b_j$ simultaneously lowers the states of the ith qubit and the jth motional mode, while $\sigma_i^\dagger b_j^\dagger$ performs the inverse operation.

3.3.2 Single-qubit gates

How should the laser amplitude, phase, frequency, and orientation be modulated to produce a particular unitary gate? We may think of this as a quantum control problem. Consider a laser which illuminates a single ion, either by tightly focusing the beam or by moving

the ion to an interaction region with a local beam. If the laser is resonant with the carrier transition, the system evolves according to the Hamiltonian

$$H = \frac{\hbar\Omega_k}{2}(X_k \cos\phi + Y_k \sin\phi), \tag{3.19}$$

where $X_k = \sigma_k + \sigma_k^\dagger$ and $Y_k = \mathrm{i}(\sigma_k - \sigma_k^\dagger)$ are Pauli operators and the label k corresponds to the addressed qubit. We may write (3.19) in the bilinear form $H = \hbar u^\mu H_\mu$, with the controls $u^x = \Omega_k \cos\phi$, $u^y = \Omega_k \sin\phi$ and spin operators $H_\mu \in \{X_k/2, Y_k/2\}$. The spin operators generate the Lie algebra $\mathfrak{su}(2)$ by repeated application of the Lie bracket. Therefore any single-qubit operator $U \in SU(2)$ can be produced by adjusting the laser phase. Since adjusting the laser amplitude scales the controls equally, it is not possible to produce an arbitrary single-qubit gate by modulating the amplitude alone.

Suppose the laser could be steered to individually address each ion in the chain, or equivalently suppose each ion may be separated and delivered to an interaction region. Then on each ion, we may perform an arbitrary single-qubit gate. This corresponds to the Lie group $\bigotimes_i SU(2)$, where the index i runs over the ions in the chain.

We denote single qubit rotations as $R_k(\theta, \phi) = \exp(-\frac{\mathrm{i}\theta}{2}(X_k \cos\phi + Y_k \sin\phi))$, which modifies the qubit state by rotating the Bloch vector by an angle θ about an axis $X_k \cos\phi + Y_k \sin\phi$ in the X_k-Y_k plane. For constant-phase pulses, $\theta = \int_0^t dt'\, \Omega_k(t')$ is proportional to the pulse area. When there is no risk of confusion, we drop the qubit index k to simplify notation.

3.3.3 Motional entangling gates

Several gates use motional modes as an "information bus" to entangle ions trapped in a common well. Here we describe the Mølmer-Sørensen gate [103–105], which is commonly used in quantum computing experiments since the gate fidelity depends weakly on the ion temperature. The gate uses a laser pulse which returns the phonon modes to their original state at the end of the operation. The Mølmer-Sørensen gate behaves like an effective spin-spin coupling between qubits.

Consider a bichromatic laser beam with frequency components nearly resonant with

the blue and red sidebands of a motional mode. This laser could be prepared by passing a beam through an AOM driven by two RF frequencies and combining the first-order diffracted beams [105]. If we illuminate the ions with equal intensity and choose the frequency components so that they are symmetrically detuned about the carrier transition, e.g. $\omega_\pm = \omega_i \pm (\nu_j + \delta)$, then the system evolves according to the Hamiltonian,

$$H = \frac{\hbar\Omega_i\eta_{ij}}{2}\left(b_j e^{i\delta t} + b_j^\dagger e^{-i\delta t}\right) S_\phi. \tag{3.20}$$

Here $S_\phi = S_x \sin\phi - S_y \cos\phi$, where $S_x = \sum_i X_i$ and $S_y = \sum_i Y_i$ are total spin operators and we have simplified the analysis by neglecting off-resonant couplings to neighboring transitions and other motional modes.

Propagation under (3.20) generates a spin-dependent displacement in the oscillator phase space. Let $\gamma(t) = -ie^{-i\delta t}(\Omega_i\eta_{ij}/2)$ so that we may write the Schrödinger equation for the propagator as $\dot{U}(t) = (\gamma(t)b_j^\dagger - \gamma^*(t)b_j)S_\phi U(t)$. This is easily solved using a Magnus expansion (see section 2.2.3.2 for details). The solution is

$$U(t) = D(\alpha(t)S_\phi)\exp(i\Phi(t)S_\phi^2) \tag{3.21}$$

where $D(\alpha) = \exp(\alpha b_j^\dagger - \alpha^* b_j)$ is a displacement operator and

$$\alpha(t) = \int_0^t dt'\,\gamma(t'), \tag{3.22}$$

$$i\Phi(t) = \frac{1}{2}\int_0^t dt' \int_0^{t'} dt''\,\{\gamma(t')\gamma^*(t'') - \gamma^*(t')\gamma(t'')\}. \tag{3.23}$$

An exact solution is possible since all second-order commutators of the annihilation operators are proportional to the identity, for instance $[b_j, b_j^\dagger] = 1$. Therefore third-order and higher commutators are identically zero and the Magnus expansion truncates after two terms. Equivalently the Lie algebra for the annihilation operators $\mathfrak{h} = \text{span}\{b_j, b_j^\dagger\}$, called the Heisenberg algebra, is nilpotent.

The displacement operator entangles the qubits to the ion motion, however the Mølmer-Sørensen gate avoids this entanglement by choosing the laser pulse so that $D(\alpha(t)S_\phi) = 1$. In particular if we apply (3.20) for a duration $t_f = 2\pi N/\delta$, where $N \in \{1, 2, 3, \cdots\}$ then

$\alpha(t_f) = 0$ and the total operation is

$$U(t_f) = \exp\left(\mathrm{i}\frac{N\pi}{2}\left(\frac{\Omega_i \eta_{ij}}{\delta}\right)^2 S_\phi^2\right). \tag{3.24}$$

During the gate $\alpha(t)$ traces a circular path in the harmonic oscillator phase space. The direction $\alpha(t)$ orbits is conditioned by the spin operator S_ϕ. At t_f, the paths return to the origin and motional state returns to the original value, however the sign of the phase enclosed by the paths now depends on the total spin.

3.4 Summary

Here we have described ion trapping and ion-trap quantum computing in detail. Paul traps use an RF quadrupolar field to confine atomic ions; we employ microfabricated surface-electrode traps since they permit complex electrode geometries compatible with ion shuttling and rearrangement. The laser and pulse control systems required for quantum gates on $^{40}Ca^+$ and $^{171}Yb^+$ qubits were discussed. Also, we considered the interaction of laser pulses with trapped atomic-ion qubits in the Lamb-Dicke regime, and showed how arbitrary single qubit rotations could be achieved using focused laser pulses. The Mølmer-Sørensen interaction generates an effective spin-spin coupling between ions. Later, we show that universal quantum computation is possible using only pairwise spin-spin couplings and single qubit rotations. In other words, the effective control Hamiltonians for these interactions generate the n-qubit Lie algebra $\mathfrak{su}(2^n)$ by repeated Lie brackets.

CHAPTER IV

THEORY OF COMPENSATING PULSE SEQUENCES

Ion-trap quantum computers require precision control of laser pulses during quantum gates. In practice, our experiments are susceptible to systematic control errors, for instance errors caused by a slow drift in the laser frequency or alignment. In this chapter we introduce compensating composite pulse sequences, which relax these precision requirements by reducing unknown but systematic errors. Section 4.1 describes a general model for systematic control errors. In section 4.2 we identify a Lie-algebraic property which all compensating sequences must satisfy. Section 4.3 considers common systematic errors in ion-trap computers.

4.1 Systematic control errors

Quantum computers use a set of controllable interactions to generate arbitrary unitary gates. In section 2.2 we treated this problem with quantum control theory. Here we consider a control problem where the objective is to produce a target gate U_T by modulating a set of unitless control Hamiltonians $\{H_1, H_2, \cdots, H_n\}$ via a set of controls $\vec{u}(t) = (u^1(t), u^2(t), \cdots, u^n(t))$. An acceptable set of controls satisfies $U(\vec{u}; t_f) = U_T$, where $U(\vec{u}; t_f)$ is the propagator produced by applying the controls $\vec{u}(t)$ over the interval $t \in [0, t_f)$. There are many (infinite in most cases) controls which implement a target unitary transformation [56]. Some controls may be robust under distortion by systematic errors.

Systematic errors arise from imperfect control. These errors are deterministic but unknown to the experimenter. Suppose during an experiment an unknown systematic error deforms the applied controls from $\vec{u}(t)$ to $\vec{w}(t)$. In these cases, it is appropriate to introduce a deterministic model for the control deformation [106, 107].

Definition 5. *A systematic* error model *is a set of maps* $\{F^\mu\}$ *of the form* $F^\mu : (\mathscr{U}^n, \mathbb{R}) \to \mathscr{U}$ *which transform an error-free control vector* $\vec{u} \in \mathscr{U}^n$ *and an* error parameter $\epsilon \in \mathbb{R}$ *into an imperfect control* $w^\mu = F^\mu[\vec{u}; \epsilon]$.

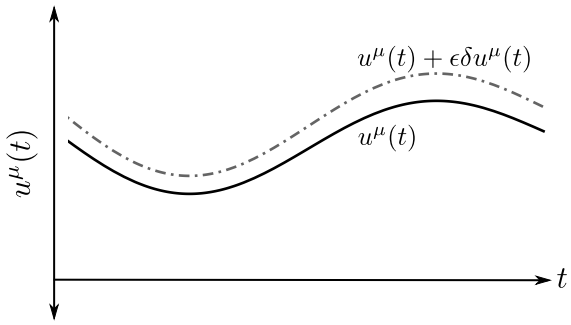

Figure 4.1: Systematic errors induce deformations of the ideal control functions $u^\mu(t)$ (solid curves) to the imperfect controls $w^\mu(t) = u^\mu(t) + \epsilon\delta u^\mu(t)$ (dashed curves).

The error model $\{F^\mu\}$ completely specifies the nature of the control deformation and the functionals F^μ are chosen to model a physical error process [107]. The error parameter ϵ is an unknown real number that parametrizes the magnitude of the error, so that when $\epsilon = 0$ no error occurs. This construction may be generalized to the case of multiple systematic errors by considering error models of the form $F^\mu[\vec{u}; \epsilon_i, \epsilon_j, \ldots, \epsilon_k]$.

Formally, we may perform the expansion

$$F^\mu[\vec{u};\epsilon] = F^\mu[\vec{u};0] + \epsilon \left.\frac{d}{d\epsilon} F^\mu[\vec{u};\epsilon]\right|_{\epsilon=0} + O(\epsilon^2), \tag{4.1}$$

then by the condition that when $\epsilon = 0$ the control must be error free, it is trivial to identify $u^\mu(t) = F^\mu[\vec{u}(t); 0]$. Frequently, it is sufficient to consider models which are linear in the parameter ϵ. In this case we introduce the shorthand notation $\delta u^\mu(t) = \left.\frac{d}{d\epsilon} F^\mu[\vec{u}(t);\epsilon]\right|_{\epsilon=0}$ and the corresponding vector $\vec{\delta u}(t)$ to represent the first-order deformation of the controls, so that the imperfect controls take the form $\vec{w}(t) = \vec{u}(t) + \epsilon\vec{\delta u}(t)$.

A natural question to ask is what effect systematic errors have on the evolution of the system. In the presence of unknown errors, the error-free propagators $U(\vec{u}; t_f)$ are replaced with their imperfect counterparts $U(\vec{w}; t_f) = U(\vec{u} + \epsilon\vec{\delta u}; t_f)$, which may be regarded as an image of the perfect propagator under the deformation of the controls [107]. If an error-free propagator produces a particular gate, then in general the imperfect propagator only approximates this operation. In our discussion it will be necessary to calculate the accuracy

of approximate gates. We use the *fidelity* defined by

$$\mathcal{F}(U,V) = \min_{\psi} \sqrt{\langle\psi|U^\dagger V|\psi\rangle\langle\psi|V^\dagger U|\psi\rangle}, \tag{4.2}$$

where $U, V \in U(n)$ are unitary operators. The minimization occurs over normalized states in the associated Hilbert space $\mathscr{H}(n)$. The fidelity returns a real number in the range $0 \leq \mathcal{F}(U,V) \leq 1$, with $\mathcal{F}(U,V) = 1$ if and only if $V = \mathrm{e}^{\mathrm{i}\phi}U$ where ϕ is a global phase. This contrasts with other measures, such as the distance $\mathcal{D}(U,V) = ||U - V||_{HS}$, which discriminate between global phases [35, 108]. The fidelity is the most common measure used to evaluate gate accuracy in the quantum information community. Our interest lies in producing extremely accurate gates. Sometimes we use the *infidelity* defined as $1 - \mathcal{F}(U,V)$ as a measure of the strength of the residual error.

4.2 Compensating pulse sequences

It is obvious that imperfect pulses make accurate manipulation of a quantum state difficult. One may be surprised to find that for some cases, the effects of errors on the controls may be systematically removed, without knowledge of the amplitude ϵ. The method we describe involves implementing a compensating composite pulse sequence which is robust against distortion of the controls by a particular error model. In this context, we propose the following definition of a robust control.

Definition 6. *An nth-order* robust control *for an error model* $\{F^\mu\}$ *is a set of controls* $\vec{u}_*$ *such that* $U(\vec{u}_* + \epsilon\vec{\delta u}_*; t_f) = U(\vec{u}_*; t_f) + O(\epsilon^{n+1})$.

As an example, consider a case where an experimentalist would like to approximate the target unitary U_T, where at least one of the controls is influenced by a systematic error. Suppose there exists an nth-order robust control such that $U(\vec{u}_* + \epsilon\vec{\delta u}_*; t_f) = U_T + O(\epsilon^{n+1})$. The experimenter attempts to apply the ideal control $\vec{u}_*$, however due to the systematic error $\vec{u}_* + \epsilon\vec{\delta u}_*$ is applied instead. Despite the error, the resulting propagator still approximates the target operation up to $O(\epsilon^{n+1})$, with the infidelity scaling as $O(\epsilon^{2n+2})$. The accuracy of the approximation improves as the order n increases. No knowledge of ϵ is required on the part of the experimenter.

Definition 7. *An nth-order* fully compensating pulse sequence *is a propagator* $U(\vec{u}_*; t_f)$ *derived from an nth-order robust control* $\vec{u}_*$.

Compensating sequences have a long history in NMR spectroscopy [41, 109–112], where they are frequently used to correct systematic errors in the control of nuclear spins. Most compensating sequences implement state-to-state control and are unsuitable for quantum computation. Sequences which implement unitary-control, meaning they produce a particular unitary gate rather than simply mapping two particular states to each other, are called *fully compensating*. Only fully compensating sequences are appropriate for quantum computation [113].

4.2.1 A fundamental property of fully-compensating sequences

Our approach is to transform the propagator into an interaction frame that moves with the ideal trajectory. Let us define the interaction frame Hamiltonian $\tilde{H}(t) = \epsilon \delta u^\mu(t) \tilde{H}_\mu(t)$, where $\tilde{H}_\mu(t) = U^\dagger(\vec{u}; t) H_\mu U(\vec{u}; t)$ is the image of the control Hamiltonian under the frame transformation; in some literature this is referred to as the *toggling frame* [114]. We regard $\tilde{H}(t)$ as a perturbation, and we associate the propagator $\tilde{U}(\epsilon\vec{\delta u}; t_f)$ as the particular solution to the interaction-frame Schrödinger equation over the interval $t \in [0, t_f)$. Then returning to the original (qubit) frame, we have

$$U(\vec{u} + \epsilon\vec{\delta u}; t_f) = U(\vec{u}; t_f)\, \tilde{U}(\epsilon\vec{\delta u}; t_f). \tag{4.3}$$

It follows that $U(\vec{u}_*; t_f)$ is an nth order fully compensating pulse sequence if and only if $\tilde{U}(\epsilon\vec{\delta u}_*; t_f) = 1 + O(\epsilon^{n+1})$. Quite generally, when a fully compensating pulse sequence is transformed into the toggling frame the resulting propagator must approximate the identity operation [106].

Our approach uses a Lie-algebraic picture to infer certain geometric properties of robust controls when viewed in the toggling frame. Recall from section 2.2.2 that the skew-symmetrized control Hamiltonians $\{\mathbf{e}_\mu = -\mathrm{i}H_\mu\}$ and other Hamiltonians generated by repeated Lie brackets form a basis for the dynamic Lie algebra $\mathfrak{g}$. When we move to the toggling frame the basis vectors are transformed as $\tilde{\mathbf{e}}_\mu(t) = U^\dagger(\vec{u}; t)\mathbf{e}_\mu U(\vec{u}; t)$. The vectors $\{\tilde{\mathbf{e}}_\mu\}$ form a comoving coordinate system for $\mathfrak{g}$ that moves with the ideal trajectory

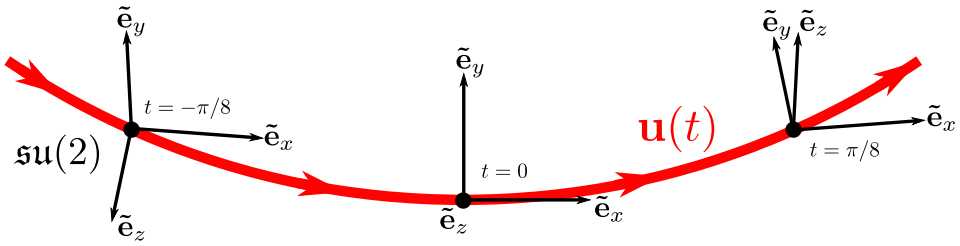

Figure 4.2: Movement of the toggling frame as seen from the qubit frame. The toggling frame is comoving with $\mathbf{u}(t)$ but the basis vectors are rotated according to $\tilde{\mathbf{e}}_\mu(t) = U^\dagger(\vec{u};t)\mathbf{e}_\mu U(\vec{u};t)$. In this illustration $\mathbf{u}(t) = 2\sin(t)\mathbf{e}_x + 2\cos(t)\mathbf{e}_y$ and $\{\mathbf{e}_\mu\}$ are the basis vectors for $\mathfrak{su}(2)$ described in section 2.2.2.2.

$\mathbf{u}(t) = u^\mu(t)\mathbf{e}_\mu$, see figure 4.2.

In the toggling frame any propagation is due to the systematic error alone. We identify the vector path $\tilde{\boldsymbol{\delta}\mathbf{u}}(t) = \delta u^\mu(t)\tilde{\mathbf{e}}_\mu(t)$ as the path associated with the systematic error viewed in the interaction frame. Provided that the displacements $\epsilon\tilde{\boldsymbol{\delta}\mathbf{u}}(t)$ are sufficiently small relative to the ideal controls, we may perform a Magnus expansion for the interaction frame propagator,

$$\tilde{U}(\epsilon\vec{\delta u};t_f) = \exp\left(\sum_{n=1}^{\infty}\epsilon^n\tilde{\mathbf{\Omega}}_n(\vec{\delta u};t_f)\right) \tag{4.4}$$

where the integration of the expansion terms is performed in the appropriate frame. Suppose $\vec{u}_*$ is an nth order robust control, which requires $\tilde{U}(\epsilon\vec{\delta u}_*;t_f) = 1 + O(\epsilon^{n+1})$. It immediately follows from (4.4) that this condition is satisfied for any ϵ if and only if the leading n-many Magnus expansion terms $\{\tilde{\mathbf{\Omega}}_1, \tilde{\mathbf{\Omega}}_2, \ldots, \tilde{\mathbf{\Omega}}_n\}$ simultaneously equal zero at t_f.

This condition may also be understood in terms of geometric properties of vector paths on the Lie algebra. For instance $\tilde{\mathbf{\Omega}}_1(\vec{\delta u}_*;t_f) = 0$ requires that

$$0 = \int_0^{t_f} dt\, \tilde{\boldsymbol{\delta}\mathbf{u}}_*(t), \tag{4.5}$$

or equivalently, that the vector path $\tilde{\boldsymbol{\delta}\mathbf{u}}_*$ forms a closed geometric figure on the interaction frame Lie algebra [115]. The elimination of higher-order expansion terms will place additional geometric constraints on the path which will depend on the structure of the Lie algebra (i.e. the commutators between paths on the algebra) [107]. For instance in $\mathfrak{su}(2)$ the commutator is isomorphic to the vector cross product in $\mathbb{R}^3$, so in this algebra we

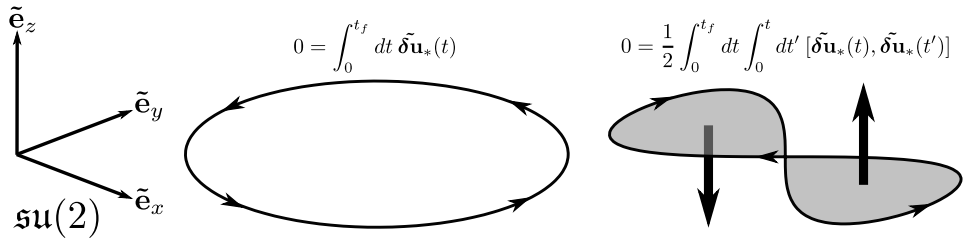

Figure 4.3: Control geometry viewed in the toggling frame. The distortion $\tilde{\boldsymbol{\delta}}\mathbf{u}_*$ forms a vector path on the Lie algebra, here $\mathfrak{su}(2)$. To cancel $\tilde{\boldsymbol{\Omega}}_1$ the distorted control must form a closed loop (left and right paths). One method to cancel $\tilde{\boldsymbol{\Omega}}_2$ balances the signed areas enclosed by the path (right path).

interpret the second-order term as a signed area enclosed by the path. One construction which cancels $\tilde{\boldsymbol{\Omega}}_2$ chooses a path that encloses regions of equal and opposite sign. Figure 4.3 illustrates paths which cancel $\tilde{\boldsymbol{\Omega}}_1$ and $\tilde{\boldsymbol{\Omega}}_2$ respectively.

This Lie theoretic method is a useful tool in determining whether a propagator generated from a control is a compensating sequence; we may directly calculate the interaction frame Magnus expansion terms in a given error model and show that they equal zero. The inverse problem (i.e., solving for control functions) is typically much more difficult. In general, the interaction frame basis vectors $\{\tilde{\mathbf{e}}_\mu\}$ are highly nonlinear functions of the ideal controls, which impedes several analytical solution methods.

4.3 Systematic errors in ion-trap quantum computing experiments

In practice, systematic errors in the controls caused by instrumental limitations prohibit the application of perfect quantum gates. We consider several models for errors in the controls of an ion-trap quantum computer. Section 4.3.1 describes control errors in single-qubit gates. Section 4.3.2 describes control errors in multi-qubit gates, such as the Mølmer-Sørensen gate. Often compensating pulse sequences are optimized for one type of error, but provide no advantage against a different type of systematic error.

4.3.1 Error models for single-qubit gates

4.3.1.1 Addressing errors

Most single-qubit gates involve applying a tightly focused laser pulse resonant with the qubit carrier transition in the Lamb-Dicke limit. In the ideal case, the laser illuminates only a single ion and the Hamiltonian is given by $H_k = \frac{\hbar\Omega_k}{2}(X_k \cos\phi + Y_k \sin\phi)$, where the index k labels the addressed ion (see section 3.3.2). Frequently however neighboring qubits are partially illuminated, which leads to an unknown but systematic error on the unaddressed qubits. These *addressing errors* arise from poor beam focusing and laser pointing instabilities [107, 116]. In this case, the Hamiltonian for the entire qubit chain is $H_k + \sum_{j\neq k} H_j$, and for the case of constant-phase pulses the entire unitary propagator may be written in terms of tensor products of single-qubit rotations as

$$R_k(\theta,\phi)\left[\prod_{j\neq k} R_j(\epsilon_j\theta,\phi)\right], \tag{4.6}$$

where $\theta = \int_0^{t_f} dt\ \Omega_k(t)$ is the angle of the rotation applied to the addressed qubit and $\epsilon_j = \Omega_j/\Omega_k \ll 1$ is the fractional Rabi frequency (proportional to laser amplitude) at the jth unaddressed qubit. In this control problem the objective is to apply some non-trivial rotation to the addressed qubit, while simultaneously suppressing unwanted rotations on the unaddressed qubits. Sequences which perform this task are called *narrowband* [117, 118].

We also may write the Hamiltonian in bilinear form in terms of the control functions $\{u^x = \Omega_k \cos\phi, u^y = \Omega_k \sin\phi\}$ and Hamiltonians $H_{\mu,k} \in \{X_k/2, Y_k/2\}$ and $H_{\mu,j} \in \{X_j/2, Y_j/2\}$ as

$$H = u^\mu H_{\mu,k} + \sum_{j\neq k} \epsilon_j \left(u^\mu H_{\mu,j}\right). \tag{4.7}$$

We group all of the controls into a vector $\vec{u} = (u^x_k, u^y_k, \cdots, u^x_j, u^y_j, \cdots)$ and require that in the ideal case the controls for the unaddressed qubits are identically zero. From here it is simple to identify an error model for the controls, summarized below

$$F^\mu_k[\vec{u};\epsilon_j] = u^\mu \qquad \text{for addressed qubits,}$$

$$F^\mu_j[\vec{u};\epsilon_j] = 0 + \epsilon_j u^\mu \qquad \text{for unaddressed qubits.}$$

From a mathematical point of view, addressing errors are simple to consider. Since rotations on independent qubits commute, we may separate the dynamics and treat the evolution of each qubit individually. On the addressed qubit the controls are applied perfectly. On the unaddressed qubits the ideal controls are exactly zero (no operation takes place). This implies $\tilde{H}_{\mu,j}(t) = H_{\mu,j}$, and that the toggling and qubit frames are identical. We may design a compensating sequence which corrects the systematic control distortion without the added complication of the passage into the interaction frame.

4.3.1.2 Amplitude errors

A second source of systematic error arises from slow variations in the laser amplitude, resulting in a small offset in the applied Rabi frequency. Frequently an experimenter adjusts the laser pulses to match a calibrated Rabi frequency, here denoted by Ω'. If the actual Rabi frequency Ω differs from the calibrated value then the qubit experiences a systematic error. In this case, the Hamiltonian may be written as

$$H = (1 + \epsilon)u^{\mu}H_{\mu}, \tag{4.8}$$

where $\{u^x = \Omega' \cos\phi, u^y = \Omega' \sin\phi\}$, the control Hamiltonians are similar as before, and $\epsilon = (\Omega/\Omega') - 1$ is an error parameter representing the magnitude of the systematic error. The interaction produces the propagator $R(\theta(1 + \epsilon), \phi)$, where $\theta = \Omega' t_f$ is the intended angle of rotation for the gate. Amplitude errors therefore result in systematic over or under-rotations on the qubit. The objective in this control problem is to perform a non-trivial rotation while suppressing systematic amplitude errors. Sequences which perform this task are called *broadband* [117, 119]. Amplitude errors are represented by the error model,

$$F^{\mu}[\vec{u}; \epsilon] = u^{\mu} + \epsilon u^{\mu}, \text{ where } \mu \in \{x, y\}.$$

4.3.1.3 Detuning errors

Systematic errors may also arise in the control of the laser frequency. Usually single-qubit operations use resonant laser pulses, which result in propagators that act as rotations in the X-Y plane. If however the laser drifts off resonance then the Hamiltonian picks up a

Z component and the qubit no longer rotates about the intended axis. We parametrize the Hamiltonian as

$$H = u^x H_x + u^y H_y + \epsilon\Omega H_z, \tag{4.9}$$

where $\{u^x = \Omega\cos\phi, u^y = \Omega\sin\phi\}$, Ω is the Rabi frequency, and $\epsilon = (\omega - \omega_i)/\Omega$ is an error parameter related to the ratio of the laser detuning to the Rabi frequency. For the case of constant controls the Hamiltonian produces the propagator

$$U = \exp\left[-\frac{\mathrm{i}\theta}{2}(X\cos\phi + Y\sin\phi + \epsilon Z)\right], \tag{4.10}$$

where $\theta = \Omega t_f$. This resembles the ideal rotation $R(\theta, \phi)$, now with an extra Z component that lifts the rotation axis out of the X-Y plane. The objective in this control problem is to produce accurate gates despite an unknown laser frequency offset [110, 120, 121]. Detuning errors are represented by the error model,

$$F^\mu[\vec{u}; \epsilon] = u^\mu \qquad \text{for } \mu \in \{x, y\},$$
$$F^z[\vec{u}; \epsilon] = 0 + \epsilon\Omega.$$

4.3.2 Error models for two-qubit gates

4.3.2.1 Spin-spin coupling (Ising) errors

Most multi-qubit gates generate an effective interaction that resembles a spin-spin coupling. Some systematic errors introduce control distortions that resemble an offset in the effective spin-spin coupling strength. The Mølmer-Sørensen gate produces the unitary propagator $U = \exp(-\mathrm{i}\Phi S_\phi^2)$ where

$$\Phi = \frac{N\pi}{2}\left(\frac{\Omega\eta}{\delta}\right)^2, \tag{4.11}$$

Ω is the Rabi frequency, η is the Lamb-Dicke parameter, and δ is the magnitude of the detuning from the first-order sidebands, see section 3.3.3 for details.

For Mølmer-Sørensen gates there are two types of effective spin-spin coupling errors. The first involves a systematic uncertainty in the Rabi frequency, similar to single-qubit amplitude errors. Denote by Ω' the calibrated Rabi frequency. Then the effective Hamiltonian may be written as $H = \frac{\Phi}{t_f}(1+\epsilon)^2 S_\phi^2$, where $\epsilon = (\Omega/\Omega') - 1$ is the same amplitude error

parameter previously considered. Amplitude errors effect both single-qubit and multi-qubit gates.

The second error involves miscalibration of the Lamb-Dicke parameter, perhaps arising from an improperly aligned laser relative to the trap normal modes. Let η' be the ideal calibrated Lamb-Dicke parameter. Similar to the case of addressing errors, the effective Hamiltonian may be written as $H = \frac{\Phi}{t_f}(1+\epsilon)^2 S_\phi^2$, where $\epsilon = (\eta/\eta') - 1$ is an error parameter related to the offset in the Lamb-Dicke parameter. However since this error does not depend on the Rabi frequency, single-qubit gates are unaffected.

4.3.2.2 Addressing errors

Similar to single-qubit gates, the Mølmer-Sørensen gate also requires focused laser beams that selectively illuminate a collection of addressed ions, here denoted as $\mathscr{A}$. The laser amplitudes are balanced such that every qubit in the addressed set evolves at the same Rabi frequency Ω. Frequently however neighboring ions are partially illuminated, which leads to an unknown but systematic error related to an unwanted entanglement between the addressed qubits and unaddressed qubits. In this case the effective Hamiltonian is

$$H = \frac{\Phi}{t_f}\left[\sum_{k\in\mathscr{A}}(X_k \sin\phi - Y_k\cos\phi) + \sum_{j\notin\mathscr{A}}\epsilon_j(X_j\sin\phi - Y_j\cos\phi)\right]^2, \tag{4.12}$$

where $\epsilon_j = \Omega_j/\Omega \ll 1$ is the fractional Rabi frequency at the jth unaddressed qubit. Terms which generate unwanted entanglement (e.g., $\epsilon_j X_k X_j$) scale linearly with the systematic error. The unaddressed qubits also see a small unwanted phase of $\epsilon_j^2\Phi$. We may write a formal error model using the usual method of expanding the Hamiltonian and grouping terms by basis elements of the Lie algebra.

4.4 Summary

This chapter discussed compensating composite pulse sequences and error models for ion-trap quantum computers. Compensating sequences are propagators which are robust to distortion introduced by systematic control errors. Viewed in the toggling frame, we identified a general Lie-algebraic property nth-order compensating sequences: the leading n-many Magnus expansion terms simultaneously cancel. Each Magnus term may be interpreted

geometrically. In the following chapter we derive narrowband sequences from geometric considerations on the Lie algebra.

CHAPTER V

ION ADDRESSING USING COMPENSATING SEQUENCES

In ion-trap quantum computers local addressing of individual qubits is achieved via focused laser pulses. Single-qubit addressing therefore demands accurate beam steering to avoid crosstalk between neighboring qubits, a significant engineering challenge in large scalable systems [122]. These precision requirements may be reduced by replacing simple single-qubit gates with a narrowband composite pulse sequence [116, 118]. Narrowband sequences allow manipulation of a single ion, even if neighboring ions are subjected to significant laser intensity.

In this chapter we describe narrowband pulse sequences for individual ion addressing. Section 5.1 discusses the SK1 and N2 sequences. In section 5.1.2 we describe a novel family of augmented sequences, which improve on SK1 and N2 by generalizing their form. Section 5.2 describes related experiments on $^{40}Ca^{+}$ qubits, where qubit addressing is enhanced by using narrowband sequences. To our knowledge, this is the first reported experimental demonstration of this technique in ion traps.

5.1 Narrowband sequences

The system we consider is a chain of ions with a single addressed ion illuminated by a focused laser. Neighboring qubits are partially illuminated by the beam, resulting in an addressing error. Since the dynamics on each ion are correlated but separable (i.e., no entanglement is generated) we may consider the evolution of each qubit individually. Here we use sequences of resonant constant-phase pulses, where each pulse produces a spin rotation $R_k(\theta, \phi)$ on addressed qubit and simultaneous rotations $R_j(\epsilon_j\theta, \phi)$ on unaddressed qubits.

Alternatively a pulse propagator may be represented in terms of a vector on the Lie algebra. We use the same parameterization used in section 4.3.1.1 for the controls and control Hamiltonians. The basis vectors $\mathbf{e}_{\mu,k}$ and $\mathbf{e}_{\mu,j}$ are proportional to Pauli operators for the addressed qubit and the unaddressed qubits respectively. The propagators may be

written as $R_k(\theta,\phi) = \mathrm{e}^{\mathbf{r}_k}$ and $R_j(\epsilon_j\theta,\phi) = \mathrm{e}^{\epsilon_j \mathbf{r}_j}$ where

$$\mathbf{r}_k = \int_0^{t_f} dt\, u^\mu(t)\mathbf{e}_{\mu,k}, \qquad \mathbf{r}_j = \int_0^{t_f} dt\, u^\mu(t)\mathbf{e}_{\mu,j}, \tag{5.1}$$

are vectors on the distinct $\mathfrak{su}(2)$ subalgebras corresponding to the addressed and unaddressed qubits. Viewed in the Lie algebra, all qubits undergo similar transformations, only the vectors corresponding to the unaddressed qubits are scaled by a factor ϵ_j. Provided that $\epsilon_j \ll 1$ we may accurately compute products of simple pulses using a Magnus expansion or a BCH formula. For instance a sequence of n pulses produces the propagator $U_k = \prod_{\ell=1}^n \exp(\mathbf{r}_{k,\ell})$ for addressed qubits and

$$U_j = \exp\left(\epsilon_j \sum_{\ell=1}^{n} \mathbf{r}_{j,\ell} + \frac{\epsilon_j^2}{2}\sum_{\ell=1}^{n}\sum_{m=1}^{\ell}[\mathbf{r}_{j,\ell},\mathbf{r}_{j,m}]\right) + O(\epsilon_j^3), \tag{5.2}$$

for unaddressed qubits. Since ideally U_j should equal the identity, we should construct a sequence of rotations such that the error terms in (5.2) vanish. This task is considerably simplified by visualising the vectors $\{\mathbf{r}_{j,\ell}\}$ as segments of a vector path on $\mathfrak{su}(2)$.

5.1.1 Simple narrowband sequences

5.1.1.1 SK1

The simplest non-trivial narrowband sequence, called SK1 [107, 114, 123], uses three simple rotations generated by the vectors

$$\begin{aligned}
\mathbf{r}_{k,1} &= \vartheta \mathbf{e}_{x,k},\\
\mathbf{r}_{k,2} &= (2\pi\cos\phi_{SK1})\mathbf{e}_{x,k} + (2\pi\sin\phi_{SK1})\mathbf{e}_{y,k},\\
\mathbf{r}_{k,3} &= (2\pi\cos\phi_{SK1})\mathbf{e}_{x,k} - (2\pi\sin\phi_{SK1})\mathbf{e}_{y,k},
\end{aligned}$$

with similar constructions for the vectors $\{\mathbf{r}_{j,\ell}\}$. The phase $\cos\phi_{SK1} = -\frac{\vartheta}{4\pi}$ is selected so that $\sum_\ell \mathbf{r}_{j,\ell} = 0$ and therefore the controls are first-order robust to addressing errors. Written in terms of simple rotations, the sequence is $U_{k,SK1} = R_k(2\pi,-\phi_{SK1})R_k(2\pi,\phi_{SK1})R_k(\vartheta,0) = R_k(\vartheta,0)$ for addressed qubits and $U_{j,SK1} = 1 + O(\epsilon_j^2)$ for the unaddressed qubits. The addressing error is suppressed by replacing a simple rotation $R_k(\vartheta,0)$ with a corresponding SK1 sequence. The trajectory of an unaddressed qubit (e.g., in the limit $\epsilon_j \to 0$) is related

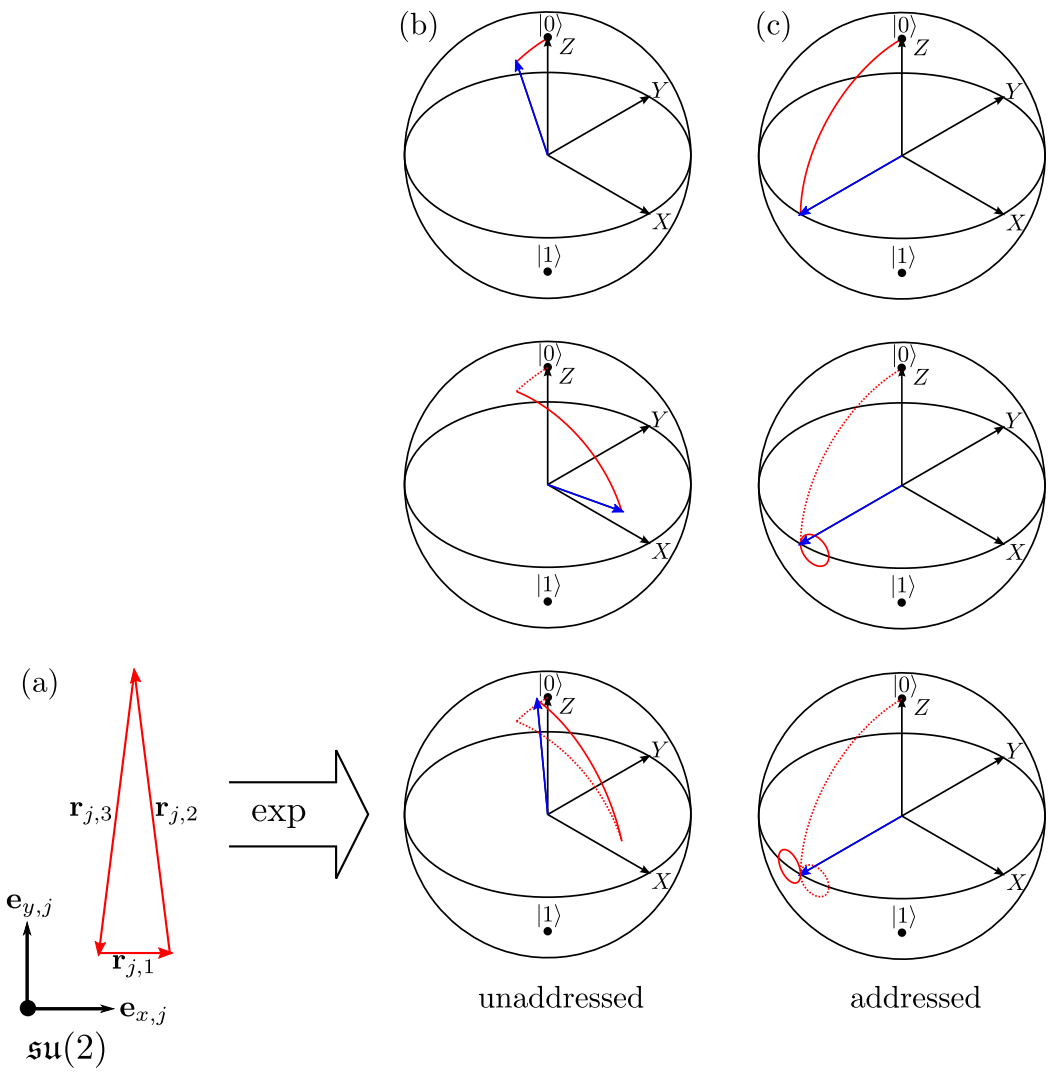

Figure 5.1: Trajectories of unaddressed and addressed qubits during an SK1 sequence that produces the gate $R_k(\pi/2, 0)$. Here $\epsilon_j = 0.2$, corresponding to a 20% addressing error. (a) Closed path formed by the vectors $\{\mathbf{r}_{j,\ell}\}$ on the unaddressed qubit Lie algebra. (b) Trajectory followed by an unaddressed qubit. (c) Trajectory followed by an addressed qubit.

to the vectors $\mathbf{r}_{j,\ell}$ by the exponential map. Figure 5.1 illustrates the trajectories of an addressed and an unaddressed qubit under a SK1 sequence.

The sequence may produce other net rotations, for instance $R_k(\vartheta, \varphi)$, by uniformly adding a phase φ to each pulse in the sequence. Alternatively one may prepare an SK1 sequence for any unitary $U_T \in SU(2)$ using a similarity transformation. For instance, we may solve for an operation Υ that performs the planar rotation $\Upsilon_k U_T \Upsilon_k^\dagger = R_k(\vartheta, 0)$, where $\vartheta = 2^{1/2}||\arg U_T||_{HS}$ is the net rotation angle for the desired gate. The sequence $\Upsilon_k^\dagger(U_{k,SK1})\Upsilon_k = U_T$ performs the desired gate on the addressed qubits, while simultaneously on the unaddressed qubits $\Upsilon_j^\dagger(U_{j,SK1})\Upsilon_j = 1 + O(\epsilon^2)$. We use this construction in section 5.1.2 when we describe augmented sequences with improved error suppression and lower time costs.

5.1.1.2 N2

A second narrowband sequence, which we call N2 [107, 117], uses four simple rotations generated by the vectors

$$\begin{aligned}
\mathbf{r}_{k,1} &= \vartheta \mathbf{e}_{x,k}, \\
\mathbf{r}_{k,2} &= (\pi \cos\phi_{N2})\mathbf{e}_{x,k} + (\pi \sin\phi_{N2})\mathbf{e}_{y,k}, \\
\mathbf{r}_{k,3} &= (2\pi \cos\phi_{N2})\mathbf{e}_{x,k} - (2\pi \sin\phi_{N2})\mathbf{e}_{y,k}, \\
\mathbf{r}_{k,4} &= (\pi \cos\phi_{N2})\mathbf{e}_{x,k} + (\pi \sin\phi_{N2})\mathbf{e}_{y,k},
\end{aligned}$$

with similar vectors $\{\mathbf{r}_{j,\ell}\}$ on the unaddressed ions. Again the phase $\cos\phi_{N2} = -\frac{\vartheta}{4\pi}$ is selected so that $\sum_\ell \mathbf{r}_{j,\ell} = 0$. In this arrangement the second and fourth vectors are identical; with some commutator algebra we may prove this symmetry along with $\sum_\ell \mathbf{r}_{j,\ell} = 0$ eliminates the second-order error term in (5.2). Geometrically, these conditions are equivalent to requiring that the path formed by the vectors encloses signed areas of equal magnitude but opposite sign (see figure 5.2). Therefore the controls are second-order robust to addressing errors. Written as a sequence of simple rotations, the sequence $U_{k,N2} = R_k(\pi, \phi_{N2})R_k(2\pi, -\phi_{N2})R_k(\pi, \phi_{N2})R_k(\vartheta, 0) = R_k(\vartheta, 0)$ for addressed qubits and $U_{j,N2} = 1 + O(\epsilon_j^3)$ for unaddressed qubits.

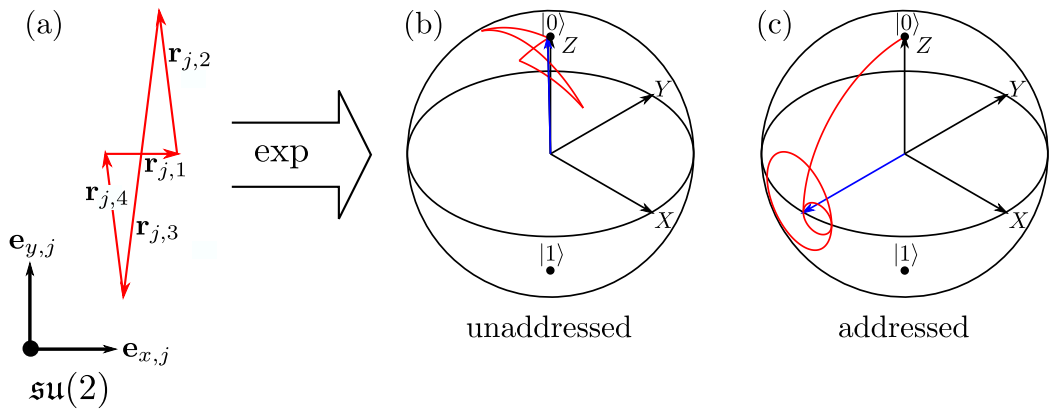

Figure 5.2: Trajectories of unaddressed and addressed qubits during an N2 sequence that produces the gate $R_k(\pi/2, 0)$. Here $\epsilon_j = 0.2$, corresponding to a 20% addressing error. (a) Closed path formed by the vectors $\{\mathbf{r}_{j,\ell}\}$ on the unaddressed qubit Lie algebra. (b) Trajectory followed by an unaddressed qubit. (c) Trajectory followed by an addressed qubit.

The N2 sequence was first discovered and applied by Wimperis [117], who called it NB1. Brown, Harrow, and Chuang [114, 123] later generalized this form to Nn, which compensates addressing errors to $O(\epsilon^n)$. We use Brown's naming convention to avoid confusion with other established sequences, namely NB2, NB3, etc. [117].

5.1.2 Augmented sequences

Compensating sequences reduce systematic control errors at the cost of increased time required to produce gates [107]. The natural question arises whether this time cost may be reduced. Here we present a new method that produces fully-compensating narrowband sequences with superior error correction properties and lower operation times.

Our method uses a Lie-algebraic construction to generalize existing sequences. We first write pulses of an existing sequence in terms of a set of vectors $\{\mathbf{r}_{j,\ell}\}$. The vector path perimeter $\sum_\ell ||\mathbf{r}_{j,\ell}||_{HS} = \sum_\ell \theta_\ell/\sqrt{2}$ is proportional to the total pulse area, i.e., the sum of rotation angles of each pulse. In most applications where the Rabi frequency is fixed to some maximum amplitude, the total pulse area is proportional to the duration of the sequence. We then allow the vector lengths (rotation angles) to vary in such a way that the error-canceling properties are preserved. Viewed on the Lie algebra, this is equivalent to requiring paths which preserve certain topological symmetries. We then use numerical

optimization to find sequences with favorable properties. We call sequences produced from this method augmented sequences.

5.1.2.1 ASK1

The augmented-SK1 sequence, which we call ASK1, uses three simple rotations generated by the vectors

$$\begin{aligned}
\mathbf{r}_{k,1} &= \theta_1 \mathbf{e}_{x,k}, \\
\mathbf{r}_{k,2} &= (\theta_2 \cos\phi_{ASK1})\mathbf{e}_{x,k} + (\theta_2 \sin\phi_{ASK1})\mathbf{e}_{y,k}, \\
\mathbf{r}_{k,3} &= (\theta_2 \cos\phi_{ASK1})\mathbf{e}_{x,k} - (\theta_2 \sin\phi_{ASK1})\mathbf{e}_{y,k},
\end{aligned}$$

with similar vectors $\{\mathbf{r}_{j,\ell}\}$ corresponding to the unaddressed qubits. We choose the phase such that $\cos\phi_{ASK1} = -\frac{\theta_1}{2\theta_2}$ and therefore $\sum_\ell \mathbf{r}_{j,\ell} = 0$ provided that the triangle inequality $\theta_1 < 2\theta_2$ is satisfied. When we apply an ASK1 sequence the addressed qubit transforms under $U_{k,ASK1} = R_k(\theta_2, -\phi_{ASK1})R_k(\theta_2, \phi_{ASK1})R_k(\theta_1, 0)$ while unaddressed qubits transform under $U_{k,ASK1} = 1 + O(\epsilon_j^2)$. The ASK1 sequence produces an identity operation on unaddressed qubits with a fidelity $\mathcal{F} = 1 - \epsilon_j^4[(2\theta_1\theta_2)^2 - \theta_1^4]/128 + O(\epsilon_j^6)$. ASK1 is a generalization of the original sequence, in the sense that replacing $\theta_2 \to 2\pi$ recovers SK1. The special case where $\theta_1 = \theta_2 = \pi$ corresponds to Jones' recently described NOT pulses [124].

5.1.2.2 AN2

The augmented-N2 sequence, which we call AN2, uses a similar parameterization for the vectors

$$\begin{aligned}
\mathbf{r}_{k,1} &= \theta_1 \mathbf{e}_{x,k}, \\
\mathbf{r}_{k,2} &= (\theta_2 \cos\phi_{AN2})\mathbf{e}_{x,k} + (\theta_2 \sin\phi_{AN2})\mathbf{e}_{y,k}, \\
\mathbf{r}_{k,3} &= (2\theta_2 \cos\phi_{AN2})\mathbf{e}_{x,k} - (2\theta_2 \sin\phi_{AN2})\mathbf{e}_{y,k}, \\
\mathbf{r}_{k,4} &= (\theta_2 \cos\phi_{AN2})\mathbf{e}_{x,k} + (\theta_2 \sin\phi_{AN2})\mathbf{e}_{y,k}.
\end{aligned}$$

Similar vectors $\{\mathbf{r}_{j,\ell}\}$ generate rotations on the unaddressed qubits. The phase is chosen so that $\cos\phi_{AN2} = -\frac{\theta_1}{4\theta_2}$ and the first-order error term cancels so long as $\theta_1 < 4\theta_2$. Similar to N2, the symmetry $\mathbf{r}_{j,2} = \mathbf{r}_{j,4}$ results in the cancellation of the second-order

error term. Written as a sequence of simple rotations, the sequence applies $U_{k,AN2} = R(\theta_2, \phi_{AN2})R(2\theta_2, -\phi_{AN2})R(\theta_2, \phi_{AN2})R(\theta_1, 0)$ to the addressed qubit and $U_{j,AN2} = 1 + O(\epsilon_j^3)$ to the unaddressed qubits. The fidelity of the identity operation on the unaddressed qubits is $\mathcal{F} = 1 - \epsilon_j^6(32\,\theta_1^2\theta_2^4 + 14\,\theta_1^4\theta_2^2 - \theta_1^6)/9216 + O(\epsilon_j^8)$. We may recover the original N2 sequence by replacing $\theta_2 \to \pi$.

5.1.3 Transformed-augmented sequences

One drawback of augmented pulse sequences is that in general the group product $U_k = \prod_\ell R_k(\theta_\ell, \phi_\ell)$ yields an effective qubit rotation about an axis outside the X-Y plane. This makes these sequences difficult to use since they cannot serve as drop-in replacements for a simple resonant pulse, for instance $U_T = R_k(\vartheta, 0)$. We can arbitrarily rotate the effective rotation axis by implementing two additional pulses which act as a similarity transformation. In particular we can choose to add rotations Υ_k and $\Upsilon_k^\dagger$ such that sequence $\Upsilon_k U_k \Upsilon_k^\dagger = R(\vartheta, 0)$ implements a rotation about the X axis. We describe a method for determining transformed sequences below:

1. Decompose U_k into the form $U_k = \exp(-\mathrm{i}\vartheta a^\mu H_\mu)$. The angle ϑ is the net rotation angle of the sequence. The unit vector $\vec{a} = (a^x, a^y, a^z)$ sets the axis of rotation in the Bloch sphere.

2. Select the rotation $\Upsilon_k = R_k(\theta_0, \pi/2 + \phi_0)$ that returns the axis $\vec{a}$ to the X-Y plane while minimizing θ_0 (proportional to time). The optimal rotation is given by

$$\theta_0 = \arctan2\left(a^z, \sqrt{(a^x)^2 + (a^y)^2}\right),$$
$$\phi_0 = \arctan2\left(a^y, a^x\right),$$

   where arctan2 is a arctangent function returns an angle in the correct quadrant.

3. Subtract the phase ϕ_0 from each pulse in the sequence $\Upsilon_k U_k \Upsilon_k^\dagger$. This aligns $\vec{a}$ along the X axis. The transformed sequence implements $R_k(\vartheta, 0)$ on the addressed qubit.

We call sequences which use similarity transformations to rotate the effective gate transformed sequences. The similarity transform only rotates the net rotation axis of the sequence. The net rotation angle, and also error correcting properties, are controlled by the

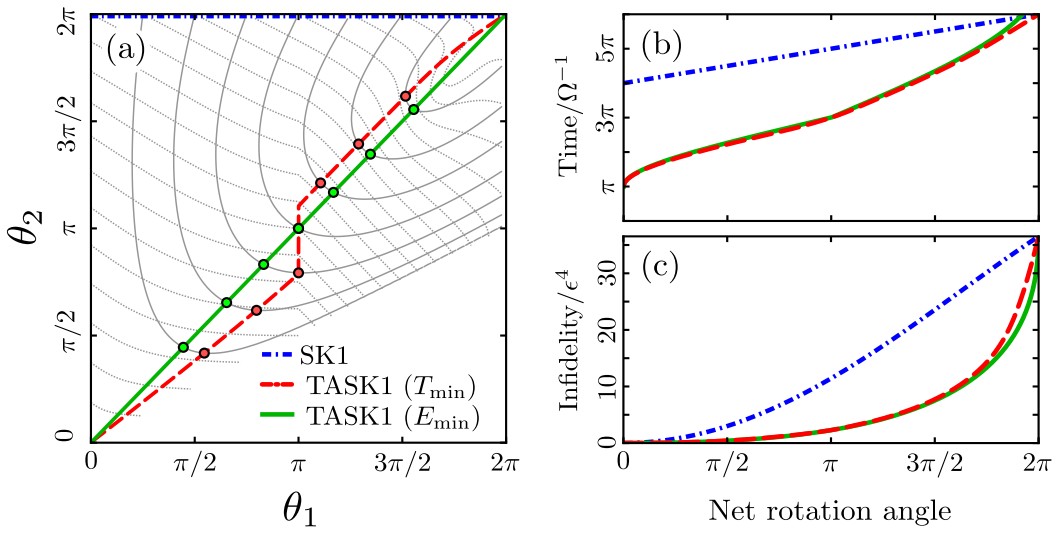

Figure 5.3: The TASK1 family of pulses. Each TASK1 sequence is parameterized by $\{\theta_1, \theta_2\}$ with $\theta_1 < 2\theta_2$. (a) Contours of the net rotation angle (solid) and pulse area (dashed) over the parameter space in intervals of $\pi/4$. Error-minimal and time-minimal sequences are plotted. (b) Comparison of sequence time, e.g., total pulse area. (c) Comparison of sequence infidelity.

compensating sequence U_k sandwiched between the transform pulses.

5.1.3.1 TASK1

We call the transformed-augmented SK1 sequences TASK1. Although TASK1 has a greater number of individual pulses than SK1, the added flexibility of this construction yields sequences with improved properties. Figure 5.3a plots the TASK1 family in terms of the parameters $\{\theta_1, \theta_2\}$. We plot the net rotation angle applied to addressed qubits (solid contours, intervals of $\pi/4$) and the total pulse area (dashed contours, intervals of $\pi/4$) as a function of the sequence parameters. No valid sequences exist wherever $\theta_1 \geq 2\theta_2$ since these fail to satisfy a triangular inequality.

We find optimal TASK1 sequences by numerically performing a constrained optimization using a sequential least-squares programming[1] (SLSQP) algorithm. Consider the set

[1]We use the SLSQP routines packaged in the `scipy.optimize` Python module

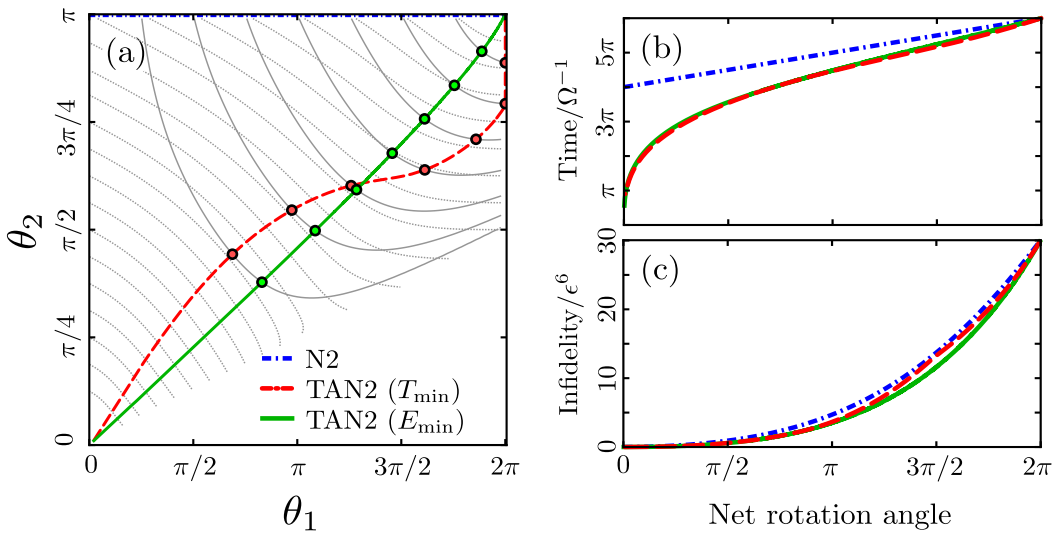

Figure 5.4: The TAN2 family of pulses. Each TAN2 sequence is parameterized by $\{\theta_1, \theta_2\}$ with $\theta_1 < 4\theta_2$. (a) Contours of the net rotation angle (solid) and pulse area (dashed) over the parameter space in intervals of $\pi/4$. Error-minimal and time-minimal sequences are plotted. (b) Comparison of sequence time, e.g., total pulse area. (c) Comparison of sequence infidelity.

of sequences that perform a particular net rotation $U_T = R_k(\vartheta, 0)$. The error-minimal sequence performs the rotation while minimizing the leading order error term of the sequence infidelity. The time-minimal sequence performs the rotation while minimizing the total pulse area. In figures 5.3b and 5.3c we plot the pulse area and infidelity for net rotation angles $\vartheta \in [0, 2\pi)$. The two optimal sequences outperform SK1 in both speed and accuracy. We find that the optimal sequences perform similarly, and we can produce sequences that improve both gate fidelity and time simultaneously. In particular for $U_T = R_k(\pi, 0)$, the optimal sequences perform the gate with a 80% reduction in the infidelity and a 40% reduction in total pulse area compared to SK1. Further improvements are possible if we consider sequences constructed of additional (but on average shorter) pulses.

5.1.3.2 TAN2

The transform-augmented N2 sequences are called TAN2. Figure 5.4a plots the TAN2 family in terms of the parameters $\{\theta_1, \theta_2\}$. Again we plot the net rotation angle applied to addressed qubits (solid contours, intervals of $\pi/4$) and the total pulse area (dashed

contours, intervals of $\pi/4$) as a function of the sequence parameters. Valid TAN2 sequences require $\theta_1 < 4\theta_2$. We use the same optimization methods to produce error-minimal and time-minimal TAN2 sequences. Figures 5.4b and 5.4c plot the pulse area and infidelity for the optimal TAN2 sequences and for N2. Due to the rather constrained parameterization the improvements over N2 are modest. For $U_T = R(\pi, 0)$ the optimal TAN2 sequence performs the gate with a 25.2% reduction in the infidelity and a 10.8% reduction in the total pulse area compared to N2. Further improvements are possible if we consider other parameterizations which allow additional pulses.

5.2 Experimental demonstration

We have recently demonstrated improved addressing of individual $^{40}Ca^{+}$ ions using narrowband compensating sequences. To date, we have successfully tested the technique now in two separate ion trapping systems. The first system uses a conventional room temperature vacuum chamber, described in detail in section 3.1.3.2. The second system is based on a closed-cycle liquid helium cryostat; details of our cryostat apparatus are described in Ref. [125]. The data reported here were collected using the cryostat system.

Both systems use identical microfabricated GTRI Gen II surface electrode traps [32] (see figure 3.2). These traps contain 44 segmented DC electrodes which allow the location of the axial potential minimum to be controlled to better than < 500 nm. Qubit operations rely on a 729 nm laser, which we orient parallel to the trap plane and at a 45° angle from the trap axis. We choose this orientation so each motional mode is accessible during sideband cooling. In applications with more stringent addressing requirements, during qubit operations one should use a second 729 nm beam oriented at 90° to minimize the beam cross-section along the trap axis.

5.2.1 Composite sequence inversion profiles

Narrowband sequences behave differently for addressed qubits where the laser field is intense compared to unaddressed qubits where the laser is weak [107, 116]. To confirm this behavior, we perform an experiment that measures the population transfer between qubit states during a gate produced by a narrowband sequence. The experiment uses a single $^{40}Ca^{+}$

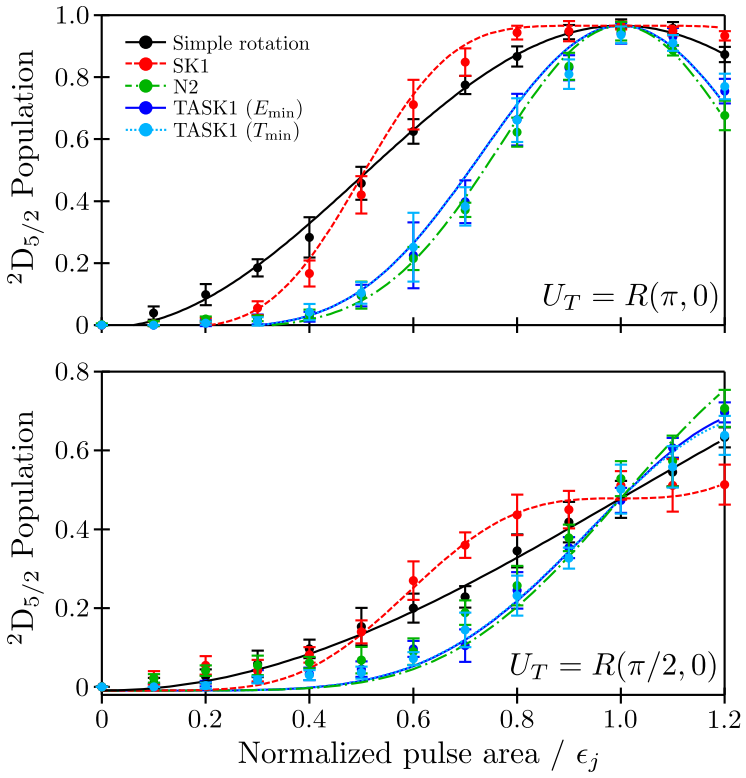

Figure 5.5: $^2D_{5/2}$ population as a function of systematic error for logical gates produced by narrowband sequences. To simulate different field strengths the pulse areas are uniformly scaled by adjusting the pulse lengths. In the top panel sequences apply $R(\pi, 0)$ when $\epsilon_j = 1$. In the lower panel sequences implement $R(\pi/2, 0)$ when $\epsilon_j = 1$. Curves are signals predicted by theory, adjusted to account for error related to qubit preparation and detection.

ion placed at the center of the 729 nm laser beam. For the data here, the qubit transition Rabi frequency at the beam center is $\Omega = 2\pi \times 0.38$ MHz. Moderate 729 nm laser powers are used to avoid off-resonant coupling to other $^2S_{1/2} \rightarrow ^2 D_{5/2}$ transitions which slowly transfer population out of the qubit states. Before each experiment, the ion is sideband cooled near the motional ground state with typically less than $\langle n \rangle < 0.3$ phonons remaining in each motional mode. The experiment prepares the qubit in $|1\rangle$, applies a gate using a simple rotation or a narrowband sequence, and then determines the population transfer by measuring the remaining population in $|1\rangle$. To simulate the effect of different laser field strengths, we uniformly scale the pulse area of every pulse in the sequence by adjusting the pulse duration. Dynamically this is equivalent to probing the ion at different values of the error parameter ϵ_j.

Figure 5.5 plots the measured excitation profiles produced by compensated gates, overlayed on the signal predicted from theory. The amplitudes of the theory curves are adjusted to account for errors related to qubit state preparation and detection. The top graph plots the response for sequences which implement $R(\pi, 0)$ on the addressed ion. The lower graph plots sequences which implement $R(\pi/2, 0)$. We find that narrowband sequences suppress population inversion when $\epsilon_j \ll 1$ while still performing the target gate when $\epsilon_j = 1$, in good agreement with theory. In particular the TASK1 sequences and N2 perform especially well, however since N2 is a second-order sequence it is actually much more accurate.

5.2.2 Compensation of addressing error

A second experiment directly observes addressing error compensation by measuring the population inversion as a function of the ion position relative to the center of the 729 nm beam. Since the ion position is accurately controlled by applying appropriate trapping voltages to the segmented DC electrodes, we control the relative positioning of the system by fixing the laser in place and moving the ion to a specific location in the beam profile. This task is facilitated by intentionally expanding the beam along the trap axis so that the ion may placed accurately relative to the scale of beam waist.

We measure the 729 nm beam waist by observing qubit population transfer as a function of ion position. The experiment moves the ion to a particular location, sideband cools and initializes in $|1\rangle$, and probes the qubit with a simple pulse that applies $R(\pi, 0)$ when the ion is located at the beam center. We measure the qubit population transfer by observing the remaining population in $|1\rangle$. The beam waist is extracted by fitting the observed population to a theoretical curve valid for Gaussian beams $P(z/w_0) = \frac{1}{2}\left[1 - \cos\left(\pi \mathrm{e}^{-z^2/w_0^2}\right)\right]$, where z is the displacement of the ion from the beam center and w_0 is the $1/\mathrm{e}^2$ Gaussian beam waist measured along the trap axis, in contrast to the waist measured transversely from the beam axis. Alternatively one could measure the Rabi frequency as a function of ion position and measure the beam profile directly. In the experiments here, the beam waist is $w_0 = 44.2 \pm 0.8$ μm.

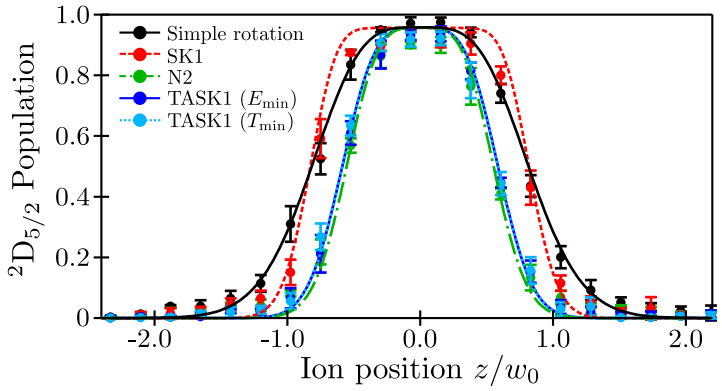

Figure 5.6: $^2D_{5/2}$ population as a function of ion displacement from the 729 nm beam center. At the center of the beam, the beam applies $R(\pi, 0)$ using either a simple pulse or a narrowband sequence. Curves are signals predicted by theory, adjusted similar to figure 5.5.

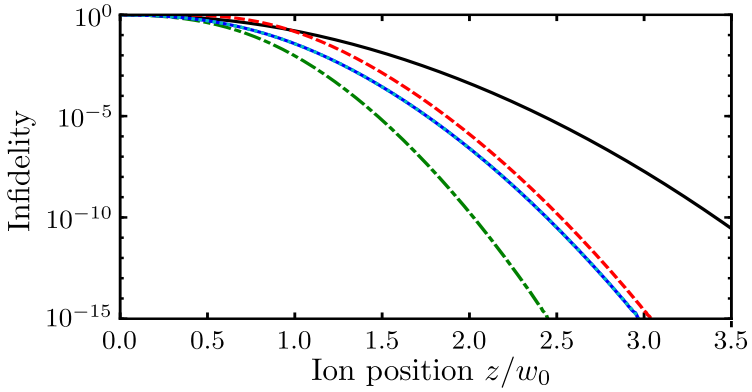

Figure 5.7: Infidelity of the identity operation on unaddressed qubits as a function of displacement from the beam center. Each sequence implements $R(\pi, 0)$ on the addressed qubit. The sequence order controls the scaling of the infidelity.

A similar technique measures effective beam profiles for gates implemented using narrowband sequences, now replacing the simple pulse with a pulse sequence that implements $R(\pi, 0)$ when the ion is located at the beam center. Figure 5.6 plots the measured excitation profile as a function of ion position, overlayed on the signal predicted from theory. The theoretical curves assume a Gaussian beam profile and are adjusted to account for fixed state preparation and detection errors, similar to before. Although physically the beam is unchanged, narrowband sequences effectively narrow the profile by suppressing unwanted qubit rotations far from the beam center, where the field is weak.

Assuming that poor ion addressing is the sole source of error, we calculate theoretical fidelities of $R(\pi, 0)$ gates produced using simple pulses and also several narrowband sequences. Figure 5.7 plots the infidelity as a function of ion displacement from the beam center. Narrowband sequences alter the scaling of the infidelity with respect to the systematic error, for instance, infidelity of the N2 sequence scales as $O(\epsilon_j^6)$ whereas a simple pulse scales as $O(\epsilon_j^2)$. Remarkably, the N2 sequence produces local $R(\pi, 0)$ gates with infidelities below the $\sim 10^{-4}$ error-correction threshold even with nearby ions as close as $1.33\, w_0$ from the beam center. Instead if we implemented the gate using a simple pulse neighboring ions must be further than $2.17\, w_0$ to achieve the same accuracy. Further improvements are possible by implementing other narrowband sequences. Brown, Harrow, and Chuang [114] and later Vitanov [118] have studied sequences which may be made arbitrarily narrow, however these sequences rapidly become too long to be practical in most experiments. A practical narrowband sequence should balance the often conflicting requirements of gate accuracy and sequence duration. Further research should consider the design of time-optimal narrowband sequences.

5.3 Summary

Narrowband sequences are a method of reducing addressing errors caused the spatial width of laser beams. These pulse sequences could be used with beam steering systems [122] to achieve robust single ion addressing in an ion-trap quantum computer [126]. We have described the SK1 and N2 narrowband sequences, and novel constructions which generalize

their form to yield sequences with lower operation times and improved error compensation. We demonstrated these techniques in a experiment on $^{40}Ca^{+}$ qubits. Currently we are studying more general sequences which perform time-optimal narrowband compensation.

CHAPTER VI

UNIFORM MICROWAVE GATES USING COMPENSATING SEQUENCES

This chapter describes a microfabricated surface-electrode ion trap with a pair of on-chip waveguides that generate local microwave magnetic fields [127]. The microwaves drive transitions between the $^2S_{1/2}$ hyperfine levels of $^{171}Yb^+$, enabling arbitrary single-qubit gates on the hyperfine qubit. Devices with integrated near-field microwave structures offer a possible simplification since the laser system for qubit operations is no longer required [128–132]. In addition, high-quality microwave sources are affordable, easily miniaturized, and are simple to maintain. This technology offers a compelling route to a future "turn-key" ion-trap quantum processor.

However, these systems are sensitive to systematic errors caused by an imperfect microwave field. Here we introduce broadband compensating pulse sequences, which we use to correct amplitude errors caused by the inherent inhomogeneity of the microwave field. Section 6.1 describes the trap, integrated waveguides, microwave polarization control, and characterizes the microwave field. Section 6.2 introduces broadband compensating sequences. Section 6.3 describes an experiment which uses broadband sequences to apply uniform global single qubit rotations.

6.1 A surface-electrode trap with integrated microwave waveguides

6.1.1 Trap geometry and electrode structures

The trap conforms to a symmetric five-wire surface-electrode Paul trap geometry [30] fabricated on a 11×11 mm^2 silicon die (figure 6.1a) similar to the designs reported in [32, 34, 133] and the description provided in section 3.1.3. Electrodes etched into three sputtered aluminum layers separated by insulating silicon dioxide films produce electric fields that trap the ion. Radio-frequency (RF) potentials applied to two parallel electrodes provide radial ion confinement (in the x-y plane, figure 6.1b) 59 μm above the electrodes. Quasi-static

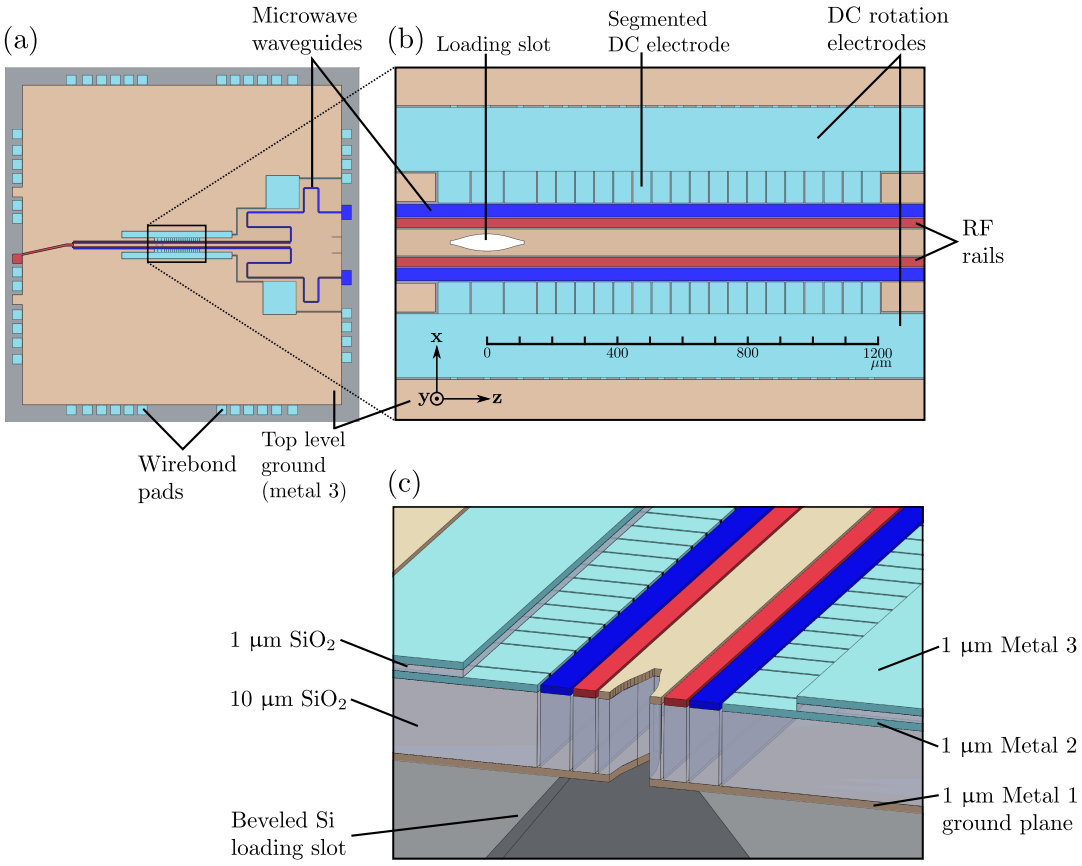

Figure 6.1: GTRI microwave surface-electrode trap with on-chip microwave waveguides. (a) A schematic of the 11×11 mm^2 silicon chip (b) The active trapping region, showing RF and DC trapping electrodes, the shaped loading slot, and the on-chip microwave waveguides. (c) A cross section showing internal layers (the vertical direction is scaled by $10\times$ for visual clarity).

potentials applied to segmented DC electrodes confine and transport ions along z. The RF electrodes are 30 μm wide along x with an inner edge-to-edge separation of 92 μm. The segmented DC electrodes are 56 μm wide along z except for six 100 μm wide electrodes bordering the loading zone. Two additional DC electrodes traversing the entire length of the trapping region are used to apply uniform x-y fields and to rotate the radial principal axes. Each electrode is separated from neighboring conductors by 4 μm gaps. Each DC electrode incorporates a 60 pF plate capacitor (1 mm^2 area) to filter unwanted RF pickup [32]. A loading slot allows a thermal beam of neutral Yb to reach the trapping volume from a resistively heated oven located below the trap.

6.1.2 Integrated waveguides

The trap includes a pair of conductor-backed coplanar waveguides that generate local microwave magnetic fields. Each waveguide includes a 40 μm wide electrode with 4 μm gaps to neighboring conductors, and 10 μm of SiO_2 separate the coplanar layer from the ground plane below (figure 6.1b). The waveguides support a $\omega_{mw} = 2\pi \times 12.64$ GHz quasi-TEM guided mode resonant with the hyperfine splitting between the $F = 0$ and $F = 1$ manifolds in the $^2S_{1/2}$ ground state of $^{171}Yb^+$ (see figure 3.5c). In the ideal case, currents in each waveguide generate a magnetic field along the trapping axis

$$\vec{B}(z,t) = I_1(z,t) \begin{pmatrix} \beta_x \\ \beta_y \\ 0 \end{pmatrix} \cos\phi_1 + I_2(z,t) \begin{pmatrix} \beta_x \\ -\beta_y \\ 0 \end{pmatrix} \cos\phi_2, \tag{6.1}$$

where each term corresponds to the field produced by a single waveguide. Here ϕ_1 and ϕ_2 are phases on the microwave current sources, $I_1(z,t)$ and $I_2(z,t)$ are spatially integrated axial current densities for each waveguide, and $\beta_x \simeq 0.08$ mT/A and $\beta_y \simeq 0.17$ mT/A are constants related to the geometry of the waveguide mode. Due to the symmetric placement of the waveguides about the trapping axis, the geometric constants along y has equal magnitude but opposite orientation for the two waveguides. The waveguides terminate in an open circuit at a position that is approximately a quarter-wavelength from the trap center, which produces a standing wave field with maximum amplitude and uniformity in the trapping

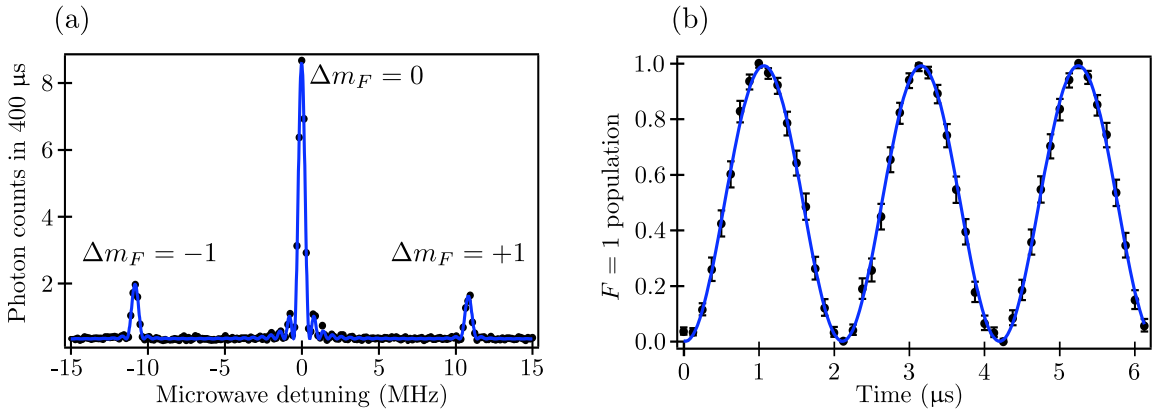

Figure 6.2: Microwave spectroscopy of the $^{171}Yb^+$ $^2S_{1/2}$ states. (a) Resolved hyperfine transitions between $^2S_{1/2}(F = 0) \rightarrow^2 S_{1/2}(F = 1)$ sublevels driven by a microwave field produced by a single waveguide. The qubit uses the $\Delta m_F = 0$ transition. (b) Qubit Rabi oscillations ($\Omega = 2\pi \times 0.49$ MHz) driven by resonant microwaves from both waveguides.

region. A small traveling wave component also exists due to on-chip attenuation.

Far from the trap center, the waveguides meander to fit a complete wavelength on the chip and then terminate on wirebond pads at the edge of the chip. Extending the waveguides to a full wavelength places a current node at the wirebond pads and reduces the potential for resistive power loss in the connections. A series of 25.4 µm diameter aluminum wirebonds connect the chip waveguides to two PCB waveguides that route microwaves from the edge of the trap package Connections between the PCB top level ground and the on-chip metal 1 and metal 2 ground planes are symmetric about each microwave electrode. Quarter-wave transformers match the 50 ohm impedance of the PCB waveguide to the 27 ohm on-chip characteristic impedance. The PCB is fabricated using a 254 µm thick Rogers 4350B substrate with two 18 µm thick copper foil conductive layers and a 3-6 µm electroless nickel immersion gold (ENIG) finish. The skin depth in the PCB at ω_{mw} is comparable to the thickness of the lossy nickel layer resulting in ~ 3 dB of power loss between the microwave connector and wirebonds.

6.1.3 Microwave spectroscopy and polarization control

The waveguides generate a microwave magnetic field that drives transitions between the $^2S_{1/2}$ hyperfine levels of $^{171}Yb^+$. A static 0.74 mT field along y defines the quantization

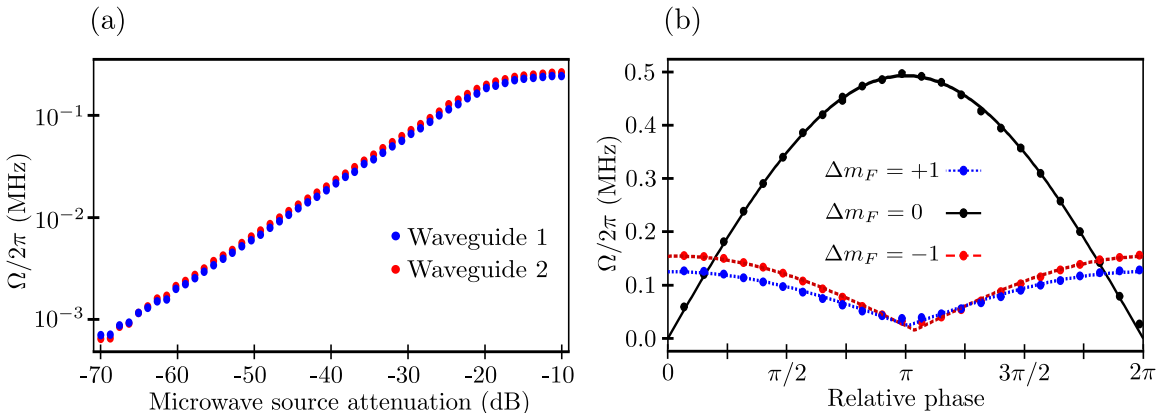

Figure 6.3: Polarization control of microwave fields. (a) Each waveguide is calibrated by measuring the Rabi qubit frequency against the microwave source power. The nonlinearity at power is due to amplifier saturation. (b) Polarization control via microwave power balancing and relative phase tuning between the two waveguides.

axis and lifts the degeneracy of the $^2S_{1/2}(F = 1)$ triplet. Each waveguide produces a magnetic field which contains both a y-polarized component that couples to the $\Delta m_F = 0$ qubit transition and also a transverse x-polarized component that couples to the $\Delta m_F = \pm 1$ transitions. We resolve each transition in an experiment that measures the hyperfine spectrum with microwave power applied to a single waveguide. The experiment prepares a qubit in $|0\rangle$ by optical pumping, applies microwave power for a fixed interval of time, and measures the resulting population transfer into the $^2S_{1/2}(F = 1)$ states through state-selective fluorescence of the 369 nm transition. Figure 6.2a shows the resulting hyperfine spectrum acquired by varying the microwave frequency. From the relative oscillator strengths of the transitions, we estimate the ratio of polarization components for each waveguide as $|\beta_x|/|\beta_y| \simeq 0.46$, in good agreement with a finite-element model.

We observe Rabi oscillations in a similar experiment, where now both waveguides resonantly drive the $\Delta m_F = 0$ qubit transition. Figure 6.2b shows Rabi oscillations at a frequency $\Omega = 2\pi \times 0.49$ MHz observed from an ion located $z = 300$ μm from the center of the loading slot.

The polarization of the near-field microwaves may be controlled by adjusting the relative amplitude and phase of the microwave currents. In particular, the polarization may be aligned along the quantization axis, thereby maximizing the qubit transition strength while

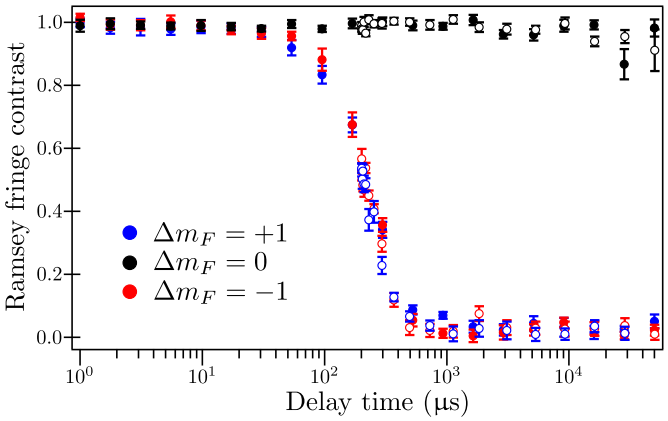

Figure 6.4: Measurement of $^{171}Yb^+$ $^2S_{1/2}$ coherence lifetime by Ramsey spectroscopy. Solid markers indicate data taken on stationary ions. Open markers correspond to ions undergoing transport. The Ramsey fringe contrast decays in $T_2 = 306 \pm 30$ μs for the $\Delta m_F = \pm 1$ transitions. The lifetime of the $\Delta m_F = 0$ qubit transition far exceeds 10^5 μs. No significant difference in coherence lifetimes for stationary versus shuttled ions is observed.

also suppressing off-resonant $\Delta m_F = \pm 1$ transitions. This is especially helpful in preventing leakage out of the qubit states during short high-power microwave pulses. The active and passive microwave components supplying microwave currents to the waveguides are not perfectly power-balanced and phase-matched. We calibrate the microwave sources by first driving each waveguide independently to map the relationship between source power and Rabi frequency (figure 6.3a). Once the field amplitudes from the waveguides have been equalized, the relative phase between microwave currents $\phi_2 - \phi_1$ can be adjusted produce an arbitrary linear polarization in the x–y plane. Figure 6.3b shows the resonant Rabi frequency for each of the three transitions as the relative phase is varied, demonstrating suppression of the $\Delta m_F = \pm 1$ transitions at $\phi_2 - \phi_1 = \pi$. We suspect that the mismatch between the $\Delta m_F = \pm 1$ curves in figure 6.3b is caused by a small frequency dependent dispersion in the microwave electronics.

6.1.4 Hyperfine coherence

We estimate the coherence of the qubit and the $\Delta m_F = \pm 1$ transitions using Ramsey spectroscopy [134, 135]. The experiment prepares the state $|0\rangle$ by optical pumping, applies $R(\pi/2, 0)$ where now the rotation is with respect to the transition being probed, waits

a variable free-precession delay time τ, applies $R(\pi/2, \varphi)$ where the phase φ is variable, and measures the $^2S_{1/2}(F = 1)$ population by state-selective fluorescence. Scanning the analysis phase φ yields a sinusoidal Ramsey fringe, which we fit to extract a fringe contrast. The fringe contrast decays as the superposition state decoheres during the free-precession delay, frequently due to ambient magnetic field noise that causes AC-Zeeman shifts. At zero magnetic field, the qubit transition is first-order insensitive to this effect. Repeating the measurement for several delay times yields a decay curve characterizing the coherence lifetime of the superposition.

We perform two variants of the Ramsey spectroscopy experiment. In the first, the ion is held stationary at $z = 300$ μm for the microwave pulses and the free-precession delay. The second variant is similar, only during the delay the ion is rapidly shuttled from $z = 300$ μm to $z = 400$ μm in 100 μs, held stationary for $\tau - 200$ μs, and then shuttled back in 100 μs. Figure 6.4 plots the observed Ramsey fringe decay as a function of the delay time. Superpositions along the $\Delta m_F = \pm 1$ transitions dephase in a 1/e time $T_2 = 306 \pm 30$ μs, while the qubit transition dephases much more slowly ($T_2 \gg 10^5$ μs). No significant difference in coherence lifetimes for stationary ions versus shuttled ions was observed.

6.1.5 Field uniformity

The standing wave current in the waveguides produces a microwave field with non-uniform amplitude along the trap axis. This field inhomogeneity introduces systematic amplitude errors when applying global single-qubit rotations. Figure 6.5 shows the measured Rabi frequency of the qubit transition at several positions along the trap axis. We observe a maximum Rabi frequency of $2\pi \times 0.52$ MHz, corresponding to a field amplitude of 0.037 mT, located $z_0 = 957$ μm from the loading slot center. Finite element calculations predict an antinode location at $z = 895$ μm, in reasonable agreement with the experiment. These models indicate that the maximum field corresponds to a local current in each electrode of $|I_z(z_0)| \simeq 0.1$ A.

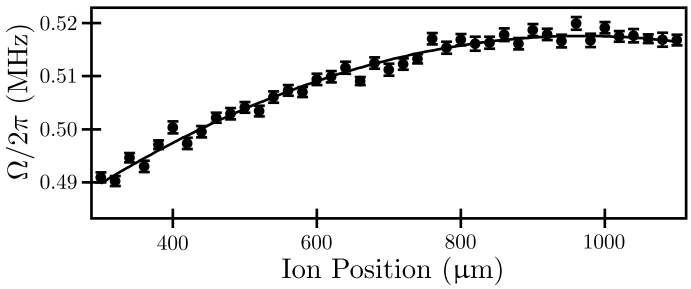

Figure 6.5: Observed qubit Rabi frequency as a function of axial ion position. The microwave current and polarization is held constant. The solid line is a quadratic fit. We measure a maximum Rabi frequency of $2\pi \times 0.52$ MHz located $z = 957$ μm from the loading slot center, and a $< 6\%$ amplitude variation.

6.2 Broadband compensating sequences

Systematic amplitude errors, such as those introduced by an inhomogeneous microwave field, limit the fidelity of quantum gates. Gate fidelity could be improved by implementing broadband compensating pulse sequences [107, 117]. Broadband sequences enable accurate control even if the field amplitude varies significantly from the ideal value. Section 6.2.1 introduces a mapping that converts narrowband sequences into an analogous broadband sequence. Section 6.2.2 describes the simple broadband sequences SK1 and B2.

6.2.1 A mapping between the narrowband and broadband sequences

All compensating pulse sequences satisfy certain Lie algebraic properties when viewed in the interaction (toggling) frame, see section 4.2 for details. Compensating sequences for separate error models differ in that they satisfy these properties in distinct interaction frames. In some cases sequences of one type may be converted into another using a frame transformation.

We developed a method to convert a narrowband sequence composed of simple pulses into an associated broadband sequence. Let $U_{NB} = \prod_{\ell}^{n} \exp(\mathbf{r}_\ell)$ represent an nth-order narrowband pulse sequence, where the vectors $\{\mathbf{r}_\ell\}$ are the associated rotation generators on the Lie algebra. We desire a new set of generators $\{\mathbf{r}'_\ell\}$ which produce a broadband sequence. These sets of vectors will be images of each other under a certain frame transformation.

Specifically if,

$$\mathbf{r}'_\ell = \left(\prod_{m=0}^{\ell-1} \mathrm{e}^{\mathbf{r}_m} \right) \mathbf{r}_\ell \left(\prod_{m=0}^{\ell-1} \mathrm{e}^{\mathbf{r}_m} \right)^\dagger \tag{6.2}$$

where $\exp(\mathbf{r}_0) = 1$, then $U_{BB} = \prod_\ell^n \exp(\mathbf{r}'_\ell)$ is a broadband sequence of the same order. U_{NB} and U_{BB} are related in the sense that the distorted controls trace similar paths in their respective interaction frame Lie algebras. Further, if the algebra was rotated using a similarity transformation Υ, the generators $\{\Upsilon \mathbf{r}_\ell \Upsilon^\dagger\}$ would still produce a broadband sequence since the interaction frame Magnus terms $\{\Upsilon\tilde{\mathbf{\Omega}}_1\Upsilon^\dagger, \Upsilon\tilde{\mathbf{\Omega}}_2\Upsilon^\dagger, \ldots, \Upsilon\tilde{\mathbf{\Omega}}_n\Upsilon^\dagger\}$ still simultaneously equal zero at the end of the sequence. Interpreted geometrically, compensation relies on topological properties of the distorted path, but does not depend on the orientation of the interaction-frame algebra.

6.2.2 Simple broadband sequences

6.2.2.1 SK1

A simple non-trivial broadband sequence results from applying the transformation (6.2) to SK1 (see section 5.1.1.1), yielding the vectors

$$\begin{aligned}
\mathbf{r}'_1 &= \vartheta \mathbf{e}_x \\
\mathbf{r}'_2 &= 2\pi \cos\phi_{SK1} \left(\mathrm{e}^{\mathbf{r_1}} \mathbf{e}_x \mathrm{e}^{-\mathbf{r_1}} \right) + 2\pi \sin\phi_{SK1} \left(\mathrm{e}^{\mathbf{r_1}} \mathbf{e}_y \mathrm{e}^{-\mathbf{r_1}} \right) \\
\mathbf{r}'_3 &= 2\pi \cos\phi_{SK1} \left(\mathrm{e}^{\mathbf{r_2}} \mathrm{e}^{\mathbf{r_1}} \mathbf{e}_x \mathrm{e}^{-\mathbf{r_1}} \mathrm{e}^{-\mathbf{r_2}} \right) - 2\pi \sin\phi_{SK1} \left(\mathrm{e}^{\mathbf{r_2}} \mathrm{e}^{\mathbf{r_1}} \mathbf{e}_y \mathrm{e}^{-\mathbf{r_1}} \mathrm{e}^{-\mathbf{r_2}} \right).
\end{aligned}$$

Further simplification if possible if we rotate the Lie algebra basis vectors according to the similarity transformation $\Upsilon \mathbf{e}_\mu \Upsilon^\dagger$, where we choose $\Upsilon = \exp(-\mathbf{r}_1) = R(-\vartheta, 0)$. Recognizing that $\exp(\mathbf{r}_2) = -1$ since $\mathbf{r}_2$ generates a 2π rotation, we find that $\{\mathbf{r}'_\ell\} = \{\mathbf{r}_\ell\}$. Since the transformed vectors $\{\mathbf{r}'_\ell\}$ are identical to the narrowband case, they generate the same sequence of rotations; the SK1 sequence is both a first-order broadband sequence and also a first-order narrowband sequence. Sequences with both broadband and narrowband character are called passband [107]. Written in terms of simple rotations, the sequence is $U_{SK1} = R(2\pi, -\phi_{SK1}) R(2\pi, \phi_{SK1}) R(\vartheta, 0)$ where the phase satisfies $\cos\phi_{SK1} = -\frac{\vartheta}{4\pi}$.

Figure 6.6 draws the trajectory of qubit under an SK1 sequence acting to compensate a 20% amplitude error. In the qubit frame, the net evolution approximates the correct gate

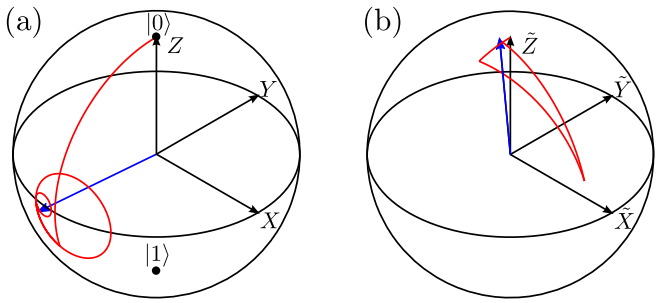

Figure 6.6: Qubit trajectory during an SK1 sequence used to compensate an amplitude error. Here $\epsilon = 0.2$, corresponding to a 20% error in the field amplitude. (a) Trajectory followed in the qubit frame. (b) Trajectory followed in the interaction (toggling) frame.

with fidelity $\mathcal{F} = 1 - \epsilon^4\theta^2(16\pi^2 - \theta^2)/128 + O(\epsilon^6)$. In the interaction frame the controls are chooses so that the distortion nearly produces the identity over the duration of the sequence. Reorienting the algebra using Υ only rotates the basis vectors; on the Bloch sphere this aligns $\tilde{Z}$ to point along $\Upsilon\tilde{Z}\Upsilon^\dagger = -\tilde{Y}$.

6.2.2.2 B2

A second-order broadband sequence results from applying the transformation (6.2) to N2 (see section 5.1.1.2). Choosing to rotate the Lie algebra according to $\Upsilon = \exp(-\mathbf{r}_1)$ yields,

$$\begin{aligned}
\mathbf{r}'_1 &= \vartheta\mathbf{e}_x \\
\mathbf{r}'_2 &= \pi\cos\phi_{B2}\mathbf{e}_x + \pi\sin\phi_{B2}\mathbf{e}_y \\
\mathbf{r}'_3 &= 2\pi\cos(3\phi_{B2})\mathbf{e}_x + 2\pi\sin(3\phi_{B2})\mathbf{e}_x \\
\mathbf{r}'_4 &= \pi\cos\phi_{B2}\mathbf{e}_x + \pi\sin\phi_{B2}\mathbf{e}_y,
\end{aligned}$$

where $\cos\phi_{B2} = \cos\phi_{N2} = -\frac{\vartheta}{4\pi}$ is the same phase for N2. Written as a sequence of simple rotations, $U_{B2} = R(\pi,\phi_{B2})R(2\pi,3\phi_{B2})R(\pi,\phi_{B2})R(\vartheta,0)$. We call this sequence B2, recognizing that it may be thought of as a broadband analogue of N2. Like N2, the B2 sequence was first discovered by Steven Wimperis [117], who called it BB1. Brown later generalized B2 to Bn [114, 123], which compensates amplitude errors to order $O(\epsilon^n)$.

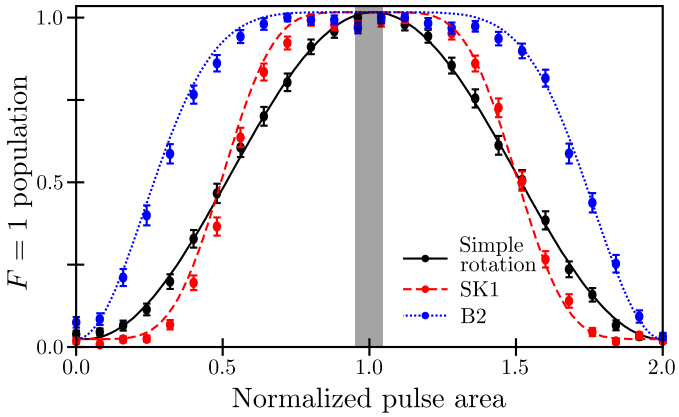

Figure 6.7: $^2S_{1/2}(F = 1)$ population as a function of systematic error for logical X gates produced by broadband sequences. The pulse areas are uniformly scaled by adjusting the pulse lengths. The solid curves are the signals predicted by theory, adjusted to account for a known qubit-detection error. The shaded area encloses the range of systematic microwave amplitude error observed over the entire trapping region.

6.3 Global rotations using broadband sequences

We return to our previous discussion regarding the uniformity of the microwave field produced by the on-chip waveguides. The field non-uniformity acts as a position-dependent amplitude error. This is problematic when implementing global single-qubit rotations on multiple ions located at different positions in the trap. To improve single-qubit gate uniformity, we implement global gates using broadband compensating pulse sequences. The excitation profiles of broadband pulse sequences enable global rotations on many qubits, although the microwave amplitude may differ significantly between distant ions.

6.3.1 Composite sequence inversion profiles

We demonstrate compensated X-gates constructed from first-order SK1 [114] and second-order B2 [117] sequences. Since $R(\pi, 0) = -iX$, these gates are equivalent to a π-rotation with an additional global phase. The experiment prepares the qubit in $|0\rangle$, applies a logical X-gate, and then measures the population in the $F = 1$ manifold. To simulate the effect of systematic over/under rotations, we uniformly scale the pulse areas of every pulse in the sequence by adjusting the pulse duration. Figure 6.7 plots the measured excitation profiles produced by compensated gates, overlayed on the signal predicted by theory. Assuming the

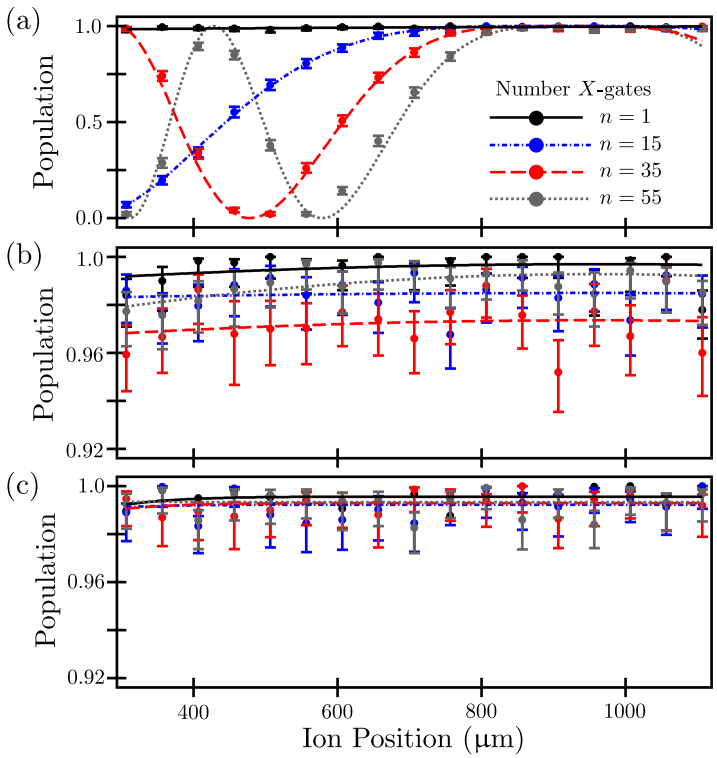

Figure 6.8: $^2S_{1/2}(F = 1)$ population after application of n sequential Pauli X-gates, with each gate implemented via a (a) simple rotation operator, (b) SK1 composite pulse sequence, or (c) B2 composite pulse sequence. Lines are fits to curves predicted by theory given the position-dependent Rabi frequency shown in figure 6.5.

field non-uniformity is the sole source of error, we calculate theoretical fidelities of X-gates. For the 6% amplitude deviation observed at $z = 300$ μm (see figure 6.5), a simple rotation performs a global X-gate with a minimum fidelity $\mathcal{F} \geq 0.995$, whereas SK1 and B2 perform the same gate with minimum fidelities of $\mathcal{F} \geq 1 - 1.5 \times 10^{-4}$ and $\mathcal{F} \geq 1 - 2.2 \times 10^{-7}$ respectively.

6.3.2 Compensated global microwave gates

As a demonstration of uniform global gates, we perform an experiment where n sequential effective X-gates are applied to a qubit initialized in $|0\rangle$. We calibrate gate times so that an ion located at the microwave amplitude maximum ($z_0 = 957$ μm) experiences nearly perfect rotations. Qubits displaced from the field maximum rotate at lower Rabi frequencies, acquiring an under-rotation error that accumulates as n increases. We measure the $F = 1$ population as a function of ion axial position and number of sequential gates. For gates

implemented by simple rotations we observe fringes (figure 6.8a) arising from the local qubit falling behind by an entire Rabi cycle relative to the maximal Rabi frequency. Instead by implementing SK1 or B2 pulses (figures 6.8b and 6.8c) error accumulates so slowly that the excitation profile remains flat over the trapping region after $n = 55$ logical X-gates. Our ability to resolve fringe structure in these cases is currently limited by systematic state-preparation and measurement errors and by the number of simple pulse operations we can implement.

We analytically calculate the fidelity scaling of the sequential logical X-gates as a function of the microwave field strength. For simple rotations, the fidelity drops as $\mathcal{F} = |\cos[\epsilon(z)\pi n/2]|$, where $\epsilon(z) = [\Omega(z) - \Omega(z_0)]/\Omega(z_0)$ is the fractional difference in Rabi frequencies between the ion location z and the field maximum. For SK1 pulses the fidelity scales as $\mathcal{F} = 1 - \frac{15}{128}\pi^4\epsilon(z)^4 n + O(\epsilon(z)^6)$, and for B2 the fidelity scales as $\mathcal{F} = 1 - \frac{5}{1024}\pi^6\epsilon(z)^6 n + O(\epsilon(z)^8)$.

6.4 Summary

We have developed a microfabricated surface-electrode ion trap with integrated microwave waveguides for performing arbitrary single-qubit gates on the $^{171}Yb^+$ hyperfine qubit. The polarization of the local microwave field can be tuned to minimize off-resonant coupling to adjacent hyperfine states. Broadband compensating sequences were discussed. We use these sequences to reduce amplitude errors introduced by microwave inhomogeneity. Instead, by implementing narrowband sequences one could apply local gates, thereby enabling single-ion addressing without requiring perfect field suppression at neighboring ions.

CHAPTER VII

MULTI-QUBIT COMPENSATING SEQUENCES

In principle, compensating pulses can be used to correct *unknown* systematic errors in single-qubit gates to arbitrary order [114]. In this chapter we extend compensating sequences to multi-qubit interactions. Our approach uses an inductive Cartan decomposition for the dynamical Lie algebra. This decomposition informs the construction of composite sequence for multi-qubit gates. We show compensating sequences may be used correct multi-qubit operations to arbitrary accuracy, provided that there exists two non-commuting control Hamiltonians with proportional error or one error-free Hamiltonian. The chapter is organized as follows: Section 7.1 describes the multi-qubit system, and simplifies the control problem using a Cartan decomposition. Section 7.2 considers two-qubit gates. Section 7.3 generalizes to n qubits and proves inductively that only two systematic errors need to be correlated to achieve arbitrary correction in all systematic errors.

7.1 Control theory and geometry of n qubits

The system we consider is n qubits with a set of dimensionless control Hamiltonians. In the absence of errors the system is universally controllable if the Hamiltonians generate the entire algebra $\mathfrak{su}(2^n)$ by addition and the Lie bracket [56, 58]. The very same technique can be used to determine if a composite pulse sequence exists [136]. Additionally, the Lie bracket can be used to constructively build pulses sequences, e.g. the balanced group commutator construction described in section 2.2.4.1.

For n qubits the corresponding Lie algebra is $\mathfrak{su}(2^n)$. As a convenient representation of the algebra we introduce the control Hamiltonians,

$$\begin{aligned} H_\mu &= \frac{1}{2}\sigma_\mu \\ H_{\mu\nu} &= \frac{1}{2}\sigma_\mu \otimes \sigma_\nu \\ H_{\mu\nu\rho\ldots} &= \frac{1}{2}\sigma_\mu \otimes \sigma_\nu \otimes \sigma_\rho \otimes \ldots, \end{aligned} \tag{7.1}$$

where $\sigma_1 = 1$ is the identity on the qubit and $\sigma_x = X$, $\sigma_y = Y$, and $\sigma_z = Z$ are the single qubit Pauli operators. For single-qubit Hamiltonians, the set $\{H_\mu\}$ matches the previously used control Hamiltonians for $\mathfrak{su}(2)$. The set (7.1) is known as the product operator basis [137]. The Lie algebra itself is spanned by a basis of skew symmeterized Hamiltonians, e.g. $\{\mathbf{e}_{\mu\nu\rho\ldots} = -\mathrm{i}H_{\mu\nu\rho\ldots}\}$. Furthermore since $\langle \mathbf{e}_{\mu\nu\rho\ldots}, \mathbf{e}_{\mu'\nu'\rho'\ldots}\rangle = \frac{2^n}{4}\delta_{\mu\mu'}\delta_{\nu\nu'}\delta_{\rho\rho'}\ldots$, the basis is orthogonal under the Hilbert-Schmidt inner product. The algebra is a $4^n - 1$ dimensional vector space since since the generator of the global phase $\mathbf{e}_{111\ldots} = -\frac{\mathrm{i}}{2}\bigotimes_{k=1}^{n} 1_k$ is outside of the algebra of $\mathfrak{su}(2^n)$. For any two generators $\mathbf{e}_i$ and $\mathbf{e}_j$, we find that either they commute $[\mathbf{e}_i, \mathbf{e}_j]$=0 or $[\mathbf{e}_i, \mathbf{e}_j] = \epsilon_{ijk}\mathbf{e}_k$, where ϵ_{ijk} is a Levi-Civita tensor. If they do not commute, the two operators generate a representation of $\mathfrak{su}(2)$.

The Lie algebra then imposes that given Pauli-operator generators with the same systematic control error, arbitrarily accurate composite pulses can be created, if and only if they do not commute. Furthermore, if they do not commute the resulting pulse sequence may have the same form as a single qubit pulse sequence, for example a two-qubit analogue of B2 [136]. A geometrical interpretation is that controlling two elements that do not commute is homomorphic to rotations on a sphere while the space for commuting elements is a 2-torus [138, 139].

7.1.1 Cartan decomposition of two-qubit gates

The Lie group of two-qubit gates is $SU(4)$. The corresponding algebra $\mathfrak{su}(4)$ is spanned by the vectors $\{\mathbf{e}_{\mu\nu}\}$, excluding $\mathbf{e}_{11}$, forming a 15-dimensional space. Rather than considering all fifteen controls simultaneously, we simplify the problem by dividing the algebra into subspaces. Choose $\mathfrak{su}(4) = \mathfrak{k} \oplus \mathfrak{m}$ where

$$\mathfrak{k} = \mathrm{span}\{\mathbf{e}_{x1}, \mathbf{e}_{y1}, \mathbf{e}_{z1}, \mathbf{e}_{1z}, \mathbf{e}_{1z}, \mathbf{e}_{1z}\}$$

$$\mathfrak{m} = \mathrm{span}\{\mathbf{e}_{xx}, \mathbf{e}_{xy}, \mathbf{e}_{xz}, \mathbf{e}_{yx}, \mathbf{e}_{yy}, \mathbf{e}_{yz}, \mathbf{e}_{zx}, \mathbf{e}_{zy}, \mathbf{e}_{zz}\}.$$

Since $[\mathfrak{k}, \mathfrak{k}] \subseteq \mathfrak{k}$, $[\mathfrak{m}, \mathfrak{k}] = \mathfrak{m}$, and $[\mathfrak{m}, \mathfrak{m}] \subseteq \mathfrak{k}$ the decomposition $\mathfrak{su}(4) = \mathfrak{k} \oplus \mathfrak{m}$ is a Cartan decomposition (see section 2.2.4.3 for details). The subspace $\mathfrak{k} = \mathfrak{su}(2) \oplus \mathfrak{su}(2)$ corresponds to Hamiltonians which generate single-qubit rotations on either qubit, while $\mathfrak{m}$ corresponds to Hamiltonians which produce entanglement between the paired qubits. Our interest is

in the abelian subalgebra $\mathfrak{a} = \text{span}\{\mathbf{e}_{xx}, \mathbf{e}_{yy}, \mathbf{e}_{zz}\}$, $\mathfrak{a} \subset \mathfrak{m}$ which corresponds to spin-spin coupling interactions. In ion-traps these effective interactions are generated by two-qubit gates such as the Mølmer-Sørensen gate or the phase gate [105, 140].

This admits a KAK decomposition $U = K_2AK_1$ for any $U \in SU(4)$, where the $K_j \in SU(2) \otimes SU(2)$ are formed from independent single-qubit rotations and $A \in \mathrm{e}^{\mathfrak{a}}$ are propagators generated by spin-spin interactions. The KAK form serves as a framework for a pulse sequence to generate any arbitrary two-qubit rotation. Furthermore, if K_2, A, and K_1 are each implemented by a compensating sequence then their product will also be a compensating sequence.

7.2 Two qubits and multiple errors

Jones extended B2 to two-qubit gates in NMR quantum computers [141], where the natural two-qubit Hamiltonian is H_{zz}. We consider Mølmer-Sørensen type interactions where the effective Hamiltonian is H_{yy} or H_{xx}, depending on the laser phase. Ultimately the distinction is unimportant since both choices yield equivalent algebras. Jones uses the KAK construction

$$R_{1,2}(\theta, \phi) = R_1(\phi, 0) \exp(-\mathrm{i}\theta H_{yy}) R_1^\dagger(\phi, 0), \tag{7.2}$$

where $R_1(\phi, 0)$ is a single-qubit rotation on the first qubit. Since $R_1(\phi, 0) H_{yy} R_1^\dagger(\phi, 0) = \cos\phi H_{yy} + \sin\phi H_{zy}$, the generator for the rotation $R_{1,2}(\theta, \phi)$ belongs to the subalgebra $\mathfrak{j} = \text{span}\{\mathbf{e}_{yy}, \mathbf{e}_{zy}, -\mathbf{e}_{x1}\}$, which is a representation of $\mathfrak{su}(2)$. Alternatively one could instead choose to implement single-qubit rotations on the second qubit, e.g. $R_2(\phi, 0)$, to yield generators in the algebra $\mathfrak{j}' = \text{span}\{\mathbf{e}_{yy}, \mathbf{e}_{yz}, -\mathbf{e}_{1x}\}$. It is unimportant which representation of $\mathfrak{su}(2)$ is used, only that the choice remains constant throughout the duration of the sequence.

Suppose the system is subjected to a systematic spin-spin coupling error, see section 4.3.2.1 for details. If the systematic error is related to the Lamb-Dicke parameters, then only the two-qubit interaction is affected and the propagator (7.2) is replaced with $R_{1,2}(\theta(1 + \epsilon_{yy}), \phi)$. However if the error is related to the laser amplitude, single-qubit rotations are also likely to experience a systematic error since both operations use the same

laser. In this case the replacements $R_1(\phi(1+\epsilon_x),0)$ and $R_{1,2}(\theta(1+\epsilon_{yy}),\phi(1+\epsilon_x))$ are used. We treat ϵ_x and ϵ_{yy} as unknown error parameters, however in the case of pure laser amplitude errors they are related by $(1+\epsilon_x)^2 = 1+\epsilon_{yy}$.

7.2.1 B2-J

Jones' extension of the B2 sequence, which we call B2-J, assumes perfect single-qubit rotations (e.g., $\epsilon_x = 0$). The sequence is constructed of four two-qubit rotations generated by the vectors

$$\mathbf{r}_1 = \vartheta \mathbf{e}_{yy}$$

$$\mathbf{r}_2 = \pi \cos\phi_{B2-J}\mathbf{e}_{yy} + \pi \sin\phi_{B2-J}\mathbf{e}_{zy}$$

$$\mathbf{r}_3 = 2\pi \cos(3\phi_{B2-J})\mathbf{e}_{yy} + 2\pi \sin(3\phi_{B2-J})\mathbf{e}_{zy}$$

$$\mathbf{r}_4 = \pi \cos\phi_{B2-J}\mathbf{e}_{yy} + \pi \sin\phi_{B2-J}\mathbf{e}_{zy}.$$

The phase $\cos\phi_{B2-J} = -\frac{\vartheta}{4\pi}$ is identical to B2. There is a one-to-one correspondence between the generators of B2-J and B2. Written as a sequence of two-qubit rotations, $U_{B2-J} = R_{1,2}(\pi,\phi_{B2-J})R_{1,2}(2\pi,3\phi_{B2-J})R_{1,2}(\pi,\phi_{B2-J})R_{1,2}(\vartheta,0)$. In the presence of unknown spin-spin errors, $U_{B2-J} = R_{1,2}(\vartheta,0) + O(\epsilon_{yy}^3)$ so long as $\epsilon_x = 0$, and the infidelity scales as $O(\epsilon_{yy}^6)$ when ϵ_x is small and as $O(\epsilon_x^2\epsilon_{yy}^2)$ when ϵ_{yy} is small [142]. As long as the single-qubit error is zero, in principle we can apply $R_{1,2}(\vartheta,0) + O(\epsilon_{yy}^{n+1})$ to arbitrary accuracy by replacing the B2 scaffold with higher order sequences, for example Bn [114]. Bn-J sequences therefore implement arbitrarily accurate gates, provided there exists two non-commuting controls, one of which is free of error. These sequences are distinguished by the use of effective rotations constructed by KAK-style pulses.

7.2.2 B2-WJ

More realistic models consider both single-qubit and two-qubit errors. One problem with Bn-J is the accuracy advantage reduces when $\epsilon_x > \epsilon_{yy}^{n+1}$. This may be improved by modifying (7.2) by replacing $R_1(\phi,0)$ with a compensating sequence that corrects single-qubit errors. Bn sequences provide arbitrarily accurate gates, provided there exists two non-commuting controls with proportional errors [142]. In the case of single qubit rotations the

errors corresponding to H_{x1} and H_{y1} are usually correlated since physically these interactions are only distinguished by a relative phase with respect to the laser field.

The sequence B2-WJ is

$$U_{B2-WJ} = W_{1,2}(\pi, \phi_{B2-WJ})W_{1,2}(2\pi, 3\phi_{B2-WJ})W_{1,2}(\pi, \phi_{B2-WJ})W_{1,2}(\vartheta, 0) \tag{7.3}$$

where $W_{1,2}(\theta, \phi) = U_{B2}(\phi, 0)\exp(-\theta H_{yy})U_{B2}^{\dagger}(\phi, 0)$ is analogous to (7.2) with now the single-qubit rotations $R_1(\theta, \phi)$ replaced by a corresponding B2 sequence. Similar to before $\cos\phi_{B2-WJ} = -\frac{\vartheta}{4\pi}$. B2-WJ may be thought of as a concatenated compensating pulse sequence. The lower layer of concatenation consists of B2 pulses which take two correlated error single-qubit controls to synthesize an compensated single-qubit control. The higher layer of concatenation is a B2-J sequence which corrects the two-qubit coupling using compensated one-qubit controls. In the presence of unknown systematic errors, $U_{B2-WJ} = R_{1,2}(\vartheta, 0) + O(\alpha\epsilon_{yy}^3 + \beta\epsilon_x^3)$ and the infidelity scales as $O((\alpha\epsilon_{yy}^3 + \beta\epsilon_{yy}\epsilon_x^3)^2)$, where α and β are constants that depend on ϑ and the control Hamiltonians.

For B2-WJ the infidelity at small ϵ_{yy} for fixed ϵ_x scales as $O(\epsilon_{yy}^2)$. This is the same order as the uncorrected pulse $R_{1,2}(\vartheta(1 + \epsilon_y y), 0)$, although with a substantially smaller infidelity. In the case of $\epsilon_x = 0.01$, the infidelity in this regime is a factor of 10^8 smaller than the uncorrected pulse (see Figure 7.1). For B2-WJ, the infidelity scales as $O(\epsilon_{yy}^2)$ when $\epsilon_{yy} < \frac{\beta^2}{\alpha^2}\epsilon_x^{3/2}$. However, we can replace the B2 sequences in $W_{1,2}$ with higher order pulse sequences, for example the Bn sequences. In this case, the infidelity will scale as $O((\alpha\epsilon_{yy}^3 + \gamma_n\epsilon_{yy}\epsilon_x^{(n+1)})^2)$, where γ_n is a constant that depends on ϑ and Bn. As a result, the value of ϵ_{yy} where the scaling changes from ϵ_{yy}^6 to ϵ_x^2 becomes smaller and smaller. In Figure 7.1, we compare the scaling properties of the B2-WJ and the higher order B2-$\tilde{\text{W}}$J where we have replaced the $W_{1,2}$ B2 sequence with the B4 sequence [114, 143]. As expected, the error ϵ_{yy} where the scaling changes from ϵ_{yy}^6 to ϵ_{yy}^2 changes from $\simeq 10^{-2}$ for B2-WJ to $\simeq 10^{-4}$ for B2-$\tilde{\text{W}}$J. In principle, given a target infidelity and systematic errors $\epsilon < 1$ [114], we can construct a pulse sequence with an infidelity guaranteed below the target infidelity. We note that in practice other errors including random control errors and decoherence typically limit the fidelity.

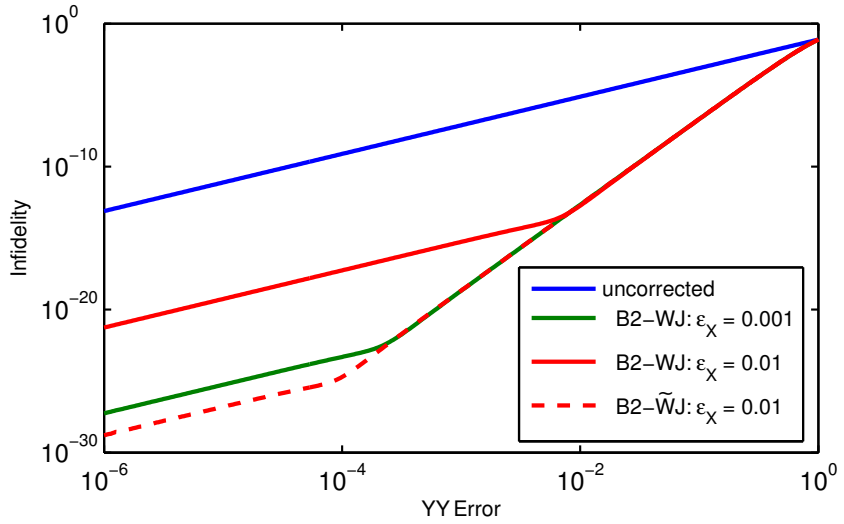

Figure 7.1: Comparison of B2-WJ and the higher order B2-W̃J pulse sequences applied to a $\exp(-\mathrm{i}\frac{\pi}{4}H_{yy})$ operation. For a fixed H_{x1} and H_{y1} error ϵ_x, the infidelity after a B2-WJ correction scales as $O((\alpha\epsilon_{yy}^3 + \beta\epsilon_{yy}\epsilon_x^3)^2)$ (see text). For the same ϵ_x the B2-W̃J sequence scales as $O((\alpha\epsilon_{yy}^3 + \gamma_4\epsilon_{yy}\epsilon_x^5)^2)$, extending the regime where the infidelity scales as $O(\epsilon_{yy}^6)$.

In Figure 7.2, we compare the ideal unitary $U_T = \exp(-i\frac{\pi}{4}H_{yy})$ to the composite sequences assuming errors equivalent errors in H_{x1}, H_{y1} and uncorrelated errors in H_{yy}. B2-J outperforms B2 when either error is low. B2 is preferable when the systematic errors are identical. B2-WJ results in low errors over the range of two errors. Initial compensation of the H_{x1} pulses results in better compensation of H_{yy}.

7.3 Extension to many qubits

Given a control operator with a systematic error and a perfect rotation that transforms that operator to an orthogonal independent operator, we can perform compensation, e.g. B2-J. Given two control operators with correlated errors that are generators of su(2), we can perform compensation, e.g. B2. As a result, in principle one can perform arbitrarily accurate composite pulses on a controllable quantum system where all the controls have independent errors except two.

As an example, imagine n qubits in a row with single qubit operators and pairwise Mølmer-Sorensen couplings. The Hamiltonians are X_j, Y_j on each qubit and Y_jY_{j+1} between neighbors. If for the qubit n, X_n and Y_n have uncorrelated error, there does not exist a

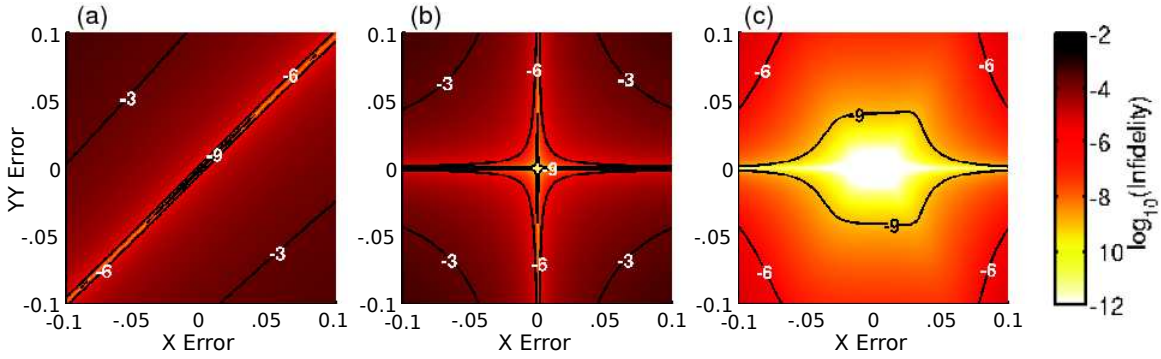

Figure 7.2: Comparison of (a) B2, (b) B2-J, and (c) B2-WJ pulse sequences applied on $\exp(-\frac{i\pi}{4}H_{yy})$ operation on a pair of qubits. B2-WJ assumes H_{x1} and H_{y1} have equivalent systematic errors.

compensation pulse [136]. However, if the X and Y systematic errors are correlated on the the first qubit but otherwise independent, the following sequence can be used to generate an arbitrarily accurate X rotation on the nth qubit.

For the initial qubit with correlated X_1 and Y_1 errors, B2 is used. To correct Y_1Y_2, B2-J is used with B2 corrected X_1 pulses. This is the sequence B2-WJ. X_2 on the second qubit is then corrected via B2-J using B2-WJ corrected Y_1Y_2 pulses. We denote this sequence as B2-WJJ or B2-WJ^2. Errors on the nth qubit can be compensated by repeated use of B2-J along the chain, first correcting X_j, then Y_jY_{j+1} and then X_{j+1} until X_n is reached. The total sequence correcting the nth X rotation is denoted B2-WJ$^{2(n-1)}$.

Figure 7.3 compares correcting a $\pi/4$ X rotation as a function of chain length assuming equal magnitude errors for all operators but with a random sign except for X_1 and Y_1. The correlated and anti-correlated lines serve as references. If X_n and Y_n have correlated errors, then local B2-W greatly reduces the infidelity. In the worst case scenario, the errors are anticorrelated and the compensation pulses add additional error to the initial overrotation. X_n rotations can still be corrected using B2-WJ$^{2(n-1)}$, if only X_1 and Y_1 are correlated. The error increases with position (comparing B2-WJ^2 to B2-WJ^{10}) on the chain for large errors but approaches an equivalent fidelity for small errors. Asymptotically, the correction of X_n rotations by sequential correction (B2-WJ$^{2(n-1)}$) is equivalent to the B2-W correction

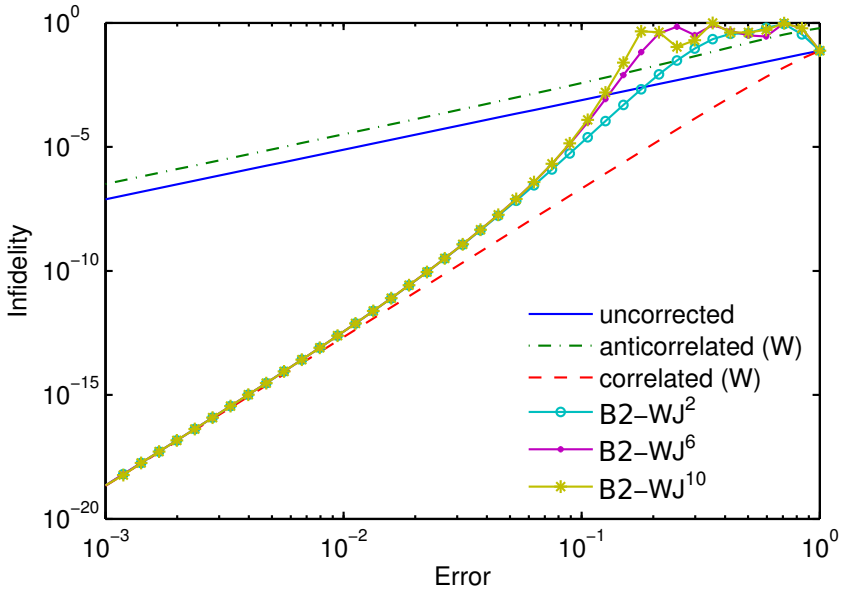

Figure 7.3: Compensation of $\exp(-\frac{i\pi}{8}X_n)$ by application of B2-WJ$^{2(n-1)}$. Compensation by B2-W pulses using Y_n works only when the errors are correlated. Anticorrelated errors between X_n and Y_n increase the infidelity. B2-WJ$^{2(n-1)}$ uses the correlated errors of X_1 and Y_1 and a chain of Y_jY_{j+1} interactions to compensate the X_n rotation. The results for X_2, X_4 and X_6 are shown.

composed of correlated X_n and Y_n rotations. Replacing B2 with the pulse sequences from [114] allows for the creation of arbitrarily accurate pulse sequences.

Although, this is not practical on a large scale, it can lead to a constant reduction in the number of gates that need to be calibrated at the beginning of an experiment for a large quantum system. Per region of computation, only a few highly reliable quantum gates can be used to reduce systematic errors in their neighbors.

7.4 Summary

We have shown that arbitrarily accurate compensation is possible with a fully controllable system if either two non-commuting Hamiltonians that generate $\mathfrak{su}(2)$ have equivalent systematic errors or if a single Hamiltonian is error free. The underlying pulse sequences are equivalent to sequences for single qubits. We can generate arbitrarily accurate two-qubit gates using B2-J type sequences. These can interact with their neighbors, etc. This is impractical but it does suggest that a system with a few low-error controls could efficiently compensate neighboring high-error control.

The $\mathfrak{su}(2)$ algebra underlying these compensating pulse provides additional incentive to continue development of single qubit compensation pulses. Shaped pulse sequences or continuous time control can lead to further improvements [144]. The question remains how to develop composite pulses that do not rely on a $\mathfrak{su}(2)$ or $\mathfrak{so}(3)$ subalgebra. The development of compensation pulses that do not use the geometry of the sphere and the development of techniques for identifying compensation compatible systems are both interesting challenges.

CHAPTER VIII

INTEGRATED MICROMIRRORS FOR RAPID DETECTION

Ion qubit state-detection relies on efficient collection of laser-induced ion fluorescence [91, 145–147]. Measurement times for high-fidelity readout are set by the collection efficiency, frequently limited by a small light collection solid-angle. In large arrays of cotrapped ions, it will be necessary to detect the states of multiple ions simultaneously in order to keep operation times low. However with most light collection optics, increasing the collection efficiency from a single ion restricts the field of view (FOV), limiting the ability to perform parallel measurements over many ions.

This chapter examines a multi-scale fluorescence collection system where high numerical aperture (NA) micromirrors are coupled to a macroscopic, low NA lens for efficient light collection over a large FOV [133]. An array of these mirrors could be integrated into a large trap, permitting simultaneous collection of light from many ions. Towards this end, we developed a microfabricated surface-electrode ion trap with an integrated micromirror. The chapter is organized as follows: Section 8.1 describes the design of the microfabricated mirror trap and optics. Section 8.2 describes the trap architecture and fabrication procedure. Section 8.3 presents measurements of the collection enhancement of a trapped atomic ion over the mirror. Section 8.4 concludes with proposed improvements and potential applications.

8.1 Trap and optics design

The design consists of a five-wire surface-electrode Paul trap with an integrated reflective mirror component for improved photon collection (see figure 8.1). Similar to our other traps, a radio-frequency RF potential applied to a pair of rail electrodes confines the ions radially. Axial confinement is achieved by biasing a subset of 42 independent DC control electrodes which lie adjacent to the RF rails. Typical trapping potentials utilize five electrodes per side to generate harmonic wells with secular frequencies between 0.5 and 2 MHz. As before,

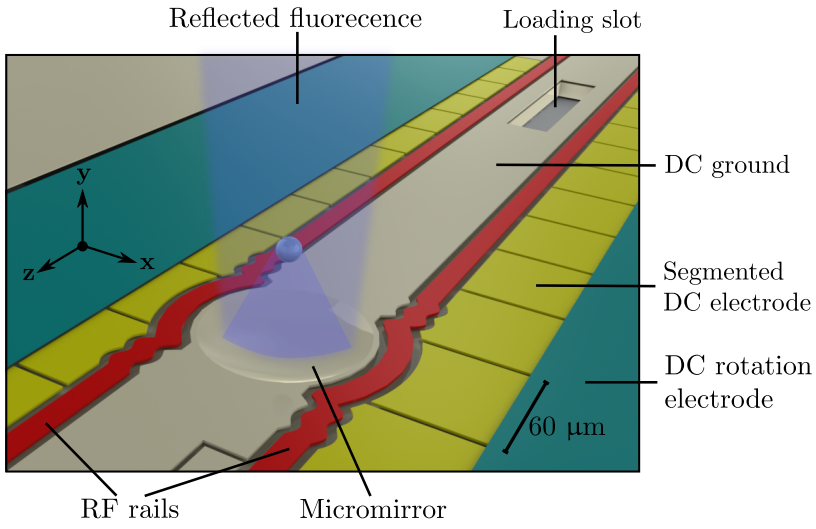

Figure 8.1: Trap layout showing the integrated miromirror, RF rails, and the DC control electrodes. Scattered fluorescent photons from a trapped $^{40}Ca^{+}$ ion are collected by a relay optic and detected by a CCD camera and a PMT. The micromirror improves collection efficiency by locally increasing the collection solid-angle.

by slowly varying the potentials applied to the control electrodes, a trapped ion can be smoothly transported to distinct regions of the device, including to regions that contain specialized structures for efficient state readout.

An approximately spherical micromirror directly incorporated into the central DC ground electrode reflects a large NA cone of fluorescence from a trapped ion near the focus. Any mirror misalignment or deviation from an ideal profile results in a divergent cone of light. The alignment of the optical focus and the ion is entirely the product of design and microfabrication of the trap and is not sensitive to thermo-mechanical misalignment. We place a macroscopic relay optic outside the vacuum chamber to collect and focus fluorescent light onto a detector. In this role, rather than imaging the ion, the relay lens images the micromirror onto the detector. As such, the relay lens spot size is only required to match the selected detector size, making it simple to design and assemble. The relay optics are designed to be tolerant of misshaped and misaligned micromirrors. Furthermore, this multi-scale light collection system can direct light from a multitude of micromirrors distributed across a large FOV to independent detectors.

8.1.1 Designing traps for micromirror integration

For compatibility with VLSI fabrication techniques [87], we consider only designs in which no electrode edges are patterned inside the micromirror and where the electrode forming the mirror surface is grounded. We estimate the solid-angle coverage provided by the mirror and its dependence on the electrode configuration by examining two analytic models in the gapless plane electrostatic approximation [86]: a ring trap geometry which enables a high collection efficiency of reflected photons and a linear-strip electrode geometry compatible with ion shuttling. These models represent the design extremes; features of both designs are combined in a hybridized wrapped-electrode geometry which is numerically optimized to minimize the influence of the mirror on the pseudopotential tube.

8.1.1.1 Ring trap geometry

Consider a trap geometry where the mirror is surrounded by a narrow RF ring electrode. Neglecting the depression of the mirror cavity (mirror sag), we use the gapless plane electrostatic approximation to calculate the inner radius of the RF rail r (equal to half the mirror diameter) as a function of the ion height h above the trap surface

$$r = h\left[\frac{3}{4}\sin^{-2}\left(\frac{\pi}{6}+\theta\right)-1\right]^{1/2},\ 0<\theta<\pi/6, \tag{8.1}$$

where θ is proportional to the angular width of the RF electrode as seen from the ion (see [86]). We immediately note that the collection angle $\varphi = \arctan(r/h)$ does not depend on the mirror shape or size. The upper bound ($\theta = 0°$, corresponding to an RF electrode with an infinitesimal width) gives $\varphi = 54.7°$ (NA = 0.82, 21% geometric collection efficiency). For a reasonable but small rail angle, $\theta = 16°$, $\varphi = 50°$ (NA = 0.76, 18% geometric collection efficiency). These analytic results neglect the effect of the micromirror depression on the fields. The influence of the micromirror on the trapping fields will lower the ion height and is therefore expected to somewhat improve the collection efficiency. Moving any portion of the RF rails away from the mirror will raise the ion height, therefore the insertion of small isolation gaps between electrodes as required for real traps will reduce collection efficiency.

8.1.1.2 Linear trap geometry

While the maximum collection efficiency is achieved with a surface ring trap, we require a mirror compatible with a scalable architecture that allows for the shuttling of ions. Figure 8.2a shows an example of such an architecture in which the mirror is tangent to the RF rails of a linear section. In this design, any ion in the linear section may be transported over the mirror for readout. Once again using the gapless plane electrostatic approximation, we find the relationship between the ion height and mirror radius for this configuration,

$$r = h \tan(\pi/4 - \theta). \tag{8.2}$$

Again, r/h is a function only of the RF electrode angle, and the radius of curvature (ROC) of the mirror is linearly proportional to the ion height. The upper bound for the mirror acceptance angle, $\varphi = 45°$, is again found when $\theta = 0°$ (NA = 0.71, 15% collection efficiency). For a reasonable rail angle, $\theta = 4°$, $\varphi = 41°$ (NA = 0.66, 12% geometric collection efficiency).

8.1.1.3 Hybrid trap geometry

Figure 8.2b shows a concept for a hybrid of the two analytic models that improves the collection efficiency by wrapping the RF rail around the mirror. We choose a conservative design, with a target ion height of 63 μm, $\theta = 16°$, and a 45° wrapping of the RF rail around the mirror. Approximate values of the mirror ROC (150 μm) and radius (60 μm) were found from the above analytic forms after including a 6 μm gap around the edge of the RF electrodes and a 4 μm flat shelf around the edge of the mirror. The resulting optimal micromirror sag is 12 μm and the NA is 0.69 (geometric collection efficiency 14%). These parameters represent an idealized target geometry for fabricated micromirrors. Errors in microtrap fabrication may lead to significant deviations in the mirror profile.

We performed numerical simulations on these candidate designs using our own method-of-moments electrostatics code. Similar methods were used to optimize trapping electrode geometries. Starting with the design in figure 8.2b, the RF rail width was adjusted until the mirror focus was aligned with the pseudopotential null (17 μm rail width) while keeping the

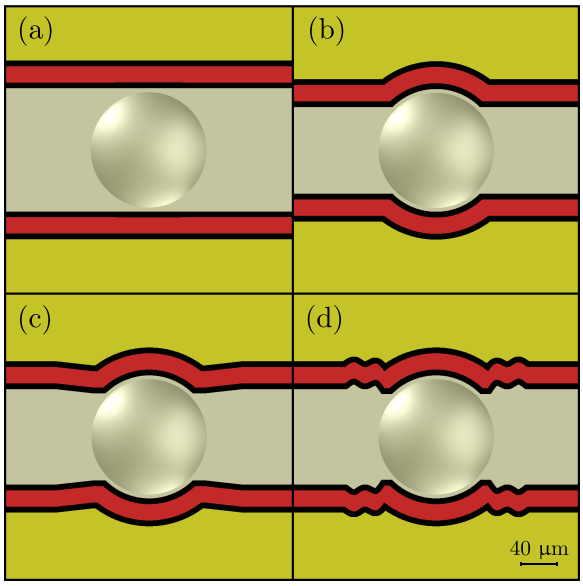

Figure 8.2: Illustration of the geometry of the trap and micromirror for various design iterations. (a) a trap with linear RF rails tangent to the mirror, (b) RF rails wrapped around the mirror, (c) RF rails with a pinch and taper to a linear section, (d) the final geometry with genetic algorithm optimized RF electrodes.

inner edge of the rail and mirror profile constant. Next, the spacing between the RF rails in the linear section was optimized so that the ion height over the linear section approximately matched the height in the mirror. A pinch in the RF electrodes was inserted at the transition region between the linear and wrapped rail geometries (figure 8.2c) to reduce variation in the ion height. This adjustment did not change the location of the RF null over the mirror.

Finally, a genetic algorithm was used to optimize the RF rail geometry near the wrapping region. The algorithm uses a fitness function that minimizes the RF-noise motional heating rate [31] while maintaining a nearly uniform ion height down the linear section. The fitness function is proportional to $\int_C [\partial E^2(z)/\partial z]^2 dz$, where $E(z)$ is the applied electric field and the contour C follows the pseudopontential minimum along the axial coordinate z. Perturbations to the rail geometry are parametrized by a set of edge points which are systematically displaced from the input geometry. A spline function was used to interpolate the RF rail edge between these points. The optimizer was allowed to adjust the number of points and the distance of the points from the axial center line of the trap, under the constraint that the width of the RF rail was held constant and the RF null location was

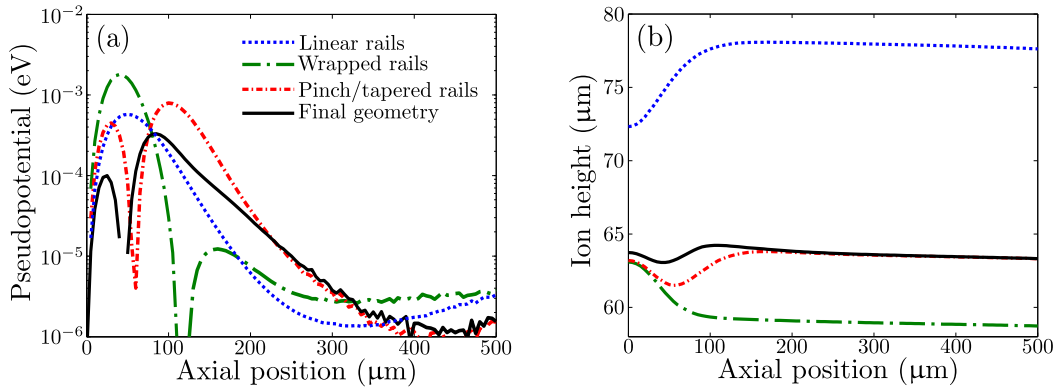

Figure 8.3: Figures of merit for various design iterations. (a) Residual pseudopotential at the minimum in the transverse plane as a function of axial displacement from the mirror center for various design iterations. The residual pseudopotential vanishes at points where the confining fields cancel. (b) Height of the calculated pseudopotential minimum as a function of position along the trap axis. Far from the mirror, the pseudopotential height asymptotically approaches a limiting value controlled by the RF rail spacing in the linear region.

maintained within 0.25 μm of the mirror focus. The resulting optimization produced several candidate solutions. The solution with the fastest decline in the RF field along the trap axis was selected for fabrication. This design is shown in figure 8.2d.

8.1.2 Design of relay optics for scalable state detection

An important component of the multi-scale detection system is the macroscopic relay lens assembly. In a proposed trap design with an array of mirrors, the relay lens directs light reflected from each micromirror site located to an independent sensor (e.g., a single element in a PMT or APD array) in the image plane, allowing independent, asynchronous readout for each mirror (see figure 8.4). The required complexity of the relay optic depends on the mirror spacing in the ion trap and the required insensitivity of the system to misalignment.

To illustrate the simplicity and robustness of this approach, a 1:1, NA = 0.14 relay lens was designed using 2" diameter stock plano-convex lenses in a commercial optics simulation package (Zemax ®). In the simulations, a spherical mirror matching the ideal target geometry is placed at the object point of the relay optic. The optic is designed so that light collected from each measurement region is focused onto independent 0.25 mm radius

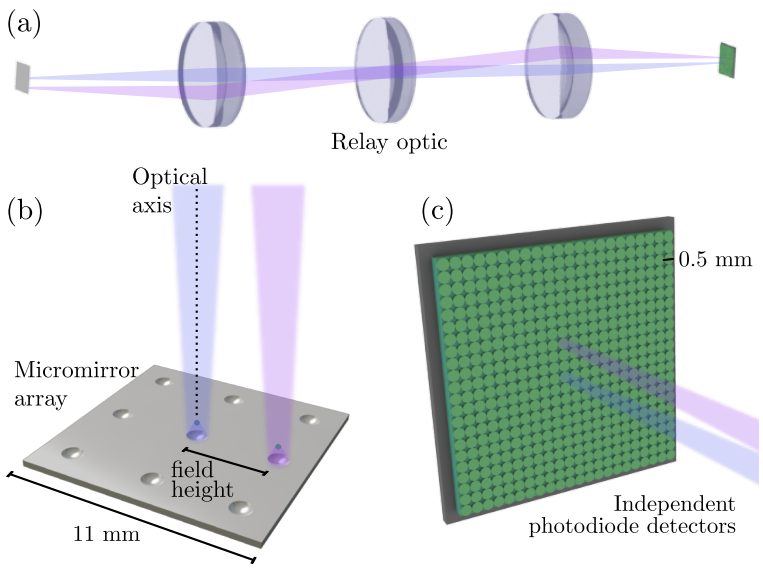

Figure 8.4: (a) Diagram of a multi-scale light collection system for a proposed trap with an array of mirrors. Collected fluorescence from each individual micromirror (b) is relayed to an independent detector (c). The relay lens assembly can image mirrors over the entire 11×11 mm^2 trap chip with minimal cross-talk between detectors. For clarity, the trap electrodes have not been drawn and only a small number of mirrors were included. The micromirrors are not drawn to scale.

detectors in the image plane. Individual micromirrors distributed anywhere on the 11×11 mm^2 chip are resolvable with zero cross-talk so long as no two mirrors are placed closer than 0.5 mm center-to-center. This distance corresponds to six DC control electrode widths in the current trap (see figure 8.1b).

To estimate the tolerance of the light collection system under various misalignments, we calculate the distribution of directly emitted and specularly reflected rays projected onto the detector plane. We consider transverse displacements of the micromirror from the optical axis of the relay lens (field height). In figure 8.5a, we show that for mirror displacements exceeding the dimensions of the trap chip the light specularly reflected by the micromirror forms a localized spot less than 0.25 mm in radius in the image plane (the lens does not vignette any light reflected from the mirror). The image plane is assumed to be distortion free. That is, if the mirror is placed 8 mm from the axis of the relay lens, the detector is placed 8 mm from the axis in the opposite direction.

Photons directly emitted by the ion are not well collimated and may arrive at one of

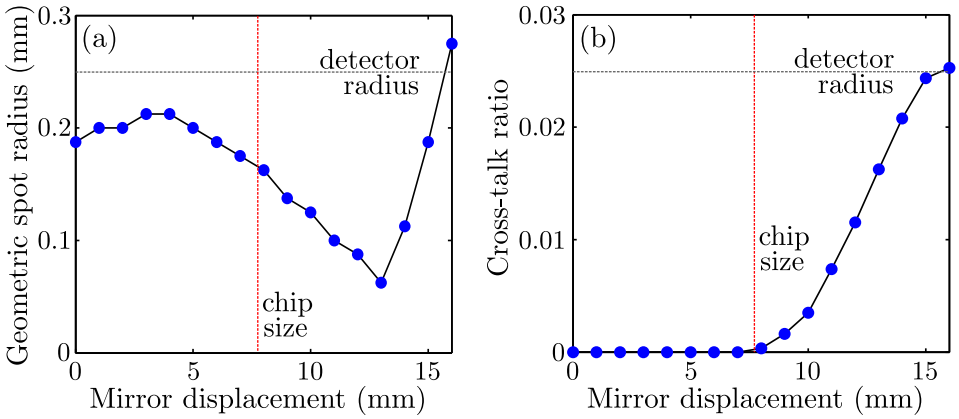

Figure 8.5: (a) Simulated geometric spot radii of the ray bundle specularly reflected from a spherical micromirror for transverse displacements of the mirror from the relay optic axis (field height). Guides illustrating the detector radius and maximum field height set by the chip dimensions ($\sqrt{2} \times 11/2$ mm) are provided. (b) Cross-talk ratio (fraction of collected light that reaches the image plane outside of the detector radius) versus mirror displacement from the relay optic axis. The ratio is an upper bound on the cross-talk; in practice the actual cross talk will be smaller. The calculation includes rays directly emitted by the ion and assumes 85% mirror reflectivity with negligible transmission losses.

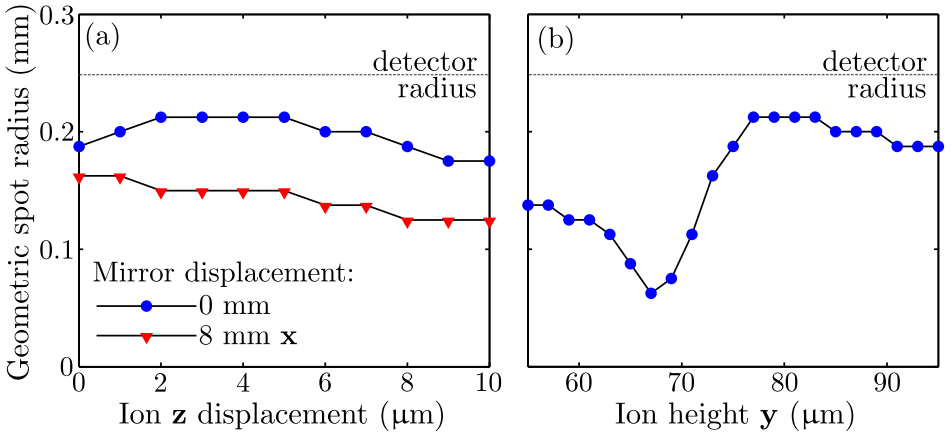

Figure 8.6: (a) Simulated specularly reflected spot radii for ion displacements along the trap axis z from a mirror center. The reflected ray distribution is calculated for mirrors at field heights 0 mm and 8 mm. The position of the detector is not adjusted to compensate for misalignment of the ion to the mirror. (b) Spot radii for vertical ion displacements along the y axis from the vertex of a mirror located on the relay lens axis.

several detectors, introducing a cross-talk error during state detection. The relay optics have been designed to reduce this effect. Figure 8.5b shows that for all transverse mirror displacements within the chip dimensions, light from an individual ion relayed by the lens may be collected by a single 0.25 mm radius detector with a cross-talk of less than 0.05%. Therefore, the designed multi-scale detection system is efficient for mirrors placed anywhere within the design FOV of the relay lens. Note that larger, denser arrays of micromirrors are possible as fast, high fidelity readout is still possible with non-negligible cross-talk [145].

We also consider misalignments of the ion relative to the micromirror either in the transverse x-z plane (e.g., the ion is not centered on the optical axis) or longitudinally (e.g., the mirror ROC is incorrect, the mirror sag is incorrect, or the RF rails are incorrectly sized). The magnitudes of these misalignments are bounded by the characteristic errors from trap fabrication. We conservatively estimate the transverse misalignment to be less than 4 μm and the mirror sag error to be less than 3 μm. Nondestructive measurement of the micromirror profile outside NA = 0.3 is not currently possible, leading to uncertainty in the longitudinal alignment of the mirror focus with the RF null. However, it is possible to accurately measure the sag of the mirror and post-select a chip that is closest to the design objective (within 1 μm). In figures 8.6a-b the specularly reflected spot radius is plotted as a function of transverse and longitudinal misalignment. We find that the design performance of the collection system is not degraded for misalignments within the expected fabrication tolerances. Finally, we note that increased FOV, improved misalignment tolerances, and other detector sizes and configurations may be accessible by redesign of the relay lens.

8.2 Trap architecture and fabrication

The ion trap fabrication process is based on well established silicon VLSI processing techniques which enable the production of complex scalable structures. The traps are fabricated on the surface of a ⟨100⟩ p-doped Si substrate and use sputtered Al electrodes with PECVD SiO_2 dielectric layers. Architecturally the device is similar to traps reported in [32, 34, 87] with several important design improvements, including integrated capacitive filters ($\sim$ 60

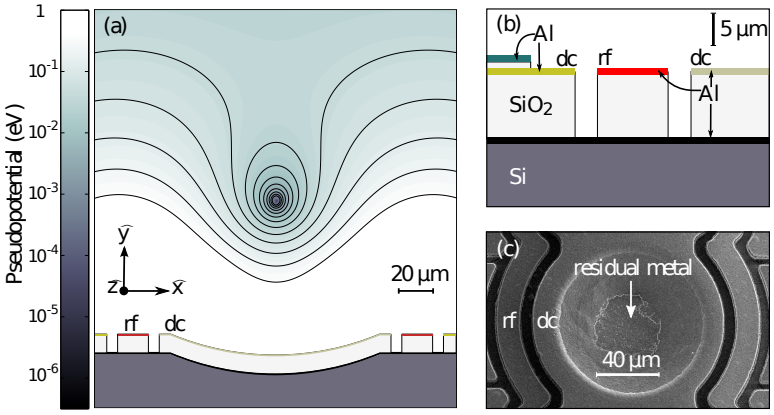

Figure 8.7: (a) Trap cross section along the x radial direction at the center of the mirror. A logarithmic plot of the pseudopotential including equipotential lines is superimposed. (b) Detail of trap fabrication on a silicon substrate. For clarity, only features in the vertical direction are drawn to scale. The trapping electrodes are isolated from the Si substrate by a 1 µm Al ground plane and 10 µm of insulating SiO_2. Two additional patterned metal layers separated by 1 µm SiO_2 define the trapping electrodes (2nd level) and the integrated capacitive filters (3rd level). (c) SEM image of the mirror on the prototype trap used in the experiment. A lithography error in the final metal patterning step left 1 µm of residual aluminum from the capacitor layer in the center of the mirror.

pF) to reduce RF pickup on the DC electrodes and asymmetric DC electrodes to simplify rotation of the secular axis for effective laser cooling. The design also features a through-chip loading slot.

Fabrication begins by defining the mirror profile in the silicon substrate. The process for producing recessed micromirrors in silicon uses an HF, HNO_3 and acetic acid (HNA) solution to etch isotropically through circular apertures patterned on a LPCVD silicon nitride mask [148–150]. The wafer is etched in a room temperature HNA bath without agitation for 22 minutes after which the nitride mask is removed in HF. The overall etch rate and final surface morphology are highly dependent on the concentrations of each of the etchant components and must be carefully optimized to provide a smooth, controllable etch [151]. We have selected a 1 HF : 8 HNO_3 : 1 CH_3COOH (by vol.) solution for an etch with an anisotropy of $\sim 10\%$ [152] and a low occurrence of surface defects. We find that the mirror diameter and radius of curvature can be controlled to within ± 2 µm by choosing the appropriate circular aperture size and HNA etch time. Following wet processing, the frontside of the wafer is thinned using a combination of lapping and chemical mechanical

polishing techniques to independently control the mirror sag. The mirror surface is protected during thinning with a sacrificial 15 μm SiO_2 layer.

Following mirror fabrication, the trapping electrode structures are patterned over the polished substrate. The spherical mirror profile is translated to the surface electrodes during build-up. A cross-section of the device is shown in figure 8.7b. To prevent coupling of the trapping electrodes to the lossy Si substrate, a 1 μm Al ground plane and a thick 10 μm SiO_2 dielectric layer are deposited over the substrate. RF and DC electrodes are lithographically patterned and plasma etched from a 1 μm Al film deposited above the insulating oxide surface. This layer of aluminum also serves as the mirror coating; the mirror surface itself is part of the central DC electrode. A final pair of 1 μm thick SiO_2 and aluminum layers are patterned to form on-chip capacitive filters for grounding RF potentials on the control electrodes. Isolation trenches separating the trapping electrodes are formed with a plasma etch which removes exposed SiO_2 between the electrode structures. The removal of excess oxide from the trap surface also reduces sites where stray charges may accumulate and perturb the trapping potential [153, 154]. An ICP Bosch process [155] is used to etch the loading slot through the substrate, resulting in a nearly vertical etch profile.

An SEM image of the micromirror in the prototype device used in this study is shown in figure 8.7c. During fabrication, a lithography error resulted in the incomplete removal of the final metal level in the center of the mirror. The presence of this rough ($\sigma_{RMS} > 40$ nm, measured by a Veeco Dimension 3100 AFM in tapping mode) residual metal is expected to severely degrade the optical performance of the device. Among the batch of roughened mirrors, we selected traps for testing by the mirror surface finish rather than the geometry of the mirror profile. For the trap tested in this study, the mirror geometry (ROC = 178 μm, $r = 50.5$ μm, NA = 0.63) differs substantially from the ideal profile. Despite the poor quality of the mirror, the device was still able to demonstrate significant photon collection improvement (factor of 1.9 enhancement). We expect to demonstrate larger collection enhancements as our fabrication processes are improved.

8.3 Trapping and demonstration of collection enhancement

The integrated mirror structure is characterized with single ions of $^{40}Ca^{+}$ fluorescing on the 397 nm $^{2}S_{1/2} \rightarrow {}^{2}P_{1/2}$ cycling transition. An additional optical repumping laser at 866 nm is used to prevent population trapping in the metastable $3^{2}D_{3/2}$ manifold [55, 156]. Ions are loaded into the trap 600 μm from the mirror by photoionization of neutral ^{40}Ca flux entering through the backside loading slot, preventing the deposition of metallic calcium over the trap surface. Stray photoelectrons may charge exposed insulators inside the vacuum chamber, affecting trapping potentials. A mesh ground plane 4 mm above the trap surface shields ions from stray fields while allowing the transmission ($T \geq 80$ %) of fluorescent photons. The RF trapping potential ($V_0 \approx 200$ V, $\Omega_{\mathrm{rf}} = 2\pi \times 62.3$ MHz) is applied by a waveform generator filtered by a helical resonator. Radial and axial mode frequencies were measured to be $2\pi\times$(2.9, 2.2, 1.0) MHz.

Ion shuttling is achieved by applying a set of slowly varying transport potentials ($|V| \leq$ 6V) to the DC control electrodes, producing a moving pseudopotential well which may be held stationary along any axial position in the trap, see section 3.1.3.1 for details. Typical shuttling operations include 10^3 transport potential update steps and last approximately 2 ms, with a success probability $P \geq 99.98\%$. After shuttling, a computer controlled piezo driven mirror steers the 397 nm cooling beam (aligned at a 45° angle from the trap axis) to track the ion. The 866 nm beam is aligned to illuminate the entire trap axis.

In the multi-scale approach, the collection enhancement from reflected light is controlled by the micromirror, while the FOV is dependent on the relay optics. While an ideal relay optic for simultaneous readout over many distributed mirrors is described in section 8.1.2, for demonstrating collection enhancement over a single mirror, we elected to use the relay optic system already present on the apparatus (1:10, design NA = 0.43, FOV < 0.25 mm). Collected fluorescence is directed through a 45:55 beam splitter to both a Princeton Instruments Photonmax 512B EMCCD camera and a Hamamatsu H7360-02 photomultiplier tube (PMT), operating in photon counting mode. The PMT has a quantum efficiency of .205 at $\lambda = 397$ nm.

Figure 8.8 compares CCD images of ions above a planar region of the trap and over the

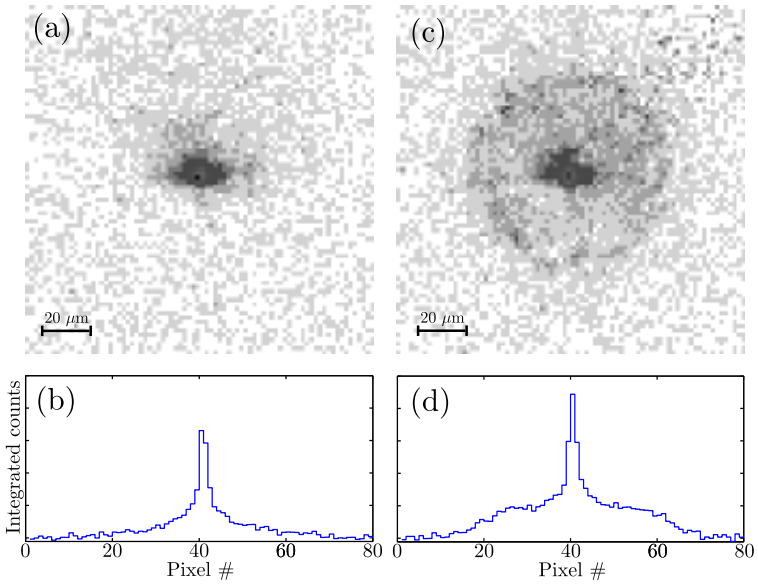

Figure 8.8: False color CCD images of ions above (a) the trap surface, and (c) the integrated micromirror. Background calibration images taken without an ion have been subtracted from the above images. (b,d) Counts from the images in (a,c) integrated across each vertical line of pixels. The sharp peaks are the direct image of the ion while the wide pedestals are produced from the light reflected from the surfaces. Each pixel is 1.6 × 1.6 μm^2 at the magnification used in the experiment.

mirror. Resonant fluorescent light directly collected from the ion appears as a well localized spot on the detector. Photons scattered from the surface of the planar region and of the mirror face form a diffuse reflected image. We observe a factor of 1.9 photon collection enhancement for an ion over the mirror compared to an ion above the planar region (see figure 8.9b). To measure the dependence of the collection enhancement on ion position, we shuttle ions across the trapping zone while monitoring the fluorescence with the PMT.

Any RF micromotion that has a component parallel to the 397 nm cycling transition beam's propagation direction will induce RF sidebands on the fluorescence profile and reduce the on-resonant fluorescence. Stray electric fields and small control potential errors can displace the ion from the micromotion minimum. To counter this effect, we measure and compensate [157] the electric field in the radial x direction required to minimize the sideband at each point in the scan. The corrections are less than 300 V/m and have a strong dependence on the ion position, likely due to a slight misalignment of the mirror to the trap axis. Though minimizing the sideband does not guarantee that the ion is on the

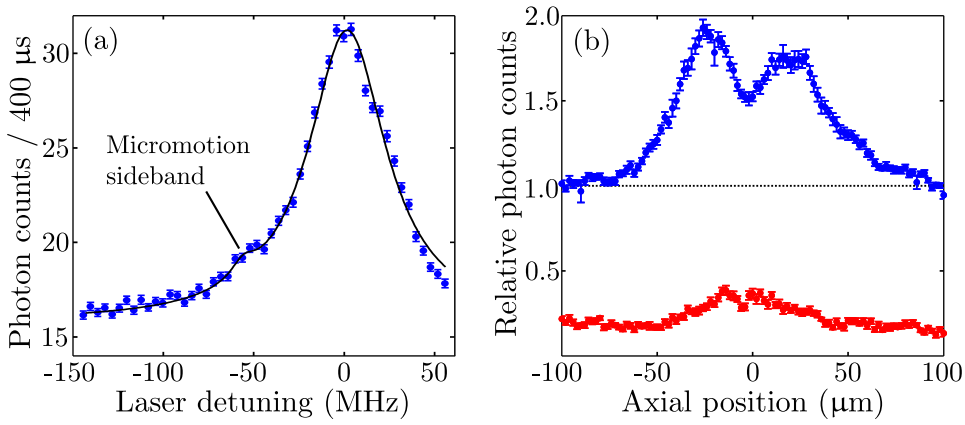

Figure 8.9: (a) Fluorescence versus frequency at the center of the mirror ($z = 0$). Static fields have been applied to minimize the RF sideband. The remaining micromotion peak is 0.06 ± 0.02 of the peak intensity. This corresponds to a micromotion modulation index $\beta = 0.3 \pm 0.1$. The smooth curve is the least squares fit of the sum of two Lorentzian functions. (b) Relative collection intensity as a function of the ion position over the mirror. The mirror is centered roughly at 0. For each position in the scan, a field in the x direction was applied to minimize the RF sideband, thus maximizing the carrier intensity.

micromotion minimum (there can be motion perpendicular to the laser), it does maximize the fluorescence. Since the 397 nm beam is at an angle of 45° with the trap axis, the remaining micromotion seen by the laser beam is an upper bound on any axial micromotion at the ion location and the resulting pseudopotential barriers. A scan of the 397 nm laser beam frequency with the compensation applied shows only a small remnant of a micromotion sideband (see figure 8.9).

Figure 8.9b shows light collection versus ion position over the mirror with the compensating field applied. The vertical scale gives the relative intensity collected by the PMT referenced to the intensity when the ion is sufficiently far from the mirror that the mirror no longer contributes, and a compensation is made for the slight dependence of the PMT collection efficiency on the ion position. This dependence is due to the PMT aperture and is determined by measuring the ion fluorescence versus position on a section of the trap far from the mirror. Fluorescence measurements on the micromotion sideband as a function of ion position (see figure 8.9b) show that the ion remains largely compensated at all the measurement locations even with the presence of the mirror. The peak light collection shows

a factor of 1.9 improvement as compared to collection without the mirror. In general, the mirror reflectance has a spatial dependence from the local topography of the aluminum film. It is postulated that the drop in collected fluorescence observed directly over the mirror is related to the rough aluminum defect at the mirror center (see section 8.2 and figure 8.7c) caused by a fabrication error. Future testing with high-quality aluminum films produced by improved fabrication techniques may clarify the role of mirror surface topography in light collection.

8.4 Summary

We have developed a surface-electrode trap with an integrated micromirror, and observed a factor of 1.9 fluorescence collection enhancement for $^{40}Ca^{+}$ ions trapped above the mirror surface. The trap design is optimized to improve the solid-angle coverage of the reflective optic under the constraints that no electrode edges be patterned inside the mirror cavity and that the electrode geometry remains compatible with ion shuttling. A relay optic system has been designed to efficiently collect fluorescence over a 16 mm FOV using a multi-scale approach, enabling enhanced ion fluorescence collection over multiple mirrors distributed across a trap.

Although a significant enhancement in fluorescence collection has been demonstrated, several improvements with the current implementation may be made, including improving the profile and roughness of mirror surfaces. With improved fabrication, we believe it is feasible to produce an integrated micromirror with greater than 85% reflectivity at $\lambda = 397$ nm, which collects $\sim$ 12% of emitted photons into a cone of fluorescence. For a trap with an 85% surface reflectivity, we estimate the collection efficiency of the system when coupled to the relay optic used in the experiment (NA ≤ 0.43, FOV < 0.25 mm) to be 17% over the mirror, and 9% over a planar region ($\sim 1.8\times$ enhancement). The same analysis using the relay lens described in section 8.1.2 (NA = 0.14, FOV = 16 mm) yields estimate collection efficiencies of 12% and 0.9% for an ion above a micromirror and a planar region respectively ($\sim 13\times$ enhancement). We emphasize that a large FOV relay optic coupled to a micromirror array is expected to allow efficient, asynchronous readout over multiple ions.

We are currently considering trap designs with several integrated mirrors, and are planning experiments to demonstrate the feasibility of the multi-scale optics approach to scalable qubit detection.

References

[1] D. Boneh, R. Rivest, A. Shamir, and L. Adleman, Not. Am. Math. Soc. **46**, 203 (1999).

[2] A. Szabo and N. S. Ostlund, *Modern Quantum Chemistry: Introduction to Advanced Electronic Structure Theory* (Dover, 1989).

[3] R. P. Feynman, Int. J. Theor. Phys. **21**, 467 (1982).

[4] P. Benioff, J. Stat. Phys. **22**, 563 (1980).

[5] P. Benioff, Phys. Rev. Lett. **48**, 1581 (1982).

[6] D. Deutsch and R. Jozsa, Proc. R. Soc. London, Ser. A **439**, 553 (1992).

[7] P. W. Shor, Algorithms for quantum computation: discrete logarithms and factoring, in *Foundations of Computer Science, 1994 Proceedings., 35th Annual Symposium on*, pp. 124–134, IEEE, 1994.

[8] L. K. Grover, Phys. Rev. Lett. **79**, 325 (1997).

[9] C. H. Bennett and D. P. DiVincenzo, Nature **404**, 247 (2000).

[10] C. M. Dawson and M. A. Nielsen, Quant. Inf. Comp. **6**, 81 (2006).

[11] A. Imamoglu *et al.*, Phys. Rev. Lett. **83**, 4204 (1999).

[12] G. K. Brennen, C. M. Caves, P. S. Jessen, and I. H. Deutsch, Phys. Rev. Lett. **82**, 1060 (1999).

[13] I. Chiorescu, Y. Nakamura, C. J. P. M. Harmans, and J. E. Mooij, Science **299**, 1869 (2003).

[14] J. Clarke and F. K. Wilhelm, Nature **453**, 1031 (2008).

[15] J. J. L. Morton *et al.*, Nature **455**, 1085 (2008).

[16] P. Neumann *et al.*, Science **320**, 1326 (2008).

[17] W. Paul and H. Steinwedel, Z. Naturforsch., A **8**, 448 (1953).

[18] W. Paul, Rev. Mod. Phys. **62**, 531 (1990).

[19] W. Neuhauser, M. Hohenstatt, P. E. Toschek, and H. Dehmelt, Phys. Rev. A **22**, 1137 (1980).

[20] J. I. Cirac and P. Zoller, Phys. Rev. Lett. **74**, 4091 (1995).

[21] D. Kielpinski, C. Monroe, and D. J. Wineland, Nature **417**, 709 (2002).

[22] J. Kim *et al.*, Quantum Inf. Comput. **5**, 515 (2005).

[23] F. Diedrich, J. C. Bergquist, W. M. Itano, and D. J. Wineland, Phys. Rev. Lett. **62**, 403 (1989).

[24] C. Monroe, D. Meekhof, B. King, W. Itano, and D. Wineland, Phys. Rev. Lett. **75**, 4714 (1995).

[25] Q. Turchette *et al.*, Phys. Rev. Lett. **81**, 3631 (1998).

[26] M. Barrett *et al.*, Nature **429**, 737 (2004).

[27] J. Chiaverini *et al.*, Nature **432**, 602 (2004).

[28] S. Seidelin *et al.*, Phys. Rev. Lett. **96**, 253003 (2006).

[29] T. Monz *et al.*, Phys. Rev. Lett. **106**, 130506 (2011).

[30] J. Chiaverini *et al.*, Quantum Inf. Comput. **5**, 419 (2005).

[31] R. Blakestad *et al.*, Phys. Rev. Lett. **102**, 153002 (2009).

[32] S. C. Doret *et al.*, New J. Phys. **14**, 073012 (2012).

[33] W. Hensinger *et al.*, Appl. Phys. Lett. **88**, 034101 (2006).

[34] K. Wright *et al.*, New J. Phys. **15**, 033004 (2013).

[35] M. A. Nielsen and I. L. Chuang, *Quantum Computation and Quantum Information* (Cambridge University Press, 2000).

[36] S. Lloyd, Phys. Rev. A **62**, 022108 (2000).

[37] C. Sayrin *et al.*, Nature **477**, 73 (2011).

[38] P. W. Shor, Phys. Rev. A **52**, R2493 (1995).

[39] D. Gottesman, An introduction to quantum error correction and fault-tolerant quantum computation, in *Quantum Information Science and its Contributions to Mathematics*, pp. 15–58, American Mathematical Society, 2010.

[40] J. Preskill, Proc. R. Soc. London, Ser. A **454**, 385 (1998).

[41] M. H. Levitt and R. Freeman, J. Magn. Reson. **33**, 473 (1979).

[42] M. H. Levitt and R. Freeman, J. Magn. Reson. **43**, 65 (1981).

[43] R. Freeman, *Spin Choreography: Basic Steps in High Resolution NMR* (Oxford University Press, USA, 1998).

[44] R. Tycko, Phys. Rev. Lett. **51**, 775 (1983).

[45] R. Tycko, H. M. Cho, E. Schneider, and A. Pines, J. Magn. Reson. **61**, 90 (1985).

[46] J. A. Jones, Prog. Nucl. Mag. Reson. Spec. **59**, 91 (2011).

[47] J. J. Sakurai, *Modern Quantum Mechanics (Revised Edition)* (Addison Wesley, 1993).

[48] H. P. Breuer and F. Petruccione, *The Theory of Open Quantum Systems* (Oxford University Press, 2002).

[49] C. Gardiner and P. Zoller, *Quantum noise: a handbook of Markovian and non-Markovian quantum stochastic methods with applications to quantum optics* (Springer, 2004).

[50] A. Y. Kitaev, A. H. Shen, and M. N. Vyalyi, *Classical and Quantum Computation* (American Mathematical Society, 2002).

[51] F. Bloch, Phys. Rev. **70**, 460 (1946).

[52] D. P. DiVincenzo, Science **270**, 255 (1995).

[53] D. P. DiVincenzo, quant-ph/0002077 (2000).

[54] D. J. Wineland *et al.*, J. Res. Natl. Inst Stand. Technol. **103**, 259 (1998).

[55] H. Häffner, C. Roos, and R. Blatt, Phys. Rep. **469**, 155 (2008).

[56] D. D'Alessandro, *Introduction to Quantum Control and Dynamics* (Chapman & Hall/CRC, Boca Raton, 2008).

[57] D. E. Kirk, *Optimal Control Theory* (Dover, 1970).

[58] G. M. Huang, T. Tarn, and J. W. Clark, J. Math. Phys. **24**, 2608 (1983).

[59] G. Turinici and H. Rabitz, J. Phys. A **36**, 2565 (2003).

[60] F. Albertini and D. D'Alessandro, IEEE T. Automat. Contr. **48**, 1399 (2003).

[61] V. Ramakrishna and H. Rabitz, Phys. Rev. A **54**, 1715 (1996).

[62] D. Deutsch, Proc. R. Soc. London, Ser. A **400**, 97 (1985).

[63] R. Gilmore, *Lie Groups, Lie Algebras, and Some of Their Applications* (Krieger Publishing Company, 1994).

[64] J. Stillwell, *Naive Lie theory* (Springer Verlag, 2008).

[65] F. Albertini and D. D'Alessandro, Linear Algebra Appl. **347**, 213 (2002).

[66] D. Grensing and G. Grensing, Z. Phys. C **33**, 307 (1986).

[67] S. Blanes, F. Casas, J. A. Oteo, and J. Ros, Phys. Rep. **470**, 151 (2009).

[68] E. B. Dykin, Dokl. Akad. Nauk SSSR **57**, 323 (1947).

[69] W. Magnus, Commun. Pure Appl. Math. **7**, 649 (1954).

[70] D. P. Burum, Phys. Rev. B **24**, 3684 (1981).

[71] U. Haeberlen and J. S. Waugh, Phys. Rev. **175**, 453 (1968).

[72] J. S. Waugh, Average Hamiltonian Theory, in *Encyclopedia of Magnetic Resonance*, John Wiley & Sons, 2007.

[73] H. F. Trotter, P. Am. Math. Soc. **10**, 545 (1959).

[74] M. Suzuki, Phys. Lett. A **165**, 387 (1992).

[75] C. M. Dawson and M. A. Nielsen, Quantum Inf. Comput. **6**, 81 (2006).

[76] N. Khaneja and S. J. Glaser, Chem. Phys. **267**, 11 (2001).

[77] G. P., *Ion Traps* (Oxford University Press, Oxford, 1995).

[78] F. F. G. Major, V. N. Gheorghe, and G. Werth, *Charged Particle Traps: Physics and Techniques of Charged Particle Field Confinement* (Springer, 2005).

[79] G. Werth, V. N. Gheorghe, and F. G. Major, *Charged Particle Traps II: Applications* (Springer, 2009).

[80] D. Leibfried, R. Blatt, C. Monroe, and D. Wineland, Rev. Mod. Phys. **75**, 281 (2003).

[81] M. Abramowitz and I. A. Stegun, *Handbook of Mathematical Functions: with Formulas, Graphs, and Mathematical Tables* (Dover, 1964).

[82] L. S. Brown, Phys. Rev. Lett. **66**, 527 (1991).

[83] R. J. Glauber, *Quantum theory of optical coherence* (Wiley-VCH, 2007).

[84] F. Splatt *et al.*, New J. Phys. **11**, 103008 (2009).

[85] J. M. Amini *et al.*, New J. of Phys. **12**, 033031 (2010).

[86] J. H. Wesenberg, Phys. Rev. A **78**, 063410 (2008).

[87] D. R. Leibrandt *et al.*, Quantum Inf. Comput. **9**, 910 (2009).

[88] R. Ozeri, Contemp. Phys. **52**, 531 (2011).

[89] P. A. Barton *et al.*, Phys. Rev. A **62**, 032503 (2000).

[90] H. J. Metcalf and P. Van der Straten, *Laser Cooling and Trapping* (Springer Verlag, 1999).

[91] A. H. Burrell, D. J. Szwer, S. C. Webster, and D. M. Lucas, Phys. Rev. A **81**, 040302 (2010).

[92] H. C. Nägerl *et al.*, Phys. Rev. A **61**, 023405 (2000).

[93] F. Schmidt-Kaler *et al.*, J. Mod. Opt. **47**, 2573 (2000).

[94] T. Monz, *Quantum Information Processing Beyond Ten Ion-Qubits*, PhD thesis, University of Innsbruck, 2011.

[95] S. Olmschenk *et al.*, Phys. Rev. A **76**, 052314 (2007).

[96] S. Ejtemaee, R. Thomas, and P. C. Haljan, Phys. Rev. A **82**, 063419 (2010).

[97] B. Lindsay, K. Smith, and F. Dunning, Rev. Sci. Inst. **62**, 1656 (1991).

[98] W. Z. Zhao, J. E. Simsarian, L. A. Orozco, and G. D. Sprouse, Rev. Sci. Inst. **69**, 3737 (1998).

[99] E. D. Black, Am. J. Phys. **69**, 79 (2001).

[100] D. J. Wineland *et al.*, Proc. R. Soc. London, Ser. A **361**, 1349 (2003).

[101] B. W. Shore and P. L. Knight, J. Mod. Opt. **40**, 1195 (1993).

[102] M. O. Scully and M. S. Zubairy, *Quantum Optics* (Cambridge University Press, 1997).

[103] A. Sørensen and K. Mølmer, Phys. Rev. Lett. **82**, 1971 (1999).

[104] K. Mølmer and A. Sørensen, Phys. Rev. Lett. **82**, 1835 (1999).

[105] C. F. Roos, New J. Phys. **10**, 013002 (2008).

[106] T. Ichikawa, M. Bando, Y. Kondo, and M. Nakahara, Phys. Rev. A **84**, 062311 (2011).

[107] J. T. Merrill and K. R. Brown, quant-ph/1203.6392 (2012).

[108] A. Gilchrist, N. K. Langford, and M. A. Nielsen, Phys. Rev. A **71**, 062310 (2005).

[109] M. H. Levitt, Prog. Nucl. Mag. Res. Spec. **18**, 61 (1986).

[110] H. K. Cummins and J. A. Jones, J. Magn. Reson. **148**, 338 (2001).

[111] T. E. Skinner, J. Magn. Reson. **163**, 8 (2003).

[112] M. H. Levitt, J. Chem. Phys. **128**, 052205 (2008).

[113] B. Luy, K. Kobzar, T. E. Skinner, N. Khaneja, and S. J. Glaser, J. Magn. Reson. **176**, 179 (2005).

[114] K. R. Brown, A. W. Harrow, and I. L. Chuang, Phys. Rev. A **70**, 052318 (2004).

[115] T. Ichikawa, M. Bando, Y. Kondo, and M. Nakahara, Proc. R. Soc. London, Ser. A **370**, 4671 (2012).

[116] S. S. Ivanov and N. V. Vitanov, Opt. Lett. **36**, 1275 (2011).

[117] S. Wimperis, J. Magn. Reson. **109**, 221 (1994).

[118] N. V. Vitanov, Phys. Rev. A **84**, 065404 (2011).

[119] T. E. Skinner *et al.*, J. Magn. Reson. **179**, 241 (2006).

[120] H. K. Cummins, G. Llewellyn, and J. A. Jones, Phys. Rev. A **67**, 042308 (2003).

[121] L. Pryadko and P. Sengupta, Phys. Rev. A **78**, 032336 (2008).

[122] C. Knoernschild *et al.*, Appl. Phys. Lett. **97**, 134101 (2010).

[123] K. R. Brown, A. W. Harrow, and I. L. Chuang, Phys. Rev. A **72**, 039905 (2005).

[124] J. A. Jones, quant-ph/1303.1745 (2013).

[125] G. Vittorini, K. Wright, K. R. Brown, A. W. Harter, and S. C. Doret, atom-ph/1302.4822 (2013).

[126] C. Monroe *et al.*, quant-ph/1208.0391 (2012).

[127] C. M. Shappert *et al.*, quant-ph/1304.6636 (2013).

[128] J. Chiaverini and W. E. Lybarger, Phys. Rev. A **77**, 022324 (2008).

[129] C. Ospelkaus *et al.*, Phys. Rev. Lett. **101**, 090502 (2008).

[130] C. Ospelkaus *et al.*, Nature **476**, 181 (2011).

[131] K. R. Brown *et al.*, Phys. Rev. A **84**, 030303 (2011).

[132] D. Allcock *et al.*, Appl. Phys. Lett. **102**, 044103 (2013).

[133] J. T. Merrill *et al.*, New J. Phys. **13**, 103005 (2011).

[134] C. Langer *et al.*, Phys. Rev. Lett. **95**, 060502 (2005).

[135] N. F. Ramsey, Phys. Rev. **78**, 695 (1950).

[136] J. S. Li and N. Khaneja, Phys. Rev. A **73**, 030302 (2006).

[137] O. W. Sørensen, G. W. Eich, and M. H. Levitt, Prog. Nucl. Mag. Res. Spec. **16**, 163 (1983).

[138] J. Zhang, J. Vala, S. Sastry, and K. B. Whaley, Phys. Rev. A **67**, 042313 (2003).

[139] N. Khaneja and S. J. Glaser, Chem. Phys. **267**, 11 (2001).

[140] D. Leibfried *et al.*, Nature **422**, 412 (2003).

[141] J. A. Jones, Phys. Rev. A **67**, 012317 (2003).

[142] Y. Tomita, J. T. Merrill, and K. R. Brown, New J. Phys. **12**, 015002 (2010).

[143] J. A. Xiao, L.and Jones, Phys. Rev. A **73**, 032334 (2006).

[144] N. Khaneja, T. Reiss, C. Kehlet, T. Schulte-Herbruggen, and S. J. Glaser, J. Magn. Reson. **172**, 296 (2005).

[145] A. H. Myerson *et al.*, Phys. Rev. Lett. **100**, 200502 (2008).

[146] G. Shu, N. Kurz, M. R. Dietrich, and B. B. Blinov, Phys. Rev. A **81**, 042321 (2010).

[147] E. W. Streed, B. G. Norton, A. Jechow, T. J. Weinhold, and D. Kielpinski, Phys. Rev. Lett. **106**, 010502 (2011).

[148] M. Trupke *et al.*, Appl. Phys. Lett. **87**, 211106 (2005).

[149] J. Albero *et al.*, Opt. Express **17**, 6283 (2009).

[150] R. Noek *et al.*, Opt. Lett. **35**, 2460 (2010).

[151] B. A. Irving, H. Robbins, and B. Schwartz, J. Electrochem. Soc. **107**, 1020 (1960).

[152] V. B. Svetovoy, J. W. Berenschot, and M. C. Elwenspoek, J. Micromech. Microeng. **17**, 2344 (2007).

[153] S. X. Wang *et al.*, J. Appl. Phys. **110**, 104901 (2011).

[154] M. Harlander, M. Brownnutt, W. Hansel, and R. Blatt, New J. Phys. **12**, 093035 (2010).

[155] R. C. Jaeger, *Introduction to Microelectronic Fabrication* (Prentice Hall, Upper Saddle River, New Jersey, 2002).

[156] S. Urabe, H. Imajo, K. Hayasaka, and M. Watanabe, Jpn. J. Appl. Phys. **30**, 1532 (1991).

[157] D. J. Berkeland, J. D. Miller, J. C. Bergquist, W. M. Itano, and D. J. Wineland, J. Appl. Phys. **83**, 5025 (1998).